POLITECNICO
MILANO 1863

Luca Sartori

SYSTEM DESIGN OF LIGHTWEIGHT WIND TURBINE ROTORS

Doctoral Programme in Aerospace Engineering

January 2019

Politecnico di Milano
School of Industrial and Information Engineering
Department of Aerospace Science and Technology

Thesis for the Doctoral Programme in Aerospace Engineering
Doctoral Cycle XXX

January 2019

Author: Luca Sartori

Supervisor: Prof. Alessandro Croce
Academic Tutor: Prof. Sergio Ricci
The Chair of the Doctoral Program: Prof. Pierangelo Masarati

Printed by Tipografia Terreni s.n.c., via P. Paoli 3, 22100 Como

Of neither Sea, nor Shore, nor Air, nor Fire
But all these in their pregnant causes mixed
Confusedly, and which thus must ever fight
Unless the Almighty Maker them ordain
His dark materials to create new Worlds

JOHN MILTON, Paradise Lost

They fail, fail and try again
Fall off a cliff, succeed, and fall, fall again
They have proven quite effectively
That bumblebees indeed can fly
Against the field's authority

EINSTÜRZENDE NEUBAUTEN,
Youme & Meyou

Acknowledgements

As soon as I set foot in the academia, as a freshly-graduated rookie, I decided I would never pursue a PhD. It is quite ironic, then, that four years on I am about to conclude my doctoral studies in wind energy. Either I dramatically lost control of the events, or I wasn't so resolute in my decisions, after all.

The contents of this work are the result of a long research activity, and I am profoundly thankful to many people who have, directly or indirectly, influenced its outcomes. First, I want to thank my supervisor **Alessandro Croce**: we have worked together in many activities along these years, from research to teaching, and the sky was not always the clearest as we sat sail. I like to think that regardless of the conditions we have always tried to put quality in our work and, quite often, we succeeded.

I would like to dedicate a special acknowledgement to our colleagues from the Chair of Wind Energy at TUM, in particular to **Carlo Bottasso** and **Pietro Bortolotti**: the contents of this work have been substantially shaped by long and fruitful discussions between us, and I wish you all the best for your next research undertakings. Thank you also for your kind hospitality in Munich.

To my companions **Carlo**, **Stefano**, **Rick**, **Fede**, **Pier** and **Marco Stefano**: thank you for sharing countless fragments of everyday madness, and for the patience you put in explaining me concepts that were, most of times, beyond my understanding.

In these years I have been part of the AVATAR project, where I met brilliant, kind and enthusiastic people. I want to thank **Gerard Schepers**, **Helge Madsen**, **Spyros Voutsinas** and **Martin Stettner** for the competence and unconditional passion they showed in leading this project. And also for the understanding they showed each time I tried hard to mess up everything.

A big thank to **Francesco Grasso**, for being a constant source of inspiration and a mentor to me. Although, when it comes to football, we speak different languages.

Some time ago, at an otherwise uneventful wind fair, I met **Angelo D'Ettore** and **Michele Damiano**. I am so glad that, years later, a coincidental encounter has evolved into a beautiful partnership and friendship. Thank you for demonstrating every day that with dedication and passion it is possible to turn ambitions into reality.

Finally, I want to acknowledge all the students whose efforts have contributed to the results presented in this work: to all of you I wish a bright future and a brilliant, satisfying career.

Abstract

The growing importance of wind power in the global energy market requires a new attitude towards plant design and optimization, which must be broadly based on a system-engineering vision. As their nominal power and size increase continuously, the physical behaviour of wind turbines becomes more complex, in particular because the higher flexibility of structural components ignites a fully aero-elastic response of the system. As a consequence, it is no longer possible to subdivide specific aspects of the design into different scopes, as this would lead to an under-representation of the physics and possible shortcomings in the final product. The design of a modern wind turbine, on the contrary, should be conducted through *ad hoc* multi-disciplinary algorithms, which must support a full description of the various sub-systems and a correct resolution of the cross-effects occurring between them. Furthermore, such an approach requires the impact of certain design choices on the cost of energy to be evaluated, as cost is the primal design driver for modern wind systems. In conclusion, system design optimization (SDO) frameworks must combine high-fidelity models of the wind plant to certain optimization techniques in order to minimize the cost of energy. Although several algorithms of this kind have been recently developed, they differ significantly in their modelling, architecture and optimization settings, and a reliable common practice has not been identified so far.

In this work, we explore the concept of the system design of large wind turbines through the development of two independent SDO algorithms, which manage the design following completely different strategies. In this way, we should be able to compare the two methods and to identify the corresponding advantages and drawbacks. The first method allows the simultaneous optimization of the rotor and a set of airfoils along the blade: this feature is novel in wind turbine design, as most existing algorithms require the shapes of the airfoils to be known in advance. In our *free-form* construction, on the contrary, the whole 3D surface of the blade can be designed according to the specific and global needs of the optimization procedure. Although the level of modelling in this approach is quite basic, we eventually show how the possibility to unfreeze the airfoils is powerful when applied to modern wind turbine design, especially because the shapes of the airfoils play an important role on both the aerodynamic and the structural performance of the rotor. We show, then, how the optimizer can leverage on the airfoil shapes to favour one or more aspects of the

design, depending on the relative costs of the rotor components.

A second approach is based on the combination of high-fidelity physical models of the entire wind turbine and a multi-level design architecture. The latter features two nested layers: the outer one manages the optimization of the general features of the turbine in order to minimize the cost of energy, and is therefore ideal to conduct preliminary design studies. A series of sub-modules, then, performs the specific optimization of different components of the turbine, like the blades and the tower, according to a local merit function. We show how this second approach is particularly suited to manage detailed design applications, in which it is important that the optimal solution complies with international standards. To prove these capabilities, we show several applications: a first study aims at the integration of different passive load-alleviating techniques on a 10 MW wind turbine, in order to achieve an optimized lightweight version of the rotor. We show how significant reduction of the key loads can be obtained through different types of structural tailoring and how these advantages can be traded in favour of a reduction of the cost of energy. Subsequently, we show a second application in which different layers of design are used in combination to conduct a full development of a reference 20 MW rotor.

keywords: wind turbines, system-design, optimization, load mitigation, lightweight rotors

Contents

List of Figures

List of Tables

Nomenclature

COE	Cost of Energy
MDO	Multi-disciplinary Design Optimization
SDO	System Design Optimization
DLC	Design Load Case
BEM	Blade Element Momentum
FEM	Finite Elements Method
$\boldsymbol{p}$	Array of the design variables
$\boldsymbol{p}_{min}$, $\boldsymbol{p}_{max}$	Lower and upper boundaries of the design variables
$J(\boldsymbol{p})$	Objective function
$\boldsymbol{g}(\boldsymbol{p})$	Set of inequality constraints
$\boldsymbol{h}(\boldsymbol{p})$	Set of equality constraints
SQP	Sequential Quadratic Programming
$\boldsymbol{B}(t)$	Non-dimensional Bézier curve
$\boldsymbol{P}_i$	Bézier control points
AEP	Annual Energy Production
FCR	Fixed Charge Rate
ICC	Initial Capital Cost
AOE	Annual Operating Expenses
MDL	Macro Design Loop
ADS	Aerodynamic Design Submodule

PDS	Prebend Design Submodule
CST	Control Synthesis Tool
SDS	Structural Design Submodule
R	Rotor radius
h_{Hub}	Hub height
θ_π	Rotor tilt angle
γ_b	Blade coning angle
σ_c^g, τ_c^g	Rotor solidity, rotor tapering
σ_t^g, τ_t^g	Thickness solid area, thickness weighted area
$\boldsymbol{r}_\epsilon$	Wind turbine regulation trajectory
$\boldsymbol{p}_g$	Array of the macro design variables
$\boldsymbol{p}_a,\ \boldsymbol{p}_b,\ \boldsymbol{p}_s$	Arrays of the aerodynamic, prebend and strutural design variables
$\boldsymbol{D}$	Fixed parameters of the optimization problem
KPI	Key Performance Indicator
η	Non-dimensional spanwise coordinate
$c(\eta),\ \theta(\eta)$	Blade chord, blade twist
CHS	Cubic Hermite Spline
λ	Tip speed ratio
β	Blade collective pitch angle
v	Wind speed
Ω	Rotor speed
PID	Proportional-integral-derivative
LUT	Look-up table
LQR	Linear Quadratic Regulator
δ_y	Out-of-plane blade deflections
A_{δ_y}	Deformed rotor area
$\zeta(\eta)$	Blade prebend
$\boldsymbol{t}_b^{Fabrics}\ \boldsymbol{t}_b^{Core}$	Thicnkess of blade fabrics, thickness of blade core
$\boldsymbol{t}_t,\ \boldsymbol{\rho}_t$	Thickness of tower walls, diameter of tower segments
$\boldsymbol{F}_U, \boldsymbol{F}_{DEL}$	Ultimate loads, fatigue loads
$\boldsymbol{\delta}_U$	Ultimate displacements

$\boldsymbol{\omega_b}, \boldsymbol{\omega_t}$	Blade natural frequencies, tower natural frequencies
$\boldsymbol{\sigma_{bt}}$	Ultimate stress in blade and tower
$\boldsymbol{\epsilon_{bt}}$	Ultimate strain in blade and tower
$\boldsymbol{d}_b$	Multi-axial blade damage index
$\boldsymbol{d}_t$	Tower damage index
δ_{Hub}	Rotor overhang
NTM	Normal Turbulence Model
ETM	Extreme Turbulence Model
EOG	Extreme Operating Gust
EWM	Extreme Wind Model
BTC	Bend-Twist Coupling
ETC	Edge-Twist Coupling
RWT	Reference Wind Turbine
DEL	Damage Equivalent Loads

CHAPTER 1

The role of system engineering in wind turbine design

1.1 Design challenges and scenarios for large rotors

Wind energy has known a rapid transformation in recent years, evolving from a niche market into a widespread source of energy and a potential strategic asset for future decades. The increasing exploitation of wind and its growing penetration in the energy mix of countries has required a continuous growth in the size of wind turbines, and converters with nominal power of 8 ~10 MW are presently being commissioned. The up-scaling trend has proven to be economically viable, since larger machines support a higher energy production and a faster recover of the investment [1]. However, such growing trend also requires technological developments in order to successfully conduct the analysis and design of very large rotating systems. While, typically, the development of a certain wind plant is subdivided into several contractors with different fields of expertise, modern wind turbines exhibit an intrinsic multi-disciplinary behaviour which makes it difficult to disentangle the effects of different phenomena and to treat them separately at design level. While the aerodynamic and structural design have been usually conducted in parallel, for example, an increasing length of the beam-like elements implies a high flexibility of the rotor blades and the tower, which originates high displacements and deformations when the turbine is loaded. As a consequence, a certain reduction of the energy production should be expected, mainly because the large deformations of the blade reduce the useful area of the rotor disk. It is evident, then, that if the aerodynamic performance of the wind turbine are computed under the assumption that the rotor is rigid, the expected production of the turbine would be highly over-estimated. Additionally, since most control strategies are tuned starting from simplified simulations like the Cp-TSR curves, a misrepresentation of the rotor flexibility

would also lead to an incorrect computation of the regulation trajectory of the turbine in different operating ranges. In this scenario, then, the coupled aeroelastic response of the turbine becomes determinant, especially because the flexibility of the components means that the eigen-frequencies of the turbine are low, which increases the risk of dangerous superposition among different turbine modes or between the natural frequencies of the turbine and the *per-revolution* ones introduced by the rotating motion. The consequences of un-resolved resonances can be perceived through the dynamic response of the system, which could cause a sharp increase of the fatigue damage along the turbine, but also increased vibrational problems and instabilities. Unstable behaviours can be also triggered by purely aero-elastic effects, like flutter or stall-induced vibrations [2, 3].

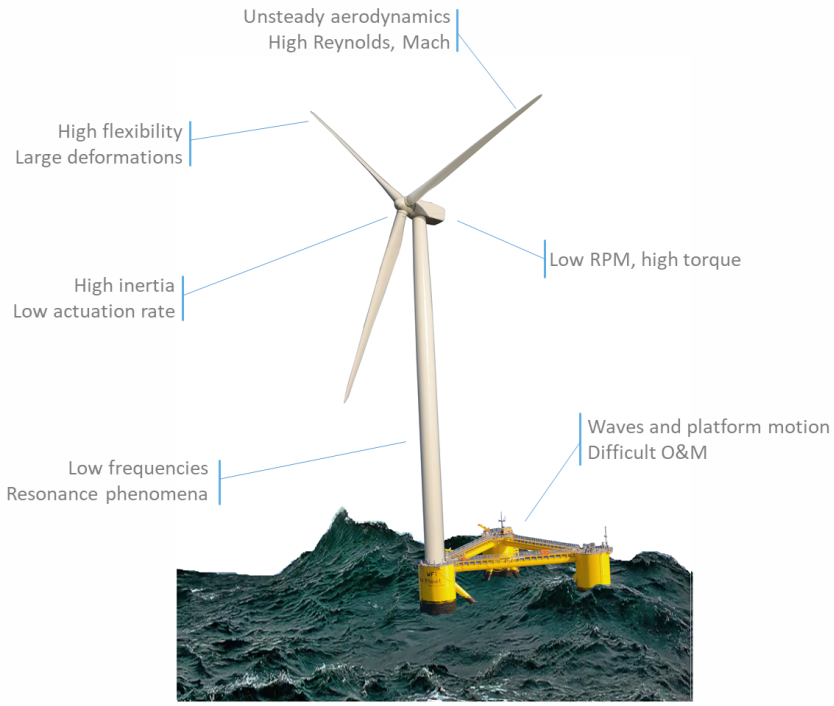

Figure 1.1: *Design challenges of modern wind turbines.*

Additional complexities which influence the design arise from the unsteady and non-uniform wind field impinging on the turbine, which in turn causes highly-variable loads on the turbine [4]. At sectional level, high Reynolds and Mach numbers along the blade make difficult to characterize the airfoil performance through wind tunnel experiments and it is usually necessary to recur to CFD calculations. Additionally, since the rotor speed is lower for larger rotors, this implies that the blades must produce higher torque to achieve a certain power, with consequences on the design of drive-train and generator [5] and with increasing loads transmitted to the system infrastructure. The recent interest concerning offshore wind energy introduces more complexities, as the wave motion causes additional loading on the system. In the same context, the design of the support structure is also fundamental since it affects the overall balance of the turbine, its resulting motion and the relative aerodynamic inflow, but also the stability of the system. Figure 1.1 gives a qualitative representation of a modern wind turbine and some of the main design challenges.

To address these peculiarities, it is necessary to develop novel approaches to the design of next-generation wind turbines, which must forcibly be based on the integration of different discipline-specific contents into a unified perspective at system level. Since the evolution of a certain turbine component during the design can significantly influence other aspects, the ability to correctly capture, describe and resolve mutual influences between different parts of the design is a fundamental achievement of a modern approach to wind turbine design. In recent years, there's been an effort from the wind energy community to develop such a multi-disciplinary vision, and this required to re-negotiate the assumptions of most design applications and, in particular, a redefinition of what are the fundamental design drivers. While classic approaches usually optimized the turbine to produce the maximum energy production, it is now widely accepted that modern turbine design should aim at the minimization of the Cost of Energy (COE) [6, 7, 8, 9]. This is usually achieved by defining the COE as the merit function of a dedicated Multi-disciplinary Design Optimization (MDO) algorithm. In fact, the computation of the cost of energy is directly affected by technical, managerial and economical characteristics of the project and this makes possible to account for several requirements, usually coming from different aspects of the design, and to condense all these information into a unified parameter, so that it is much easier to properly evaluate the impact of certain design choices on the overall performance of the system.

The effective implementation of an MDO procedure, however, is not a trivial task since it requires to discuss a series of fundamental aspects:

- The computation of the COE. The cost of energy is the ideal merit function for an MDO, since it summarizes the description of a whole system into a number. However, the way it is calculated can dramatically influence the optimization, and potentially drive the optimization in completely different directions.

- Capturing the physics of the turbine. The numerical modelling of wind turbines has improved significantly in recent years and different models of increasing complexity are available for the description of the aerodynamics and the structure. While the choice of low or high-fidelity models can have some impact, it is instead absolutely necessary that the models capture the multi-disciplinary aspects of the wind turbine behaviour. Usually, higher-fidelity models intrinsically support a better physical description, but is also possible to rely on simplified models which share information with one another.

- The domain of optimization. In addition to a certain level of modelling, it is important to define how many design variables are included into the multi-disciplinary optimization algorithm. To support a system-level design, in fact, different unknowns coming from different disciplines should be collected together. These parameters ideally account for the blade shape, the internal structure of the blade (and possibly the tower), the general features of the rotor and, potentially, of the wind farm. Usually, combining a satisfactory number of variables to a sufficient quality of the physical modelling is hard, and often compromises have to be made. The nature of such compromises and the direction they favour typically characterize the MDO.

1.2 State of the art in the integrated design of wind turbines

Numerical optimization methods have been successfully applied to specific wind turbine design tasks, in particular the shape optimization of the rotor and the structural sizing of blades and tower. Recently, several authors have proposed different approaches towards the implementation of multi-disciplinary design algorithms. These contributions have been quite heterogeneous and show wide differences in the methods, the level of modelling and the design variables. In the following, we provide a brief survey of the most prominent works in the field of MDO design of wind turbines. In an effort to give a consistent review, we introduce the informal criteria of considering as MDO only those methods that combine design variables which historically pertain to different design branches (e.g. aerodynamic and structural design). In addition, we define as System Design Optimization (SDO) those algorithms which support the design of the rotor and at least another component of the turbine. These are not, however, strict definitions. The application of system design to wind turbines is in fact quite recent and a recognized nomenclature is still missing.

1.2.1 Rotor design studies

A broad family of MDO applications has its focal point on the design of the rotor and a great deal of contributions is available in the literature. In this context, Kenway and Martins [10] were among the first to conduct a truly coupled aero-structural design in which variables related to chord, twist, airfoils and structure were optimized to minimize the COE at a certain wind site. Later, Xudong et al. [11] introduced an aero-elastic model of the wind turbine and optimized the aerodynamic shape of the rotor under limits on the axial thrust and the shaft torque. In this work, the structure was indirectly optimized through the thickness of the blade. More recently, Pourrajabian et al. [12] applied a genetic algorithm to design a small-scale wind turbine rotor. Here the design variables account for chord and twist as well as the shell thickness, while the design objectives include the starting time and the power output. Bottasso et al. [13] developed a procedure in which the chord and twist of the blade is optimized together with the thickness of all the structural components. Here, the procedure is based on a multi-stage process in which the rotor shape is firstly optimized and the resulting solution is then fed to a structural optimization problem. A peculiarity of this application is that the structural optimization is based on a broad set of fully-resolved Design Load Cases (DLC), which are continuously re-computed during the design. The problem of defining an accurate, yet computationally affordable load basis has been investigated in detail by several authors. For example Sessarego and Shen [14] proposed an optimization method based on surrogate modelling which include a very large set of load cases. In this case, the chord, twist and thickness of a 5 MW rotor are successfully optimized, together with the spar caps and the shear webs, for a set of hundreds of load cases. An alternative methodology has been proposed by Pavese et al. [15] and is based on the substitution of computationally-expensive turbulent cases with custom-made shear zones and equivalent deterministic loads. This way, the authors were able to embed the load computation directly within the workflow of the MDO algorithm and to re-optimize a 10 MW rotor with the reduced load basis. Several authors have applied genetic algorithms to the design of rotors: Zhu et al. [16], for example, combined the Blade Element Momentum (BEM) theory to a three-dimensional Finite Elements Method (FEM) to conduct the aero-structural optimization of a 1.5 MW rotor blade. Aerodynamic design variables in this work include the rotor speed and the chord distribution, while structural ones account for the thickness and the width of the spar caps and the positioning

of the shear webs. The optimization is then managed by a non-dominated sorting genetic algorithm. A similar study in which BEM and finite elements are combined has been conducted by Dal Monte et al. [17] although the focus here is on small-scale rotors. Very recently, Yang et al. [18] proposed a similar methodology to redesign a 2.1 MW rotor. A particular aspect of this work is that airfoil shapes are described by means of Taylor series and directly designed as part of the optimization problem. The possibility of designing the airfoils together with other aero-structural variables is a prominent topic and will be extensively discussed in this work. A recent application of rotor-based MDOs, concern the study of solutions for very large rotors and, possibly, load-mitigating techniques to support lightweight ones. In this light, for example, Richards et al. [19] proposed an integrated aero-elastic design of a 100 m blade. The study considers the impact of bond-line damage, a common failure mode for long blades, on the design and explores how an MDO-based design can reduce its influence on the integrity of the wind turbines. Pavese et al. [20], instead, employed an MDO approach to optimize the sweep of the blade achieving an important load alleviation on a 10 MW rotor. Similar studies, although based on different techniques are conducted later on as part of this work.

1.2.2 System design of wind turbines

More recently, several researchers applied the concept of multi-disciplinary design to the whole wind turbine, introducing the idea that accurate modelling of physics, coupled to suitable optimization schemes, could pave the way for a system-engineering approach to the design of modern wind turbines. An early realization of this SDO perspective was proposed by Fuglsang et al. [21], who first combined aeroelastic simulations to an optimization cycle based on the COE. Here, the design variables are some macro-parameters of the wind turbine like rotor shape and diameter, tower height and rotor speed, whose impact on the COE are computed through a dedicated model. Through this construction, the authors performed several site-specific redesigns of wind turbines from 600 kW to 1 MW. Later on, Maki et al. [22] discussed an SDO based on a multi-level design architecture. In this framework, an external optimization is employed to minimize the cost of energy. At this level, design variables include rated power, rotor diameter, rotor speed and other turbine parameters. This loop is interfaced with two sub-levels, which conduct discipline-based optimizations. The first allows to maximize the AEP of the rotor, while the second minimizes the loads produced by the blades. In this view the architecture is similar, although based on simplified models, to that presented in this work. Another formulation at system-level has been presented by Ashuri et al. [23, 24]. Here, a preliminary round of design can be made by optimizing blade length, tower height and the rotor speed for minimum COE. Then the optimal configuration is fed to a second optimization problem which manages aero-structural design variables from the rotor and the tower. The design unknowns, which are monolithically designed together, account for the chord, the twist, the blade structure (shell and spar caps thickness) and the tower (diameter and thickness of the top/bottom sections).The simulation environment is built around the solver FAST, which allows to take full DLC into considerations during the design. The authors validated this approach through a redesign of the NREL 5 MW reference and, later, employed it to test the validity of classic up-scaling relations in the range 5-20 MW. Significant research on SDO algorithms has been done at NREL [25], who developed an integrated tool for the analysis and design of a wind energy project from component level to the entire wind plant. The algorithm is based on the OpenMDAO [26] software which manages the optimization problems and links the different models required for the various simulations, which sup-

port increasing levels of detail depending on the needs. The engine of the algorithm is the internal cost models which recursively computes the COE by taking information from the various modules. A similar project, also based on OpenMDAO has been recently developed at DTU [27]. The structure of the information flow basically allows to conduct a full aero-structural optimization of large wind turbines and the simulation environment is widely based on internally-developed software. The tool includes some particular specialisms, like the possibility to design the airfoils during the optimization and a frequency-based fatigue model which reduces the computational time.

1.3 Scope, assumptions and methodology of this research

This work deals with the optimization of wind turbines at system level, and its possible applications to the design of next-generation lightweight rotors. To fulfil this scope, the activities developed during this research follow two main trails. A first direction is the development of SDO-dedicated algorithms: here the goal is to craft the necessary tools in order to properly tackle the challenges of modern wind turbine design, and during this work we explore two different strategies, which are eventually very different from each other in terms of design assumptions, modelling and optimization set-up. Our first approach to the SDO design is based on the concept of *free-form*, which was firstly proposed by the author as a tool to conduct the aerodynamic design of rotors (see Sartori et al. [28]). The main innovation of this approach is that the shapes of the airfoils along the blade are treated as unknowns within the optimization problem, and their shapes are optimized together with classic aero-structural variables. During this research, we developed the methodology and extended its capabilities to support a complete aero-structural design of the rotor and, subsequently, a preliminary sizing of the rotor diameter. A second methodology is developed in partnership with the Technische Universität München starting from the works of Bottasso et al. [13, 29]. The idea is to create an SDO design framework which combines high-fidelity models of the wind turbine and a series of different design modules, which are organized in separated layers. This approach is a novelty in wind energy, since previous research was based either on monolithic approaches or on multi-level design but, usually, with only low-fidelity models or a limited load spectra. One of the essential advantages of this construction is the possibility to maintain a possibly large number of DLC directly within the design, so that optimal solutions automatically comply with international certification standards.

A second direction of this research is the application of these new MDO/SDO algorithms to design lightweight rotors for modern wind turbines. With the term *lightweight*, we refer to a solution which drastically reduces the loads when compared against a certain initial configuration. The topic has been recently quite hot in wind turbine design, mainly because it is well-known that the blade mass increases as a third-power of the rotor diameter [30]. This fact implies that, unless technological breakthroughs are introduced and the blade design departs from this trend, future wind turbines will require extremely massive rotors. In this context, we want to conduct a rigorous investigation of the impact of structural tailoring on the performance of large rotors, and our new algorithms will be used to continuously re-optimize the required aspects of the rotor, so that a consistent comparison could be ideally made. One of the secondary goals of this research is to develop the first structurally-feasible configuration of a 20 MW wind turbine rotor. Ideally, this activity should demonstrate how the SDO algorithms can cope with the design and the subsequent optimization of very large rotors.

1.4 Organization of the work

This Thesis is organized as follows: Chapter 2 is dedicated to the development of the *free-form* approach. We discuss the new features of the algorithm and the main choices we made on the optimization process and, importantly, on the level of modelling. We show how the tool can manage an integrated aero-structural design of the rotor which includes the airfoil and, eventually, that it can be used as a basic SDO algorithm for the simultaneous optimization of the rotor diameter, the aerodynamic shape and its internal structure. We then conduct several applications to demonstrate the capabilities of the approach on realistic design problems. In Chapter 3 we present a completely different approach to system design, based on high-fidelity models and a multi-level architecture. The features of the code are presented, together with the specifics of the data-flow. We show how the program can be used as a fully-automated SDO or, depending on the needs, as an MDO to conduct components design or, eventually, as a tool for the mono-disciplinary design of certain parts of the turbine. Once we described the algorithm, we use it to perform a detailed structural definition of different Reference Wind Turbines (RWT), ranging from 10 to 20 MW. These models, developed and presented in Chapter 4, are conceived to serve as starting point for subsequent design applications and, potentially, as benchmark configurations for additional research activities. Chapter 5 is dedicated to the investigation of passive load alleviating techniques, based on different levels of structural tailoring. We show how the properties of the materials and the sectional topology can be leveraged to induce significant reduction in the driving loads of a large rotor. The effectiveness of such strategies is demonstrated through analysis of increasing complexity and, eventually, two 10 MW rotors are redesigned to transform the beneficial effects of the load alleviation in a reduction of the COE. Chapter 6 shows a redesign process in which our 20 MW baseline is optimized to achieve lower loads and a globally lighter rotor design. Eventually, Chapter 7 provides an overview of the achievements of this research project and a brief discussion about possible developments.

CHAPTER 2

Free-form design of rotors

In this Chapter, we introduce and describe a *free-form* methodology to manage the multi-disciplinary design of wind turbine rotors. The approach is characterized by the fact that the airfoil shapes are included in the set of the optimization variables, so that they are optimized together with typical aero-structural variables like chord, twist and the thickness of structural components. Given the high number of variables introduced by the parametrization of airfoils, we developed the *free-form* design algorithm as a monolithic gradient-based solver in which all variables are managed together through a centralized data-flow. The 2D polar data of airfoils are automatically computed and updated through XFOIL, whereas an essential BEM model provides the 3D performance of the rotor. However, a flexible blade model coupled to a detailed 2D sectional description of the structure allows a satisfactory management of the main integrity constraints. The optimization procedure is based on the minimization of the COE, so that non-trivial compromise configurations can automatically emerge as part of the optimal solution if they lead to a reduction of the total system cost. Through a summary of applications we demonstrate that, albeit its inherent simplicity, the free-form is able to manage complex design challenges and to deliver interesting solutions.

2.1 Motivations

A key feature of most blade optimization algorithms is the use of BEM or lifting-line methods for the computation of the aerodynamic performance of the rotor. These methods are much faster than vortex-based ones or CFD analysis and, although being based on simple actuator disk and moment theories, they can provide a level of accuracy which is acceptable in most practical applications [31, 32, 33]. Nevertheless, their use require that aerodynamic tables listing lift, drag and moment coefficients are provided for several Reynolds and Mach

numbers along the blade. These data are readily available for existing families of airfoils, as they typically come from high-fidelity numeric simulations or from measurement campaigns. However, when it comes to the problem of rotor optimization, such requirement implies that either the airfoils are chosen at the beginning of the design and then frozen, or that their aerodynamic data are updated whenever their shape is changed. Most design algorithms currently used by manufacturers adopt the former strategy and the airfoils are selected from existing families although, according to the needs of the project, it might happen that new airfoils are designed on purpose. However, the principal implication of a frozen strategy is that a certain blade is optimized for a specific set of airfoils. From a designer's viewpoint, it is difficult to overlook the limitations of such an approach. As discussed, modern wind turbine rotors exhibit important aero-elastic effects in their behaviour, and those effects are triggered by the aerodynamic characteristic of a rotor as well as by its structural response. A partial, albeit important conclusion is that the design of modern wind turbine rotors should be carried out with a genuine multi-disciplinary vision in mind. In this context, the choice of the airfoils is central, since their geometries have a strong influence on both the aerodynamic performance and the structural integrity of the rotor. When, as designers, we target the power production of a rotor we intuitively prefer thinner airfoils, as they show a better aerodynamic efficiency. When it comes to the structural design, on the contrary, thicker shapes guarantee higher sectional inertia and a better redistribution of the internal stress. However, when the target of the design is no longer genuinely aerodynamic or structural but shifts to the minimization of the COE, it becomes much more difficult to identify ideal characteristics for a certain airfoil: since the merit function is computed at a global performance level, it is not straightforward to translate a global optimality criteria into local requirements at sectional level. This consideration justifies the fact that, often, the optimization of individual airfoils for wind turbines is a diffcult task itself. Unsurprisingly, there are many works in the literature aiming at the design of airfoils for wind turbines [34, 35, 36, 37]. Typically, conflicting requirements are managed by setting up a multi-objective optimization process or by defining a suitable linear combination of parameters such as lift, thickness, sectional inertia and surface transition points. Although these choices can be effective, the problem of how to translate global optima into sectional requirements persists, in particular because it remains unclear how to tune the relative importance of each merit figure against the others at certain parts of the blade. In the *free-form* approach on the contrary, the overall optimization of the COE provides the necessary directions for the design of the airfoils, and specific requirements at different parts of the blade are automatically managed. Additionally, the importance of the intial choice of airfoils is significantly reduced, and finally altogether eliminated. In the following we show how the proposed free-form approach encourages the natural emergence of certain configurations, for example flatback airfoils, if such shapes represent optimal choices in certain circumstances. Airfoils at different span locations are free to adapt to different local conditions, which depend on the relative importance of the aerodynamic and structural requirements at that location. We also show how the relative thickness of airfoils, and thus their efficiency, can be automatically sacrificed in favour of better structural performance when the optimization requires this choice, for example when the blade is laminated with a very expensive material. We first proposed this idea, limited to the sole aerodynamic design in [28] and we later expanded it to support a complete aero-structural design with free airfoils [38, 39]. The same approach has been furtherly explored in the literature by Zhu et al. [40] and recently by Ning and Barrett [41].

2.2 Design philosophy

The idea of simultaneously designing the blade and the airfoils involves certain difficulties. The first is related to the modelling of the wind turbine: in fact, the design algorithm must be able to perform and manage a variety of simulations which must provide the 2D data of airfoils as well as the 3D performance of the rotor. Additionally, some structural verifications must be included in order to ensure the feasibility of the optimal solution. A second thought concerns the number of design variables: in a typical design scheme, the shape of the blade and the structure can be easily parametrized so that the number of associated design variables is reasonably low. On the contrary, the description of the airfoil shapes typically requires a large number of degrees of freedom, so that each airfoil which is left free to optimization adds more and more design variables. Third, the array of the design variables is quite heterogeneous, since it includes variables related to the chord, the twist, the structure and the airfoils. Then, a major point is to decide which is the most suitable algorithm in order to have an effective exploration of the design space.

With these challenges in mind, we choose to favour the simplicity of the *free-form* and its computational speed rather than the accuracy of the models. Thus, in this Chapter, the discussion on the results is more qualitative than quantitative, as we are fully aware that the solutions here illustrated are not feasible designs in a strict sense. As we discuss later on, the *free-form* algorithm is organized as a monolithic optimization problem in which all design variables are optimized by an SQP gradient method at the same level. This is not the only possible choice, since optimization algorithms can be structured as a multi-level architecture. A risk of gradient-based optimization is that the merit function can show different sensitivities for different variables: one can ease this phenomena by defining non-dimensional variables, however, this is an intrinsic issue of the method and it could not be completely eliminated. A main objective of this study, then, is to understand how effectively the *free-form* can manage the optimization of all the different variables. We decided to favour simplicity also at simulation level, so that the algorithm was conceived as a coordinated work-flow in which different analyses are carried out by different sub-modules, most of which are open-source programs already available in the community. In the following, we'll give a brief description of the features of the algorithm.

2.3 Description of the algorithm

In this study, the aero-structural design of a rotor blade is expressed as a single-objective constrained optimization problem. The merit function is based on the cost of energy, so that it is theoretically possible to capture optimal trade-offs between aerodynamic and structural requirements, while suitable constraints are used to express desired features of the solution, or to force the fulfilment of safety requirements. The optimization problem can be formulated as follows:

$$\min_{\boldsymbol{p}} J(\boldsymbol{p}), \tag{2.1a}$$

$$\text{s.t.: } \boldsymbol{p}_{\min} \leq \boldsymbol{p} \leq \boldsymbol{p}_{\max}, \tag{2.1b}$$

$$\boldsymbol{g}(\boldsymbol{p}) \leq 0, \tag{2.1c}$$

$$\boldsymbol{h}(\boldsymbol{p}) = 0, \tag{2.1d}$$

where $J(\boldsymbol{p})$ is the objective function, $\boldsymbol{p}$ the vector of the n design variables, whose lower and upper bounds are expressed by Eqs. 2.1b, while Eqs. 2.1c and (2.1d) are, respectively, the inequality and equality constraints applied to the design. The numerical solution of the problem 2.1 is here managed by a gradient-descent sequential quadratic programming (SQP) algorithm [42] in which the gradients of the merit figure and of the constraints are computed through forward finite differences. The architecture of the program is based on a main bus along which all relevant data are dispatched and transmitted. The bus is written in FORTRAN and it is interfaced with several analysis modules, all of them invoked by the algorithm as Windows executable files. A qualitative description of the data-flow of the *free-form* algorithm is given in Fig. 2.1.

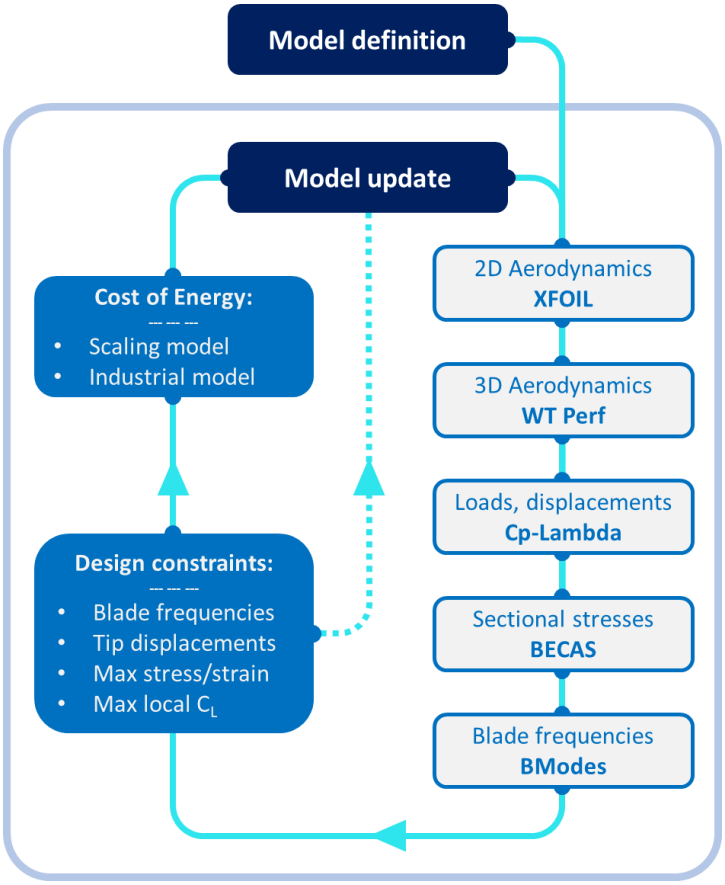

Figure 2.1: *Architecture of the free-form design algorithm.*

2.3.1 On the shape parametrization of airfoils

When the *free-form* is initialized, the model definition requires the description of the blade shape in terms of chord, twist and geometry of the airfoils. To limit the number of design variables, all these functions must be defined through a suitable parametrization. How to describe airfoils, in particular, is a non-trivial decision: an ideal parametrization should

combine a low number of parameters and a high level of flexibility in order to correctly represent existing families of airfoils. Moreover, it should not have singularities in its domain, in order to prevent the automatic optimization procedure from falling into non-existing solutions. In this view, at the beginning of the development we chose to describe airfoils through the NACA 4 digits representation, so that a single airfoil could be defined by only three parameters [28]. Intuitively, for the purpose of representing wind turbine airfoils that was an oversimplification, and in fact, modern airfoils for wind energy differ significantly from the pre-assumed shapes produced by the NACA 4 equations. However, the extremely low complexity of the formulation allowed us to run a wide campaign of tests in order to verify the functioning of the program. For the complete version of the code a more sophisticated parametrization was required. The literature provides several examples of specific parametrizations for aeronautical and wind energy use. Comprehensive reviews of the most common methods are given by Salunke et al. [43] and by Shahrokhi and Jahangirian [44]: these include more complex families of NACA (5,6 digits), the PARSEC and modified Sobieczy [45, 46] the Bernstein-CST [47, 48], B-Splines [49] and the Bézier polynomials [50]. The latter method, in particular, has been developed for the computer graphics and successfully employed in many fields of computer science [51, 52] and we eventually adopted it as the standard parametrization of airfoils within the *free-form*. In its general formulation, a Bézier curve of degree n can be determined from the position of $n+1$ control points:

$$\begin{aligned}\mathbf{B}(t) = \sum_{i=0}^{n} \binom{n}{i} (1-t)^{n-i} t^i \mathbf{P}_i = \\ (1-t)^n \mathbf{P}_0 + \binom{n}{1} (1-t)^{n-1} t \mathbf{P}_1 + ... \\ + \binom{n}{n-1} (1-t) t^{n-1} \mathbf{P}_{n-1} + t^n \mathbf{P}_n\end{aligned} \tag{2.2}$$

here, $\mathbf{B}(t)$ is the array of the points of the curve along the non-dimensional coordinate $0 \leq t \leq 1$, while $\binom{n}{i}$ are binomial coefficients and $\mathbf{P}_i$ are the control points of the curve. It's straightforward to show that Bézier curves have the following properties:

1. The first point of the curve coincides with the first control point $\mathbf{P}_0$.
2. The last point of the curve coincides with the last control point $\mathbf{P}_n$.
3. The start and the end of the curve is tangent to the first and last sections of the Bèzier polygon defined by the control points
4. A curve can be split at any point into two subcurves, or into arbitrarily many subcurves, each of which is also a Bézier curve.

The combination of these properties allows to design versatile curves which can be tailored to the problem at hand. In the *free-form*, for example, we parametrized each airfoil with four different Bézier curves of order 3. The resulting structure is shown in Fig. 2.2, where the four curves are identified by different linestyles.
This construction was first proposed by Grasso et al. [53, 37, 54] and was here modified to allow its use within the *free-form* dataflow. As shown, the control polygon is made of 13 points which, depending on their associated degrees of freedom, can be frozen (0 d.o.f), mono-directional (1 d.o.f.) or bi-directional (2 d.o.f). Usable degrees of freedom

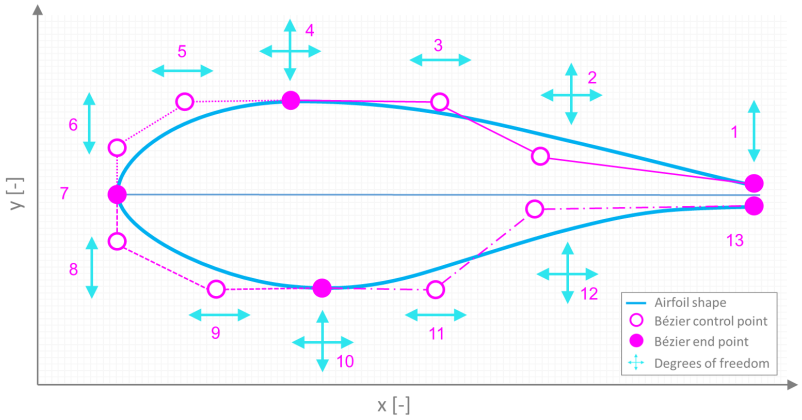

Figure 2.2: *Parametrization of an airfoil with Bézier curves.*

are represented in Fig. 2.2 by double-arrowed lines pointing in the direction of the d.o.f. The geometry of a single airfoil is then controlled by a total of 15 design variables. It is important to notice that building the Bézier polygon with four curves instead of just 1 or 2 leads to a much better control over the regularity of the shape. By exploiting the properties 1-4), for example, it is possible to ensure that the upper surface has a horizontal tangent at its summit point (see point 4). Geometrically, this implies that the segment connecting points 3, 4, 5 is horizontal, so that the three points must always have the same y coordinate: that's why point 4 has two associated degrees of freedom while points 3 and 5 have only one. Similar considerations apply for the lower surface and for the vertical tangent at the leading edge.

This construction is very intuitive when compared against other types of parametrization: by changing the position of the control points, the optimization algorithm can modify the associated curve with a good sensitivity, in particular because all the end points of the Bézier curves are defined directly on the surface of the airfoil. Additionally, with just few subtleties it is possible to ensure that degenerate configurations do not appear during the design. In particular, it is necessary that the curves are always defined on the whole range $x \in [0\ 1]$. With reference to Fig. 2.2 this requires that points 1, 6, 7, 8 and 13 do not modify their abscissa during the design. Similarly, a second geometric constraint must be enforced to guarantee that the thickness of the airfoil is always positive along the chord. In fact, most 2D aerodynamic solvers would struggle to cope with degenerate cases in which the upper and lower surfaces are reversed or twisted. This can be formalized by the requirement that:

$$max(t) = max(y^{ss}(x) - y^{ps}(x)) \geq 0, \quad x = [0\ 1] \tag{2.3}$$

where y^{ss} is the suction-side surface and y^{ps} the pressure side. Numerically, Eq. 2.3 can be evaluated at discrete points along the chord, and in particular in the vicinity of the trailing edge, where the physical thickness of the section becomes narrow. These two geometric constraints are the only ones which are strictly necessary for a good conditioning of the optimization problem. Other geometry requirements can be defined, according to the designer's own experience, in order to prevent odd configurations to appear and to increase the stability of the program. However, the discussion of such additional constraints falls beyond the scope of this work and is not detailed here.

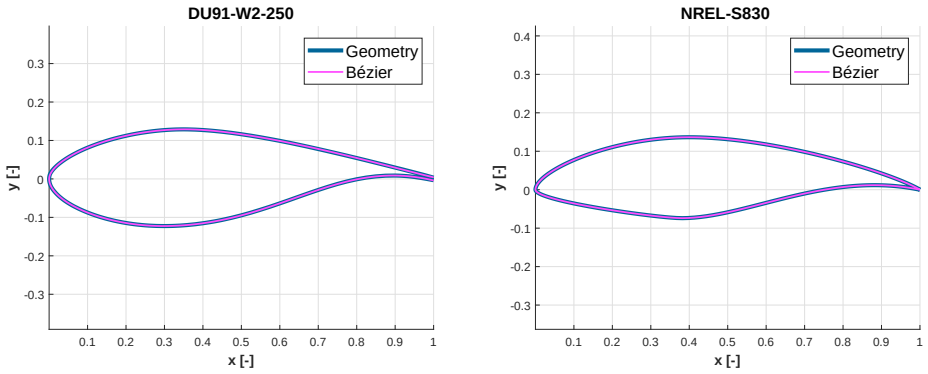

Figure 2.3: *Two examples of airfoils described with the Bézier parametrization: DU91-W2-250 (left) and NREL-S830 (right)*

Another important advantage of this formulation lies in its flexibility: the definition through Bézier curves allows the optimization process to have full authority over important features of the airfoil like camber, bluntness of the leading edge, steepness of the surface and thickness. It also supports flatback airfoils. This generality makes possible to represent most existing families of airfoils via the Bézier curves by identifying a suitable combination of control points. For example, Fig. 2.3 shows how the geometries of the DU91-W2-250 and NREL-S-830 can be successfully approximated with the Bézier curves introduced above. For each airfoil, the approximating curves were obtained as the solution of an optimization problem in which the weighted difference between the actual geometry and the one coming from the Bézier was minimized. In both cases, the optimal Bézier shape achieved a very good agreement with the original geometry of the corresponding airfoil.

The Bézier parametrization is prone to some inherent limitations. First, the mathematical construction of the Bézier curves is not specific for airfoils, as it supports curves of arbitrary length and shape. This means that strange geometries can emerge during the design, usually resulting in the missed convergence of the simulation tools. We showed that countermeasures are possible to minimize the occurrence of such degenerate shapes, however, the definition of suitable constraints requires time, experience and loads of test runs. A second point is the high number of design variables of this parametrization: since each of them requires 15 degrees of freedom, even a limited set of airfoils can drive up the number of design variables. This aspect poses a serious limit on the level of fidelity of the simulations. However, for what concerns the scope of this study, we decided that the focus is definitely on the design of airfoils, as this capability is a significant innovation in the field of wind turbine rotor design. Then, we decided to adopt the Bézier approximation in order to enjoy a high flexibility on the design of airfoils and to extend significantly the exploration of the design space. As we discuss in the next Sections, this comes at the cost of a reduced complexity of the simulation models.

2.3.2 Chord, twist and structure parametrization

In addition to the variables related to the airfoil shapes, the array of the design variables includes parameters for the shape of the chord and twist, and others related to the thick-

ness of the structural components. Chord and twist functions are also parametrized through Bézier polynomials, although the construction of the control polygon is slightly different from that of the airfoils. In particular, the shape of the chord is controlled by two curves of different degrees, which merge at the point of maximum chord. A sketch of this construction is represented in Fig. 2.4, where the two curves are identified by different line styles.

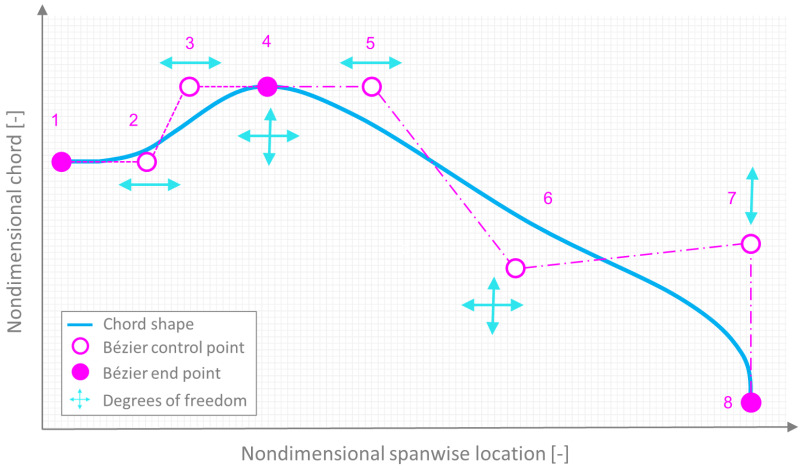

Figure 2.4: *Parametrization of blade chord with Bézier curves.*

The first curve is a 3rd-order Bézier which controls the chord design between the root of the blade and the section of maximum chord: two geometric constraints are enforced in order to ensure that the tangent is horizontal at the root (segment 1-2) as well as the maximum chord (segment 3-4). The second curve describes the chord function between the section of maximum chord and the blade tip. This curve can be of any order, according to the required complexity. In the example of Fig. 2.4, we defined a 4th-order Bézier. Again, the horizontal tangent at the maximum chord is guaranteed by the constraints that the segment connecting points 4 and 5 is always horizontal. This way, a C^1 continuity is guaranteed along the blade, promoting a better controllability and regularity of the generated shapes. It can be seen that, in the example, the total number of degrees of freedom is 8. This number can be higher, if higher-order Bézier curves are used for the second part of the blade, but it also represents the minimum number of parameters which are required for the description of the chord.

The shape of the twist does not require particular geometric constraints, so that its description through Bézier curves can be more unstructured. For this reason, the twist function is described by a single Bézier of an arbitrary degree. In a limiting case, even a 1st-degree curve defined by only two control points could suffice, although the property of a Bézier curve being tangent to its first and last segment would result in a straight distribution of twist rather than a curvilinear shape. However, additional control points ensure a better flexibility of the underlying shape as illustrated in Fig. 2.5. The example shows a 6th-degree Bézier curve and its associated 11 degrees of freedom. In general, the number of degrees of freedom related to the twist is $n_{DOF} = 2(d-1)+1$ where d is the degree of the curve. In the application of the *free-form* algorithm, a horizontal tangent is usually imposed at root, in order to better control the regularity of the shape and to favour the convergence

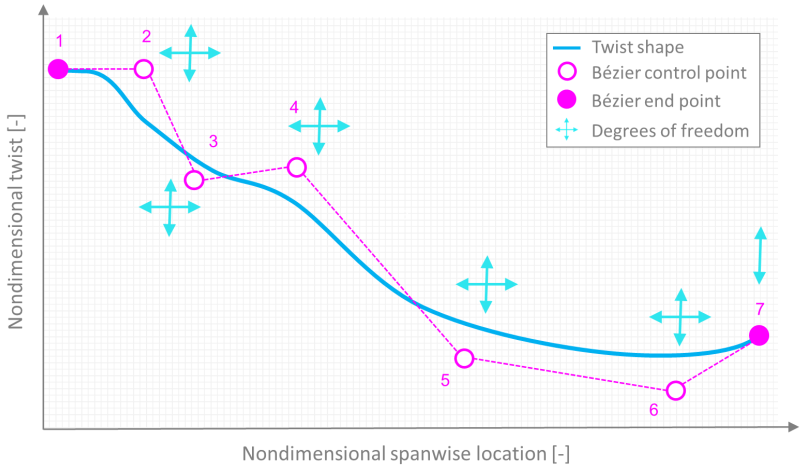

Figure 2.5: *Parametrization of blade twist with Bézier curves.*

of the solvers. However, this is not a strict requirement in real applications.

The parametrization of the structure is much simpler, in fact, the thickness of the optimized structural components are directly discretized at the required design stations. When their value is modified, a full spanwise distribution is recovered by interpolation.

2.3.3 Wind turbine modelling

Starting from a given initial guess, at each iteration the algorithm generates a new configuration, which is then evaluated following the steps highlighted in Fig. 2.1. Each step corresponds to a certain analysis, as follows.

2D aerodynamics

The 2D aerodynamics data of the generated airfoils are estimated by the panel solver XFOIL from Drela [55, 56]. This method is fast enough to be included directly in the optimization algorithm, and its viscous/inviscid formulation allows the designer to account for the boundary layer, which can be customized by tuning the embedded transitional model [57]. The default operating mode of the program performs, for each designed airfoil, two different simulations at different Reynolds numbers. This way, the 3D aerodynamic model can perform a suitable interpolation in order to use aerodynamic data which are close to the actual Reynolds at that section. It is important to notice that, in XFOIL, it is possible to fix the transition on the upper and lower surfaces: this way it is possible to simulate a certain amount of surface roughness and to account for leading edge deterioration at design level. Since the reliability of XFOIL results drops quickly after the stall, the coefficients C_L, C_D, C_M are computed in a range $\pm 20°$ and subsequently extrapolated according to the method by Viterna and Corrigan [58]. Once that airfoil tables are generated, these are interpolated on a finer mesh in order to build a span-wise distribution of the coefficients along the blade.

3D blade aerodynamics

Once the aerodynamic tables of the airfoils have been built, the blade shape is generated from the set of the design variables, and the aerodynamic characteristics of the rotor are computed by a rigid BEM solver by Moriarty and Hansen [59]. This module has been integrated in the data-flow of the *free-form* algorithm to perform the computation of the static $C_p - TSR$ curves of the wind turbine, from which it is possible to compute the ideal regulation trajectory (see for example Bottasso et al. [60]). From the regulation trajectory and the knowledge of the Weibull distribution, the program is able to compute the theoretical AEP . Since the rotor is rigid, losses in energy production due to the flexibility are not directly accounted for. However, it is still possible to customize the simulations by including the vertical shear on the turbine and by enabling or disabling the hub and tip losses models.

Loads and deformations

The choice of a suitable subset of load-cases is a crucial one when setting up a system-level optimization process. In fact, international certification guidelines typically require to perform a full range of dynamic simulations in order to prove the structural integrity of the machine under a variety of loading conditions [61, 62]. While this practice is highly recommendable in the context of certification, it is certainly not feasible in a design-and-optimization framework. Thus, one fundamental choice of any integrated design program concerns what level of detail must be attained in the simulations. In the *free-form* algorithm, we reduced the loading conditions to a minimum, in order to favour the computational speed and to manage a high number of design variables. Still, we put a lot of care in ensuring that the level of modelling was sufficient to support a truly aero-structural interaction. In the algorithm, then, the set of the DLC is reduced to just two families of simulations: a *pseudo* DLC 1.1 and a *pseudo* DLC 6.2. Both sets are performed by the multi-body simulation software Cp-Lambda developed by Bottasso and Croce [63], in which each blade is modelled as a one-dimensional flexible beam. Each blade is described by a lifting line, whose airfoil data are taken from XFOIL, and by a flexible beam whose spanwise data are computed from the sectional model discussed below. Both *pseudo* DLC 1.1 and 6.2 are based on static simulations: the former are performed by imposing the control parameters of the turbine, i.e. collective pitch, wind speed and rotor speed computed from the regulation trajectory. The latter are done assuming the wind turbine is parked, with the rotor in idling and the blades fully pitched towards feather. Several simulations are done by varying the yaw angle of the machine, in order to account for the extreme wind coming from different directions. The choice of these two families is based on experience: in particular DLC 6.2 are usually responsible for the driving loads and displacement of the rotor. Even when DLC 6.2 are not the most striking cases they typically appear in the top positions of the load hierarchy, so that their use as a loading marker for a simplified model like the one we use in the *free-form* is broadly justified. It must be noticed that, with this arrangement, the total running time of the simulations is in the order of seconds.

Structural model

The 1D flexible beam model is completed by a spanwise distribution of mass, stiffness and inertia. These information are automatically computed at each section through the sectional analysis tool developed at DTU by Blasques [64]. The software implements a

surface algorithm based on the anisotropic beam theory developed by Giavotto et al. [65]. It allows to compute the sectional properties by taking as input the actual shape of the section, the stacking sequence of materials and the relative thickness of each layer. In this study, we assume that the topology of the section is fixed and based on the classic *three-cells* box depicted in Fig. 2.6 (left). This assumption is not particularly limiting, since this configuration is widely adopted by most blade manufacturers, however, it will be easy in future developments of the code to include additional topologies in order to generalize the formulation.

Figure 2.6: *Three-cell section (left) and surface mesh of the structural members (right).*

The stacking sequence, that is, the order of lamination of the different layers, is defined as part of the input of the algorithm. Likewise, the properties of each material along the section must be specified in dedicated input forms. During the design, the geometry of the section is controlled by the optimization loop, which actively modifies the airfoils, where the thickness of each structural component can be defined as part of the input or directly included in the array of the design variables. In both cases, the initial distribution of thickness of a certain component must be specified at an arbitrary number of sections, while thickness at intermediate stations is recovered by interpolation. Once the input have been produced by the algorithm, a 2D Finite Element mesh is automatically generated on all the different elements, as shown in Fig. 2.6 (right). Then, the algorithm yields the sectional mass and inertia properties, as well as a fully populated stiffness matrix which accounts for the couplings (e.g., flap-torsion, flap-lag) induced by the use of composite anisotropic materials. The total structural mass can be easily determined at this point through a simple integration of the distribution of mass per unit length. Then, the *free-form* algorithm allows to add parasitic masses like bonding, adhesive, paint, lightning protection and so on which are computed through chord-dependent or surface-dependent empirical models. The sum of the structural and parasitic mass allows to obtain the total blade mass. After solving a required number of sections, it is possible to supply the resulting distributions of mass, stiffness and inertia to the structural model of Cp-Lambda, in order to perform the required simplified DLC. In the simplified methodology of the *free-form*, the extra-diagonal terms of the stiffness matrix are neglected, so that aero-elastic couplings are not accounted for. Similar distributions are supplied to the module BModes developed at NREL which has been included in the algorithm to compute the frequencies of the blade. This action could actually be performed by Cp-Lambda, however, the Arnoldi method used by the latter is much more time-consuming.

Once the simplified DLC are finished, the most demanding load combination is derived and supplied to the sectional solver for a second analysis, in which stress and strain are computed for each structural component, so that the structural integrity of the blade can be verified at each section through the dedicated constraints.

2.3.4 Cost of energy

As discussed in Chapter 1, system design algorithms for wind turbines should aim at the reduction of the COE (see [7]). In this work, the basic cost model is the one developed at the NREL and presented by Fingersh et al. [66, 67, 68, 69]. In this model, hereafter referred as *Scaling model*, the COE is expressed as follows:

$$\text{COE} = \frac{\text{FCR} \cdot \text{ICC}(\boldsymbol{p})}{\text{AEP}(\boldsymbol{p})} + \text{AOE}(\boldsymbol{p}), \tag{2.4}$$

where AEP is the net annual energy production, FCR is the fixed charge rate, ICC the initial capital cost, and AOE the annual operating expenses. This scaling-based cost model allows to draw a direct relationship between the design variables included in the optimization and the cost of energy. This is summarized by the expressions $ICC = ICC(\boldsymbol{p})$, $AEP = AEP(\boldsymbol{p})$ and $AOE = AOE(\boldsymbol{p})$ which basically state that the main parameters of the cost model can be computed from the knowledge of few parameters of the wind turbine which depend on the optimization variables $\boldsymbol{p}$. At each iteration, the cost of each sub-component of the turbine is computed from the knowledge of radius, blade mass, AEP and other parameters through dedicated scaling laws. Similarly, it is possible to compute costs for the commissioning, operation and decommissioning of the plant. The main limitation of this model is related to the reliability of the scaling relations, which were derived by fitting existing data from several projects in the past [70, 71, 72]. As the new generation of wind turbines approaches, some doubts on the validity of these laws for megawatts-size turbines arise. This is particularly true for the computation of the blade individual cost, which is determined as a function of either the rotor radius or the blade mass. These semi-empirical relations maintain a good validity as well as the design choices do not steer too much from the considered case studies, however, some limits of the model arise because the costs associated to the materials and those arising from the labour process are not directly taken into account. In the *free-form*, it is alternatively possible to compute the blade cost through an industrial estimator developed at SANDIA [73]. With this option, it is possible to account directly for the material unit cost and for labouring/equipment costs, which widely vary according to the geographic location of the manufacturing plant. In the following, we refer to this second method as Industrial model and we show how switching between the two models can dramatically influence the outcomes of the *free-form* design.

2.3.5 Constraints

To ensure the physical meaning of optimal solutions, several constraints from international certification guidelines [62, 61] are applied. For generality, each constraint is expressed in a non-dimensional form as follows:

$$c_i = \pm \frac{g(\boldsymbol{p}) - \alpha g_0(\boldsymbol{p}_0)}{g_0(\boldsymbol{p}_0)} \leq \epsilon_i \tag{2.5}$$

where $g(\boldsymbol{p})$ is a certain function of the design parameters $\boldsymbol{p}$, $g_0(\boldsymbol{p}_0)$ is a reference value, α is a multiplicative factor of choice, ϵ_i is a given tolerance related to the maximum allowable constraint violation and the actual sign $\pm$ depends on whether the constraint is posed in a *higher than* or in a *lower than* form. Given the simplified nature of the *free-form*, only a limited set of constraints was considered. Such subset was selected in order to be simple and not excessively expensive to compute, but at the same time complete enough to achieve realistic solutions:

- Resonance avoidance: the first flap-wise frequency of the blade must be higher than the N_b*-per-revolution*, where N_b is the number of blades. This avoids resonance and hence vibrations. Since the first flapwise frequency depends mainly on the out-of-plane stiffness of the blade, such a constraint has an impact on the thickness of the airfoils and of the structural elements, particularly the spar caps.
- Structural integrity: at each section, the local stresses are required to be lower than the corresponding allowables in order to ensure that the blade can withstand ultimate loads.
- Maximum tip displacement: this must be lower than the blade/tower clearance, in order to avoid fatal collisions.
- Geometric consistency: when the airfoils are optimized, their shape might be modified significantly by the optimizer. This constraint forces the relative thickness to be monotonically non-increasing from the root to the tip of the blade.
- Maximum operating C_L: this ensures that each airfoil operates far enough from the stall when the wind turbine is in operating (i.e.rated) conditions.

Other simple constraints may be considered, for example to limit the maximum chord or the spanwise rate of change of the structural thickness.

2.4 Applications

In this Section, we present applications in which the *free-form* is used to conduct the design of multi-MW rotors. Some interesting design problems are investigated like the impact of different cost models on the design, the influence of the materials and a preliminary combined optimization of the rotor *and* the radius.

2.4.1 Influence of the cost model on the design of a 2 MW rotor

In the first case study we investigate how the choice of different cost models, namely the scaling and the industrial ones discussed in § 2.3.4 influences the outcomes of the aero-structural design. The test is performed on a 2 MW onshore wind turbine, whose design has been carried out at the Politecnico di Milano for the Italian home market. The main features of the turbine are listed in Tab. 2.1.
The definition of the blade includes 5 different airfoils of the DU family developed at TU Delft by Timmer and van Rooij [74]. The non-dimensional thickness of these airfoils ranges from 18 to 40 %, as summarized in Tab. 2.2. The Table reports also the spanwise position of each airfoil and a flag which specifies if the airfoil is active for optimization or not. All the active airfoils are added to the *free-form* optimization while, on the contrary, the twin cylindrical sections at root are not optimized. XFOIL simulations are performed in viscous *regime* at Reynolds 5 millions. The transition is left free on both surfaces, whereas the value of the exponent n in the transitional model is 9.
The distribution of chord is controlled by 9 degrees of freedom, while the twist by 8. The thickness of the shell, as well as that of the two shear webs is frozen, while the thickness of the spar caps is divided into 8 stations and added to the set of the design variables. The total number of design variable is 100, as summarized in Tab. 2.3.
The goal of this test is to study how different choices of the cost model impact the optimal aero-structural design. To this end, we perform two redesigns of the **Baseline 2 MW**

Table 2.1: *Baseline 2MW: main turbine characteristics*

Class	IEC IIIA
Number of blades	3
Rotor orientation	Clockwise, upwind
Control	Variable speed, collective pitch
Cut-in speed	3 m/s
Cut-out speed	25 m/s
Rated power	2.0 MW
Rotor radius	46.2 m
Hub radius	1.2 m
Max chord	3.8 m
Cone angle	1.0 deg
Tower clearance	5.54 m

Table 2.2: *Baseline 2MW: airfoils*

Number	Active	Airfoil	Thickness %	Position $[-]$
1	No	Cylinder	100	0
2	No	Cylinder	100	0.0222
3	Yes	DU00-W2-401	40	0.1289
4	Yes	DU97-W-300	30	0.2844
5	Yes	DU91-W2-250	25	0.4033
6	Yes	DU93-W-210	21	0.5567
7	Yes	DU95-W-180	18	1.0000

Table 2.3: *Baseline 2MW: design variables*

Component	Parametrization	No. of design variables
Airfoil 3	4x 3rd-order Bézier	15
Airfoil 4	4x 3rd-order Bézier	15
Airfoil 5	4x 3rd-order Bézier	15
Airfoil 6	4x 3rd-order Bézier	15
Airfoil 7	4x 3rd-order Bézier	15
Chord	3rd-order + 4th-order Bézier	9
Twist	5th-order Bézier	8
Spar caps thickness	Direct discrete points	8
	TOTAL:	100

assuming that the spar caps are made of carbon. In the first, we estimate the blade cost with the Scaling model, where the blade cost is basically a function of its mass. In the

second run, we use instead the Industrial model, so that material, labouring and equipment costs are accounted. The mechanical properties of the unidirectional carbon fiber are listed in Tab. 2.4. We assume that the other structural components are made of glass, whose properties are also listed in the Table. We assume that the shell is laminated with a triaxial texture, while the shear webs are made of biaxial. Data of the unidirectional glass are also provided for completeness, and to highlight different unit prices between glass and carbon.

Table 2.4: *Baseline 2MW: materials*

Properties	Units	UD Glass	UD Carbon	Biaxial	Triaxial
E_{11}	[GPa]	38.24	115	9.73	28.54
E_{22}	[GPa]	8.62	7.56	9.73	10.28
ν_{xy}	[-]	0.259	0.300	0.596	0.438
G_{12}	[GPa]	3.50	3.96	10.91	6.47
ρ	[Kg/m3]	1901	1578	1874	1888
$\sigma_{x\ max}$	[MPa]	688.4	1317	92.0	513.8
$\sigma_{x\ min}$	[MPa]	478.0	625.1	92.0	356.8
$Price$	[$/Kg]	2.97	26.4	2.97	2.97

The main results of the two *free-form* designs are summarized in Tab. 2.5, where the solution obtained with the Scaling cost model is compared against the one obtained with the Industrial one. Remarkably, the two solutions achieve a similar COE and a comparable blade mass. However, it is interesting to see that the solutions differ significantly in their aero-structural definition. Fig. 2.7 shows the chord distribution of the two solutions and the thickness of the unidirectional carbon fiber in the spar caps. We see that when the Industrial model is employed, the optimal design has a greater solidity and much thinner spar caps: this is certainly a consequence of the high unit price of the carbon fiber, which is directly accounted by this model. The conclusion is that, when the unit price is considered, the optimizer tries to minimize the mass of the spar caps in order to limit the associated costs. This is done in part by a larger chord and in part by designing thicker airfoils, as shown in Fig. 2.8. The picture shows the non-dimensional thickness of the blade and the spanwise aerodynamic efficiency C_L/C_D as computed during nominal operating conditions.

Table 2.5: *Baseline 2MW: KPIs*

KPI	Units	Carbon - Scaling	Carbon - Industrial	Difference
COE	[$/MWh]	41.75	42.08	+ 0.8%
AEP	[GWh]	8.12	8.06	-0.73%
C_P^*	[-]	0.49	0.48	-2.04%
Blade mass	[kg]	5522	5513	-0.17%
Blade cost	[k$]	75.8	77.8	+2.61%
Spar cap mass	[kg]	1412	1098	-22.2%
Spar cap cost	[k$]	37.3	28.9	-22.5%

The efficiency, in particular, confirms that when the optimizer has a direct feedback on the unit price of carbon, it decisively favours a lower thickness of the spar caps. Quite naturally,

this comes at the expenses of the aerodynamic performance of the rotor. This is actually a counter-intuitive result, since a natural thought would be to use carbon to support the implementation of thinner airfoils and to increase the aerodynamic efficiency of the rotor. On the contrary, this study shows how the *free-form* chooses automatically to trade some of the efficiency in favour of a lighter structure, thus reducing the cost of the spar caps. Tab. 2.5 shows that, indeed, the mass and cost of the spar are broadly reduced.

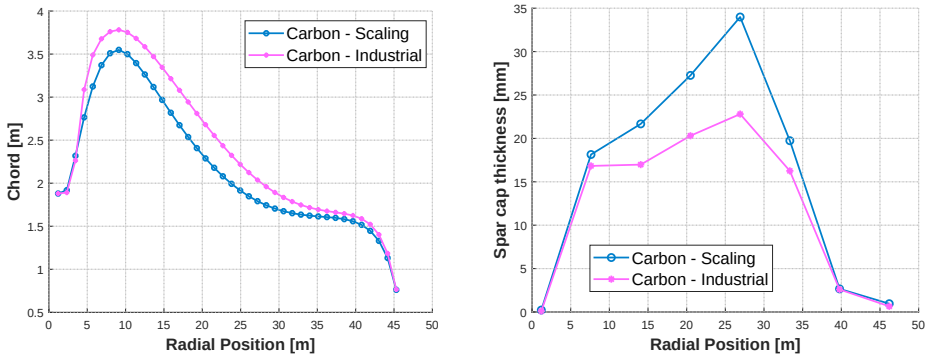

Figure 2.7: *Optimized 2 MW: spanwise chord distribution (left) and thickness of the spar caps (right).*

This trade-off is also visible in the design of airfoils. Figure 2.9 shows the optimal design achieved in both cases by the airfoil number 5. The plot on the left compares the optimal shapes, while the one on the right compares the efficiency of the airfoils, which is given in the form of a C_L *v.* $Efficiency$ curve. Similar information are given in Fig. 2.10 for airfoil number 6. Again, it is clear how the optimizer favoured thicker, less efficient airfoils when its main goal was to reduce the cost, of the spar caps. It is remarkable to notice that the otpimal design of airfoil 5 automatically includes a flatback configuration: through this design, in fact, it is possible to further increase the sectional area of the airfoil, which contributes to compensate for the loss of stiffness due to the thinner spar caps. A partial conclusion is that the choice of the cost model has a paramount importance on the evolution of the design and, if the algorithm is given sufficient authority to modify the design, results can differ significantly. Due to its ability to capture the cost of materials, we conclude that a blade cost computed by the Industrial model should be preferred in the context of this work.

2.4.2 Glass versus Carbon design of a 10 MW rotor

We now investigate the economic convenience of a glass and a carbon design applied to a 10 MW rotor. The starting model is the INNWIND.EU 10 MW wind turbine developed at DTU by Bak et al. [75]. The original model has been slightly simplified in order to comply with the requirements of the *free-form* algorithm and the latter version is here referred as **Baseline 10 MW**. The main characteristics of the turbine are listed in Tab. 2.6.
The original blade is equipped with the airfoils developed at the Flygtekniska Försöksanstalten (FFA) by Björck [76], which are listed in Tab. 2.7. Again, the two cylindrical sections are not optimized, whereas airfoils from 24 to 48% are. Viscous XFOIL simulations are performed for a Reynolds of 10 millions with free transition. The structural

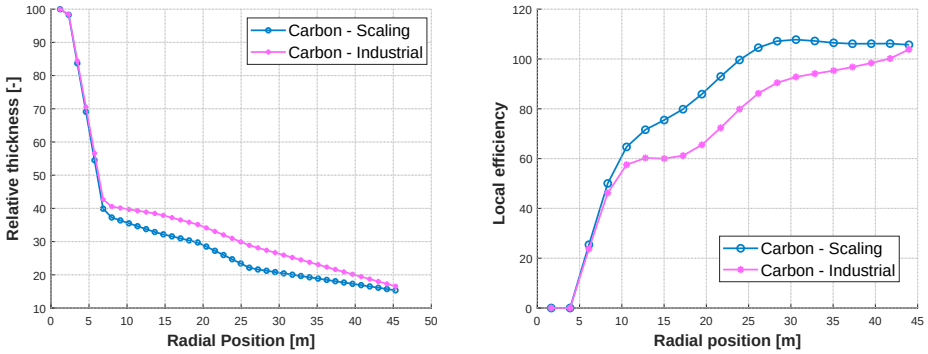

Figure 2.8: *Optimized 2 MW: non-dimensional thickness (left) and aerodynamic efficiency (right).*

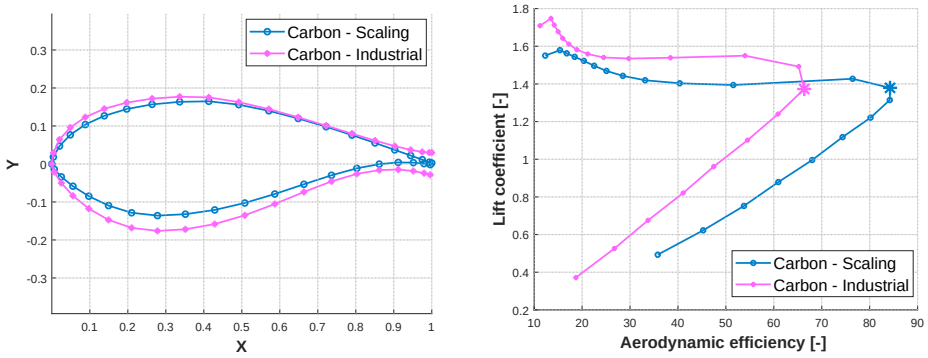

Figure 2.9: *Optimized 2 MW: optimal shape of Airfoil 5 (left) and aerodynamic efficiency (right).*

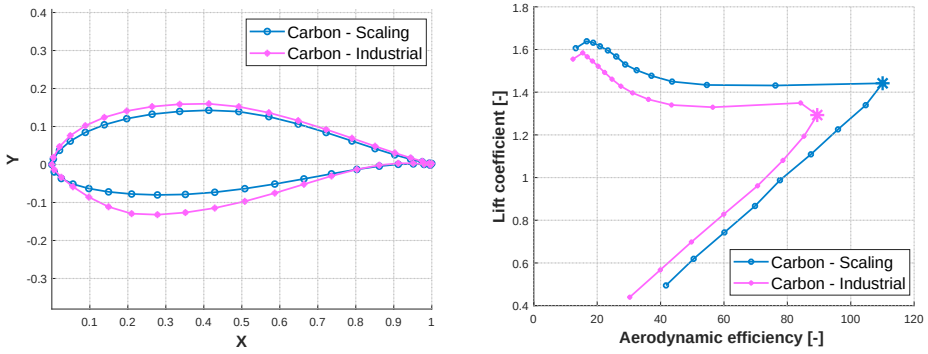

Figure 2.10: *Optimized 2 MW: optimal shape of Airfoil 6 (left) and aerodynamic efficiency (right).*

assumptions follow those of § 2.4.1, and in this study we test a first configuration in which

Table 2.6: *Baseline 10MW: main turbine characteristics*

Class	IEC 1A
Number of blades	3
Rotor orientation	Clockwise, upwind
Control	Variable speed, collective pitch
Cut-in speed	4 m/s
Cut-out speed	25 m/s
Rated power	10.0 MW
Rotor radius	89.17 m
Hub Radius	2.8 m
Cone angle	2.5 deg
Tower clearance	18.34 m
Maximum tip deflection	12.38 m

the spar caps are made of glass fiber and a second one in which carbon is used. The properties of the materials are again listed in Tab. 2.4.

Table 2.7: *Baseline 10MW: airfoils*

Number	Active	Airfoil	Thickness %	Position $[-]$
1	No	Cylinder	100	0
2	No	Cylinder	100	0.0602
3	Yes	FFA-W3-480	48	0.2107
4	Yes	FFA-W3-360	36	0.2976
5	Yes	FFA-W3-301	30	0.3844
6	Yes	FFA-W3-241	24	0.5465
7	Yes	FFA-W3-241	24	1.0000

The goal of this second study is to use the *free-form* algorithm with the Industrial cost model to assess which design, between glass and carbon, is the most convenient. The main results are given in Tab. 2.8, which shows that the glass solution leads to a 0.8% reduction in the COE when compared against the Baseline. It is interesting to notice that the saving comes from an improvement of the AEP (+0.75%) and a reduction of the mass (-4.6%). The design of the glass solution is mainly constrained, like the Baseline 10 MW, by the maximum tip deflection, and in this view it is interesting to notice that the optimizer managed to slightly reduce the spar cap thickness as shown in Fig. 2.11 (right). The inevitable drop in stiffness is compensated by an increased blade planform (see Fig. 2.11 (left)). The optimal airfoils are generally thinner, which gives a better efficiency and a higher power coefficient than the Baseline. The distribution of percent thickness is shown in Fig. 2.12 (left), while the aerodynamic efficiency C_L/C_D is reported on the right.
The optimal carbon design, on the contrary, leads to a COE which is about 0.8% higher than the Baseline. Both the AEP and the blade mass are improved, although the most driving constraint is given by the local stress and strain on the sections, and in particular in

Table 2.8: *Baseline 10MW: KPIs*

KPI	Units	Baseline 10 MW	Glass	Carbon
COE	[USD/MWh]	71.88	71.31 (-0.79%)	72.44 (+0.78%)
AEP	[GWh]	49.87	50.24 (+0.75%)	50.26 (+0.75%)
C_P^*	[-]	0.48	0.49 (+2.3%)	0.49 (+2.3%)
Blade mass	[kg]	40958	39077 (-4.6%)	33720 (-17.7%)
Blade cost	[k$]	280.5	274.5 (-2.11%)	451.5 (+61.0%)
Spar cap mass	[kg]	15317	13626 (-11.4%)	8730 (-43%)
Spar cap cost	[k$]	57.64	51.27 (-11.1%)	230.5 (+315%)

the spar caps. This leads the optimizer to reduce the chord with respect to the Baseline (see Fig. 2.11 (left)). Once again, the optimization works to reduce the thickness of the spar caps as much as possible. Looking at the results of Tab. 2.8, it is interesting to see how the mass related to the spar was reduced by more than 40% for this solution. This is in part due to the intrinsic lower density of carbon, but also to the heavy reduction of thickness in the structural elements (see Fig. 2.11 (right)). However, the unit cost of carbon is so high that those advantages were not sufficient to reduce the COE and, in particular, the cost associated to the spar.

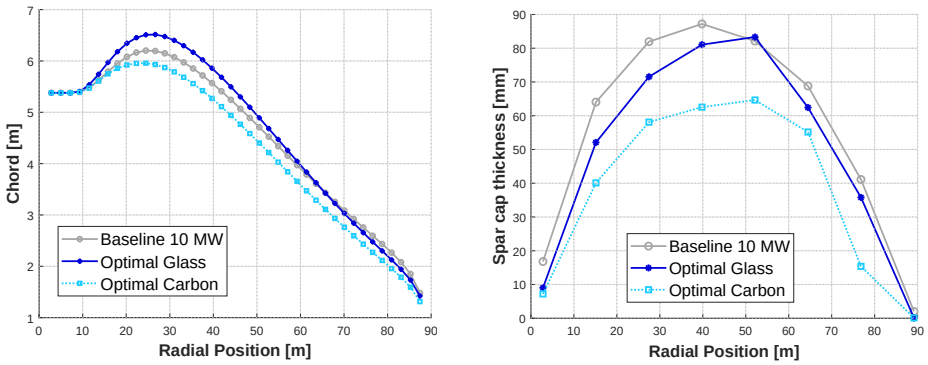

Figure 2.11: *Optimized 10 MW: chord (left) and spar caps thickness (right).*

The optimal shapes of Airfoil 5, together with the corresponding efficiency curves are shown in Fig. 2.13, whereas Fig. 2.14 gives similar informations for Airfoil 6. In general, the optimal glass solution has thinner airfoils when compared to those of the Baseline. On the contrary, the optimizer tried to design thicker airfoils in the case of carbon, in order to reduce the thickness of spar caps: this solution is qualitatively similar to the one followed in the previous case study.

Considering that the current unit price of carbon made the optimal design not competitive against glass, it would be interesting to estimate which carbon price would. We conducted a series of designs in which the unit price of carbon was parametrized from 35 $/Kg to 10 $/kg. Looking at the results provided in Tab. 2.9, we see how carbon solutions become more and more convenient as the unit price of the material is reduced. It is possible to see how the previous trend is confirmed: as the price is lowered, the optimal solution achieves

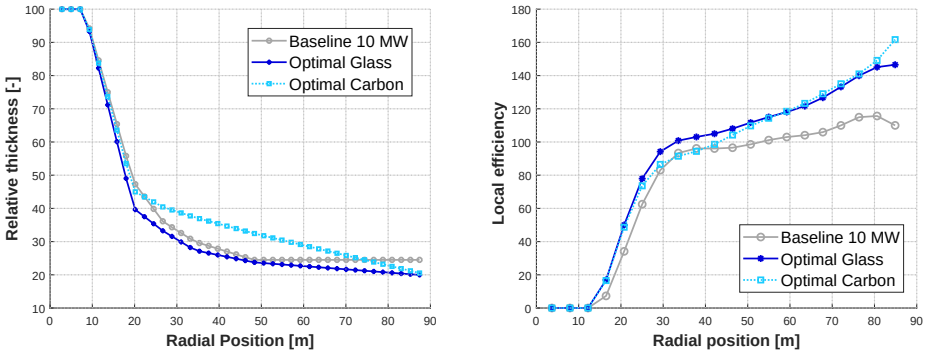

Figure 2.12: *Optimized 10 MW: non-dimensional thickness (left) and aerodynamic efficiency (right).*

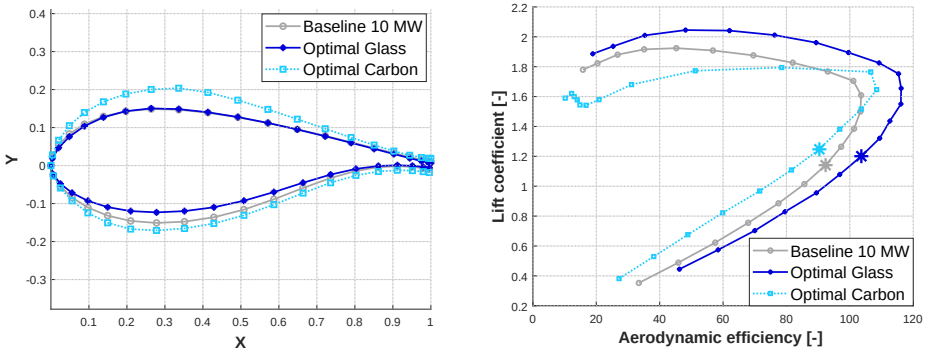

Figure 2.13: *Optimized 10 MW: optimal shape of Airfoil 5 (left) and aerodynamic efficiency (right).*

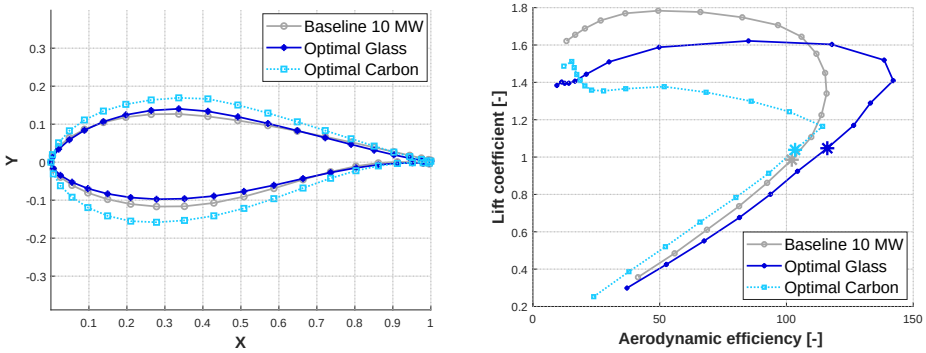

Figure 2.14: *Optimized 10 MW: optimal shape of Airfoil 6 (left) and aerodynamic efficiency (right).*

a lower rotor solidity [1] and the thickness of airfoils is heavily reduced (see Fig. 2.15) to

[1] Here the rotor solidity is intended as the ratio between the area physically occupied by the blades

obtain a higher efficiency. At the same time, a lower price means that the optimizer has a larger insensitivity on the spar cap thickness, and in fact, the spars are generally thicker as the price decreases. From these results we conclude that, in the framework of the *free-form* design, a unit price of 10 \$/Kg would result in a COE similar to the one of the optimal glass solution.

Table 2.9: *10 MW parametric carbon design: KPIs*

KPI	Units	Glass	35 \$/Kg	26.4 \$/Kg	18 \$/Kg	10 \$/Kg
AEP	[GWh]	50.24	50.15	50.26	50.21	50.36
Rotor solidity	[%]	4.94	4.8	4.57	4.54	4.54
Spar cap mass	[kg]	13626	8136	8729	7978	10139
COE	[\$/MWh]	71.31	73.05	72.44	71.86	71.31

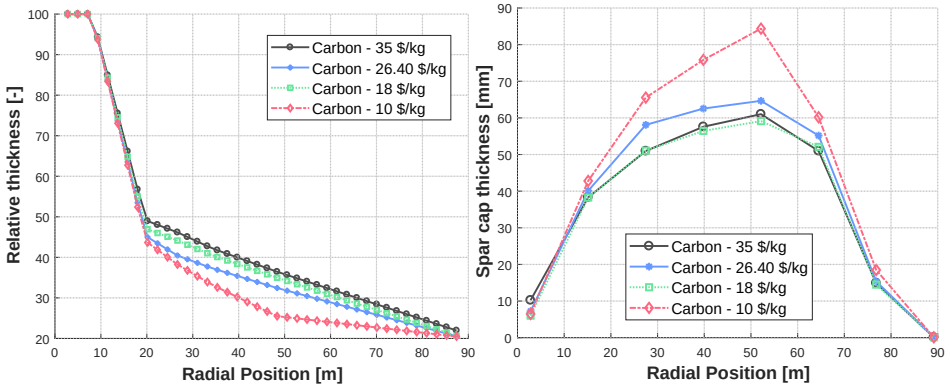

Figure 2.15: *10 MW parametric carbon design: non-dimensional thickness (left) and spar cap thickness (right).*

2.4.3 Free-form optimal rotor sizing

The last application we present in this Chapter investigates the possibility to include the rotor radius in the set of the design variables. To this end, we performed two different case studies in which the rotor radius was optimized together with the other design variables. Both designs start from the Baseline 10 MW. The first run allows the optimizer to size the rotor according to the original setup of the *free-form* approach, without additional constraints. For this reason, we identify this solution simply as **Optimal R**. In the second run, we introduced an additional constraint which forces the total rotor thrust to be lower or equal than the initial. This configuration is called **R + Thrust**. Table 2.10 gives an overview of the main results. Both the thrust-free and the thrust-constrained solutions evolved towards a larger radius, and this clearly increases the AEP of the two rotors. Both solutions attain a better COE than the Baseline. However, the optimization differ according to the different formulations of the problem. When the thrust is unconstrained, the solution

and the nominal area of the rotor disk.

achieves a higher elongation of the rotor, and thus, the best cost reduction. In this case, the aero-structural design is constrained by the maximum deflection so that, to support the longer blade, the optimizer increases also the chord (see Fig. 2.16 (left)). The percent thickness of airfoils shown in Fig. 2.17 (left) shows that the optimization led to thinner airfoils in the outboard part of the blade whereas an interesting result is that the thickness was increased in the region between 25 and 50 meters. This seemingly strange result can be explained by looking at Fig. 2.17 (right) which shows the value of the stress constraints as computed at 12 stations along the spar caps. As we see, probably due to the larger planform, the stress constraint is active in sections 4 to 7, which correspond to the area of increased thickness. It is interesting to observe that, in this area, the optimizer evolved automatically toward thick airfoils and lower efficiency: (see Fig. 2.18 (left)). This region works at sub-optimal induction (see Fig. 2.18) (right), and thus, the optimizer moderately evolved towards a Low-Induction Rotor. The latter is a concept for large turbine which has been recently proposed by several Authors [9, 6, 77]. This result partially contradicts our previous findings [39], however, in that preliminary version of the *free-form*, the tip displacement constrain was still not implemented.

Table 2.10: *Optimal rotor sizing: KPIs*

KPI	Baseline 10 MW	Optimal R	R + Thrust
Radius [m]	89.17	97.4 (+9.2%)	93.07 (+4.4%)
AEP [GWh]	49.87	53.09 (+6.5%)	51.60 (+3.5%)
Blade mass [kg]	40958	45413 (+10.9%)	39964 (-2.4%)
Thrust [kN]	1508	1572 (+4.3%)	1523 (+1.0%)
COE [$/MWh]	71.87	70.16 (-2.4%)	70.6 (-1.8%)

In the optimal sizing with thrust constraint, the rotor increase was limited. This is because the thrust constraint became active on the design, preventing further stretching of the blade. Looking at Fig. 2.16 (right) it is possible to see how the operating thrust, for this rotor is correctly kept within 1% of that of the Baseline, in accordance with the tolerance set on all constraints. In this second case, the design of airfoils was still oriented towards thinner shapes, with the exception of a tiny region between 28 and 45 meters. However, the increase of thickness in this part of the blade is moderate when compared against the unconstrained solution, so that a globally higher efficiency can be achieved along the blade.

2.5 Conclusions

In this Chapter, we proposed an innovative design methodology in which the airfoils along the blade are optimized together with a typical set of aero-structural variables like chord, twist and the thickness of the structural components. The idea is to develop a methodology in which the optimal design is no longer limited, or constrained, by the initial choice of the airfoils. Due to the high number of design variables, the design framework is forcibly simplified, however, we presented several applications in which the *free-form* approach was employed to manage non-trivial design challenges. The findings show that the methodology has sufficient robustness and flexibility to produce consistent optimal solutions and, in some cases, some unexpected results were obtained. A first conclusion is that the choice of the cost model can affect significantly the aero-structural optimum. In particular, it is

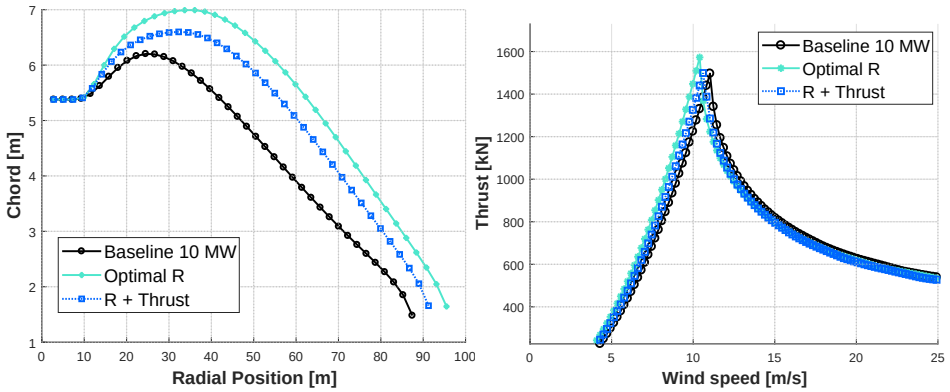

Figure 2.16: *10 MW optimal rotor sizing: chord (left) and nominal thrust curve (right).*

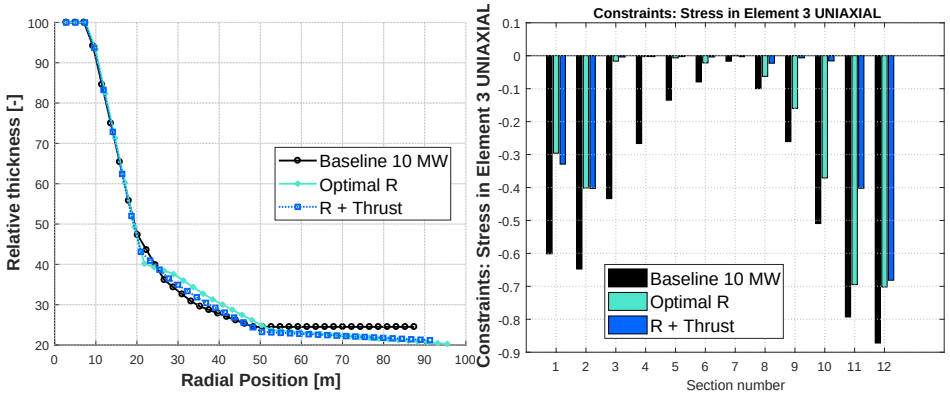

Figure 2.17: *10 MW optimal rotor sizing: non-dimensional thickness (left) and sectional stress constraints (right).*

highly recommendable that the unitary blade cost is computed through detailed models which account for material, labour and equipment cost. In this view, we also demonstrated how the *free-form* automatically trades aerodynamic efficiency in favour of light-weight rotors when the blade is made of expensive materials like carbon. Finally, we proposed an extension of the algorithm by including the rotor radius in the optimization loop: results show how the *free-form* can successfully manage an optimal rotor sizing by leveraging on all the design variables. In particular, we showed how the algorithm can automatically decide to reduce the efficiency of the airfoils in some parts of the blade if this represents an aero-structural optimal strategy.

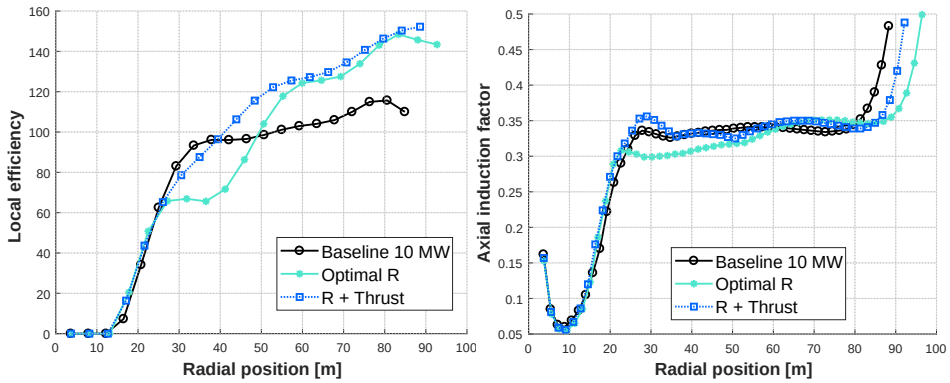

Figure 2.18: *10 MW optimal rotor sizing: aerodynamic efficiency (left) and axial induction factor (right).*

CHAPTER 3

Multi-level system design of wind turbines

In this Chapter we develop a second approach to the design of large wind turbines, based on the combination of highly-detailed numerical models and a dedicated multi-level optimization framework. The result is a System Design Optimization (SDO) scheme which allows to conduct fully-automated design tasks relying on a whole set of dynamic simulations of the entire system. The design philosophy is quite different from that of the *free-form* methodology developed in Chapter 2 and, in a way, complementary. We discussed how the *free-form* was conceived as an innovative method in which a huge variety of aero-structural variables are optimized together on the basis of selected simplified analysis. Here, on the contrary, we discuss the problem of including a full set of DLC directly within the optimization procedure, so that the resulting turbine could be designed on realistic load conditions from the very initial steps of the loop. The implications of such an approach on the design of very large turbines are potentially very important: modern wind turbines experience a variety of loads and cross-couplings which arise from different causes, in particular the high flexibility of the beam-like elements (blades, shafts, tower) and the important mass of some of the sub-components. It is widely accepted in the literature that such a combination of phenomena results in a complicated, and often fully-coupled response of the turbine [78, 5, 79], so that fundamental dynamic and aero-elastic behaviours should be definitely accounted for during a successful design effort. In the next Sections we discuss how the multi-body formulation offers a flexible and powerful tool for simulating the dynamics of wind turbines, then we discuss the development of our multi-disciplinary design suite `Cp-Max`. The algorithm is based on a multi-level architecture: an external design loop manages the optimization of few fundamental characteristics of the turbine, which are sized in order to minimize the COE. Then, for each perturbation of the external variables, a set of different sub-models performs the detailed design of specific components, which are optimized according to dedicated merit functions and constraints. Then, the resulting

workflow is a nested sequence of individual optimization problems which continuously influence one another and exchange data through a dedicated central bus. The underlying assumption of this construction, which differs significantly from the classic monolithic approach, is that the definition of the individual merit functions at the detailed design levels work in synergy with the overall COE minimization defined at the external level. We show in the following that, unlike many monolithic algorithms, this procedure allows to include a significant set of dynamic DLC so that, ideally, the optimal solutions obtained at the end of the process are automatically guidelines-compliant. In the following, we describe the assumptions behind the multi-level structure of `Cp-Max` and we detail the formulation of the external loop as well as those of the individual design submodules. For each design, we describe the corresponding optimization problem in terms of modelling, design variables, merit function and constraints. The development of `Cp-Max` here discussed starts from the findings of Gualdoni [80] and has been conducted in partnership with the Wind Energy Chair at the Technische Universität München.

3.1 Multi-body modelling of wind turbines

An integrated multi-disciplinary design scheme like the one implemented in `Cp-Max` must forcibly rely on an appropriate set of numeric simulations, from which it is possible to compute a variety of informations about ultimate and cyclic loads, component deflections, performance and integrity of the sub-systems. The simulations can be static or dynamic, and can support different layers of detail in the modelling according to the level of complexity required by the optimization loop. In `Cp-Max` all the simulations are performed by `Cp-Lambda`, an aero-servo-elastic simulation software based on the multi-body method developed by Bauchau et al. [81] and later adapted for wind energy applications by Bottasso et al. [82]. In this formulation, the system is represented through a set of fundamentals elements which can be arbitrarily assembled together from a library which includes beam models, rigid bodies, different joint models, actuators, sensors and boundary conditions. Since no *a-priori* assumption is made on the sequence of elements, it is possible to represent any typology of wind turbine by choosing a suitable combination from the library. To provide an example, Fig. 3.1 shows a possible `Cp-Lambda` representation of a classic horizontal-axis, three-bladed wind turbine with pitch, torque and yaw actuators.
The formulation exploits a finite elements description, which implies that no modal-basis reduction is performed on the flexible elements of the system. Cartesian coordinates are used for the geometric definition of the model and are referred to a unique inertial frame by means of suitable transformations, which allow to manage arbitrarily large rotations. Beam-like elements including blades, tower and shafts are defined through their associated curves, represented by means of Non-Uniform Rational B-Splines (NURBS) according to the formulation of Piegl and Tiller [83]. Each curve can assume an arbitrary shape in the three-dimensional space, thus supporting twisted, swept and pre-bent blades. Those elements are also intrinsically flexible and must be associated to a distribution of cross-sectional mass and stiffness properties, which can be defined with respect to the elastic, shear and gravity centers of the section or by providing the full 6x6 mass and stiffness at each section. This way, it is possible to correctly account for built-in structural couplings associated to non-zero extra-diagonal stiffness terms of anisotropic materials. The structural model of the beams is based on the non-linear composite beam theory developed by Bauchau [84], which accounts for transverse shearing deformations and torsional warping. Joints are modelled through holonomic or nonholonomic constraints, as required by the specific application, and are enforced by means of Lagrange multipliers. All joints can be

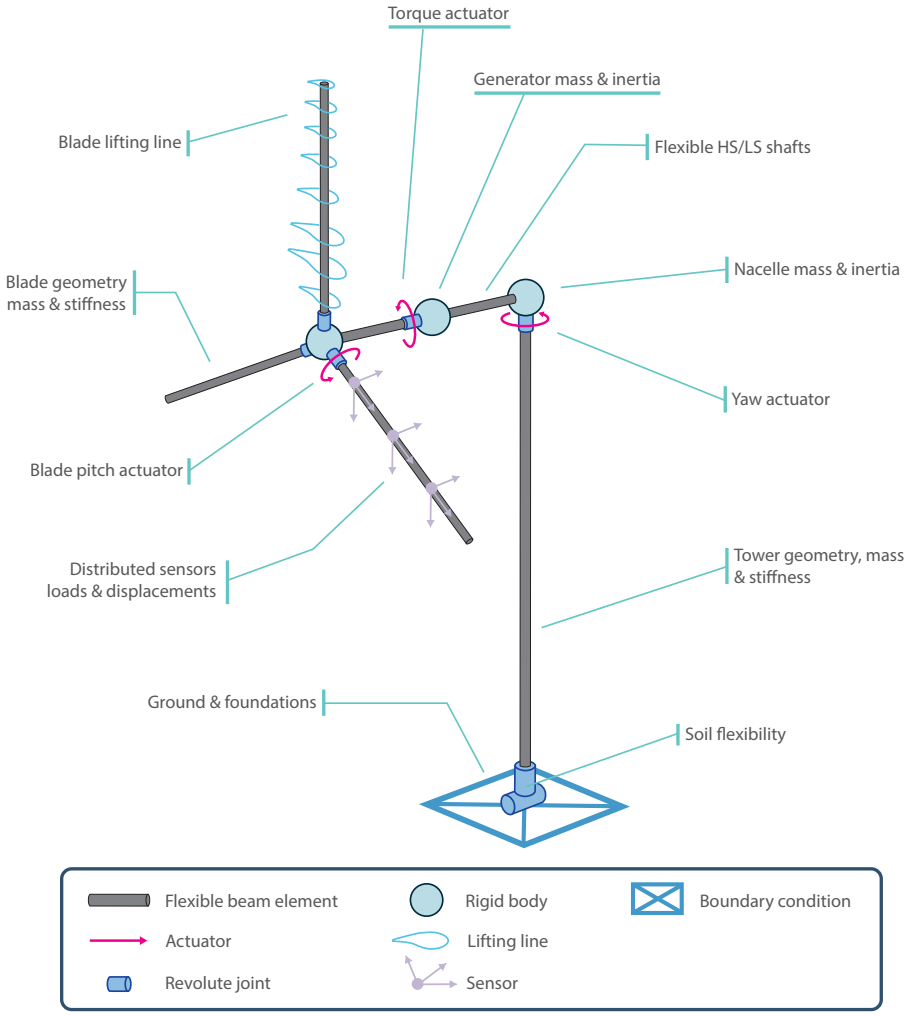

Figure 3.1: *Topological description of a wind turbine in* `Cp-Lambda`.

associated to non-linear internal springs, dampers, backlash, and friction models, so that localized flexibilities and losses can be modelled by means of equivalent joints. An example of such modelling is given in Fig. 3.1, where the flexibility of the ground is represented by a 4-degrees of freedom combination of joints.

The aerodynamics of the rotor is modelled by means of lifting lines, which provide the aerodynamic properties of the blades at each section. These are computed from the distribution of chord and require suitable airfoil tables to be defined, for different Reynolds numbers, at sectional level. The effects of an equivalent flap can be also modelled by introducing a further dependency on the flap deflection within the airfoil tables. The inflow over the rotor is computed by a classic BEM model based on annular stream tube with wake swirl [85]. Suitable corrections for hub and tip losses can be directly accounted for, while a dynamic correction for unsteady flows can be introduced according to the model by Pitt [86].

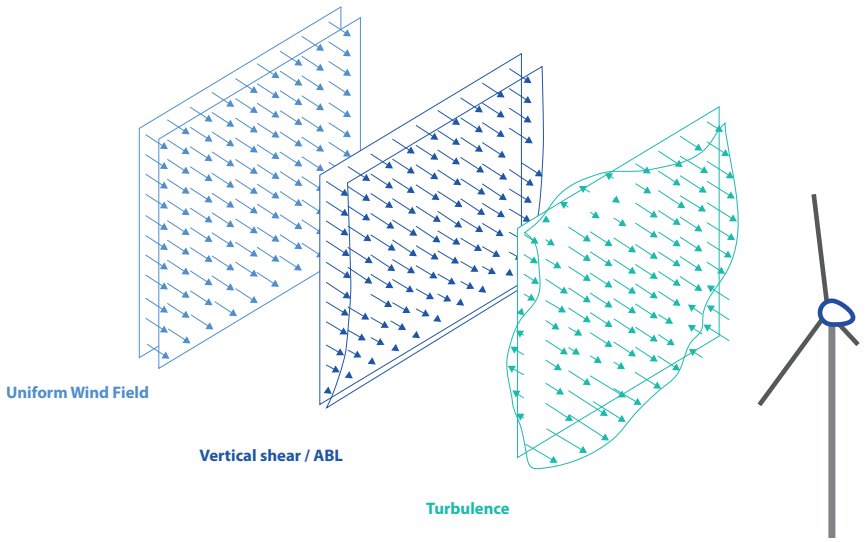

Figure 3.2: *Generation of the wind field in* `Cp-Lambda`.

The incoming wind conditions are defined on a dedicated spatial grid at the rotor plane. At each point of the grid, the three components of the wind velocity $[u, v, w]$ are applied as specified by an external wind source file. The latter can represent either deterministic gusts like the ones prescribed by the certification guidelines or fully-turbulent wind fields, which are usually generated for the required wind class and turbulent seed by the dedicated tool `TurbSim` [87]. Within the simulation, the externally-supplied wind field is superimposed to a uniform wind field and to additional wind models defined within the solver: these include waves and currents, tower shadow and vertical shear. Figure 3.2 gives a qualitative representation of the components of the wind field impinging on the turbine.

The regulation of the wind turbine is provided by an external control module developed by Riboldi [88], which allows to define and operate different control strategies for yaw, torque and collective blade pitch. The module is fully interfaced with `Cp-Lambda` so that, at each time step, the controller receives informations from the solver and produces the control inputs according to the chosen strategy. The control action is then performed by torque, pitch and yaw actuators, whose dynamics can be modelled by a 1st or a 2nd order system. This setup allows to modify, improve and define new control strategies without the need to recompile the solver and, when required, it operates as a gateway to third-party control modules.

This simulation tool allows to conduct a variety of analysis, both static and dynamic, which are expected during the optimization loop. At each level of design, specific subroutines automatically generate suitable multibody models and perform the necessary simulations up to a desired level of detail. A typical set of simulations includes the modal analysis of the isolated blade, the computation of the Campbell diagram, the run of the Cp-TSR curves and an arbitrary set of DLC for the characterization of the wind turbine performance. Additional simulations can be optionally added to the work-flow in order to perform *out-of-the-loop* specific analysis. Identification-based stability analysis, for example, are performed in this way.

3.2 Architecture of the program

The main feature of the integrated SDO approach here proposed is the nested/multi-level architecture shown in Fig. 3.3. The idea is to interface two different layers of design, one dedicated to the preliminary aero-structural optimization and the other conceived as a series of individual design modules which perform detailed design of specific wind turbine subcomponents. The main advantage of such construction is that it allows to combine the level of detail of highly-physical simulations with a high number of design variables typical of aero-structural design problems. Another important feature is that different design variables, which form a highly-heterogeneous set, are not treated all at the same level like it happens in monolithic approaches (see, for example, the *free-form* methodology discussed in Chapter 2). Vice-versa, the variables are dispatched among different design steps, so that quantities which bear similar effects on a certain merit function could be packed together and provide a better sensitivity to the optimization scheme. So, for example, variables with high influence on the overall design like the rotor height and radius are optimized at the same level whereas, for example, the structural thickness of the components are optimized together at another level. Clearly, the fundamental assumption behind this architecture is that the external loop *and* all the modules work together in the same direction, that is, the target of each design step must be coordinated to the others, in order to avoid the situation in which the design within a module evolves independently from that at the global/macro level. A detailed description of the algorithm and its developments can be found in several contributions (see for instance [8] [89] [90] [91]). In the following, we describe the global design strategy and the different submodules in order to highlight the features of the program, its capabilities and the aspects which required particular attention during the development.

3.2.1 Macro Design Loop

The Macro Design Loop (MDL) is the backbone of `Cp-Max`, since it manages the overall optimization of the wind turbine and the data-flow between the various submodules. Given a certain project, in terms of power rating and wind class, its main task is to conduct a *preliminary* design in which a selection of few important (Macro) parameters of the turbine is optimized in order to minimize the cost of energy. However, given the multi-level nature of `Cp-Max`, for each perturbation of those parameters one or more submodules at the inner level perform the *detailed* design of desired aspects of the wind turbine. This can be formalized through the following algorithmic structure:

$$(\boldsymbol{p_a^*}, \boldsymbol{p_b^*}, \boldsymbol{p_s^*}, \boldsymbol{p_g^*}, COE^*) = \texttt{MinCOE}(\boldsymbol{p_a}, \boldsymbol{p_b}, \boldsymbol{p_s}, \boldsymbol{p_g}, \boldsymbol{D}) \tag{3.1a}$$

$$COE^* = \min_{\boldsymbol{p_g}}(\texttt{ComputeCOE}(\boldsymbol{p_a}, \boldsymbol{p_b}, \boldsymbol{p_s}, \boldsymbol{p_g}, \boldsymbol{D})) \tag{3.1b}$$

$$(\boldsymbol{p_a^*}, \boldsymbol{p_b^*}, \boldsymbol{p_s^*}, \boldsymbol{p_g^*}) = arg(\min_{\boldsymbol{p_g}}(\texttt{ComputeCOE})) \tag{3.1c}$$

$$s.t.:$$

$$\boldsymbol{g_g}(\boldsymbol{p_a}, \boldsymbol{p_b}, \boldsymbol{p_s}, \boldsymbol{p_g}) \leq \boldsymbol{0} \tag{3.1d}$$

Equation 3.1a is written in the form $(\boldsymbol{Output}) = Function(\boldsymbol{Input})$ and shows that the module takes as input the array of the aerodynamic design variables $\boldsymbol{p_a}$ together with those containing the unknowns of the prebend ($\boldsymbol{p_b}$), the structure ($\boldsymbol{p_s}$) and the global/macro

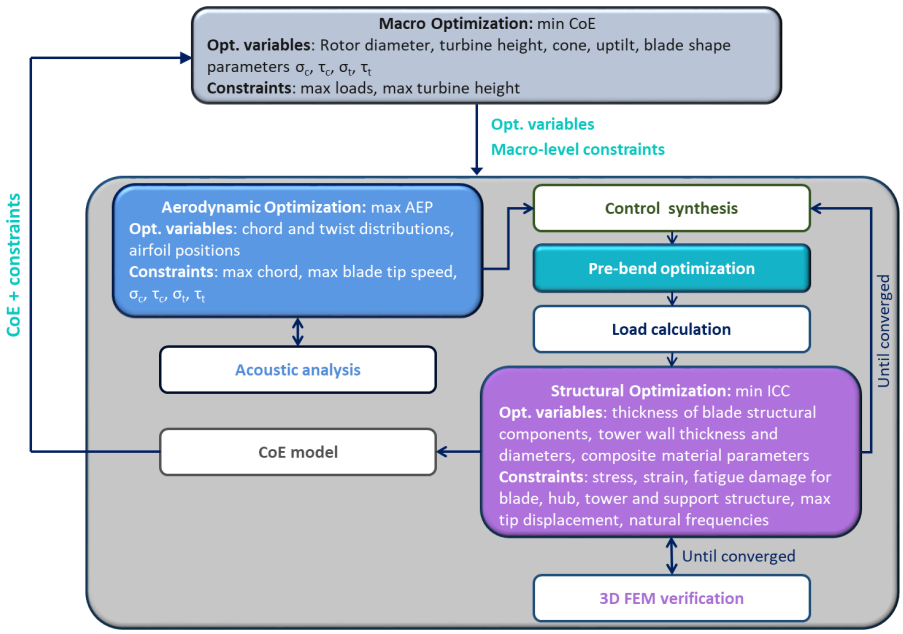

Figure 3.3: *Architecture of the Macro Design Loop.*

ones $\boldsymbol{p_g}$. The latter are directly optimized by the MDL, while the former by the individual submodules. A set of fixed input parameters is collected in the array $\boldsymbol{D}$ which includes quantities that remain frozen during the design stages. The canonical construction of $\boldsymbol{D}$ is:

$$\boldsymbol{D} = [\delta_{Hub},\ P_r,\ \mathcal{C},\ v_{in},\ v_{out},\ \boldsymbol{q}_{af},\ v_{tip_{max}},\ \boldsymbol{I_{DLC}},\ \boldsymbol{q}_s] \tag{3.2}$$

where δ_{Hub} is the rotor overhang, P_r is the the power rating, $\mathcal{C}$ the wind turbine class, v_{in} and v_{out} are, respectively, the cut-in and cut-out wind speeds of the turbine, $\boldsymbol{q}_{af}$ is a structure containing the geometry and the aerodynamic data of a given number of airfoils n_{af} defined along the blade. The input $v_{tip_{max}}$ is the the maximum tip speed, while $\boldsymbol{I_{DLC}}$ is a structure containing the set of the DLC considered during the design, together with their respective safety factors. Finally, $\boldsymbol{q}_s$ is a structure which contains topological data of the blade and tower internal layout:

$$\boldsymbol{q}_s = [\boldsymbol{\tau}_{sec},\ \boldsymbol{f}_{mat,b},\ \boldsymbol{f}_{mat,t},\ \boldsymbol{\phi}_{mat,b}(\eta),\ \boldsymbol{h}_t] \tag{3.3}$$

Here, $\tau^i_{sec},\ i = 1, ..., n_{sec,b}$ is a variable storing informations on the structural topology of the blade at each section (i.e. position of elements, number of webs, stacking sequence) and $n_{sec,b}$ is the number of sections considered in the structural description of the blade. The array $f^j_{mat,b}, j = 1, ..., n_{mat,b}$ lists the mechanical properties of the materials employed for the design of the blades, and $n_{mat,b}$ is the number of materials defined on the blades. Similar considerations apply for the materials of the tower, whose properties are listed in $f^j_{mat,t},\ j = 1, ..., n_{mat,t}$. The array $\phi^j_{mat,b}(\eta)$ describes the orientation along which the fibers of the j^{th} blade material are laminated. This property is important when anisotropic materials are employed, as their resulting properties depend on the actual direction of the laminate. Since, on the contrary, the tower is typically designed with steel,

which is isotropic, a similar structure is not defined for tower materials. Since the tower is assumed to be piece-wise cylindrical, $\boldsymbol{h}_t$ stores the relative height of each tower segment. All the previous informations refer to quantities or properties which are not optimized in the current version of `Cp-Max`, and thus, they are provided through Eq. 3.3 as part of the input.

The array of the global optimization variables $\boldsymbol{p}_g$ is defined as follows:

$$\boldsymbol{p}_g = [R, h_{Hub}, \theta_\pi, \gamma_b, \sigma_c^g, \tau_c^g, \sigma_t^g, \tau_t^g] \tag{3.4}$$

and includes the rotor radius R, the nominal hub height h_{Hub}, the rotor tilt angle θ_π, the blades collective coning angle γ_b and four additional shape parameters $\sigma_c^g, \tau_c^g, \sigma_t^g, \tau_t^g$ defined in Eq. 3.5. As discussed, the idea is to store within the global design variables array, a little number of fundamental features of the wind turbine, in order to collect together those parameters whose variation has a significant impact on the whole turbine design, and especially on the COE. In particular, the rotor radius is the variable whose evolution affects the design the most, as several cost items in the computation of the COE directly scale with the radius. For example, in the mentioned scaling cost model by Fingersh et al. [66], the value of the rotor radius directly affects the costs of the pitching system, the hub hardware including nose, shafts, spinner and cone, the yaw drive and the main bearing systems. Additional non-ICC costs scale with the rotor radius, like for example the assembly and installation cost. The choice of a certain hub height h_{Hub} for a certain wind class $\mathcal{C}$ is not imposed by the certification standards, then, it makes sense to find its value as part of a cost-minimizing optimization problem. In fact, a higher tower leads to a greater energy capture, but also to larger capital costs and higher components loading, so that identifying the best trade-off is not a trivial task. Both rotor tilt and coning angles θ_π, γ_b are fundamental parameters, as they typically affect the AEP of the turbine, but also the structural design. Higher values of tilt and cone, in fact, typically result in a reduction of the energy capture, as the rotor plane is twisted from its ideal plane normal to the free-stream, but also in a larger clearance between the blade and the tower, which might relieve the constraint of maximum blade deflection. Four shape parameters $\sigma_c^g, \tau_c^g, \sigma_t^g, \tau_t^g$ are introduced as part of the global design variables as a channel to connect the MDL with the individual design sub-modules, and in particular to the aerodynamic design. These parameters are defined as follows:

$$\sigma_c^g = \frac{3A_b}{A_\pi} = \frac{3\int_0^R c(r)dr}{\pi R^2} \tag{3.5a}$$

$$\tau_c^g = \frac{\int_0^R rc(r)dr}{A_b} \tag{3.5b}$$

$$\sigma_t^g = \frac{1}{100}\int_0^1 t(\eta)d\eta \tag{3.5c}$$

$$\tau_t^g = \frac{\int_0^1 \eta t(\eta)d\eta}{\int_0^1 t(\eta)d\eta} \tag{3.5d}$$

where A_b is the blade solid area, A_π is the ideal rotor area, $c = c(r)$ is the blade chord distribution as a function of the local radius r, $t = t(\eta)$ is the distribution of blade percent thickness as function of the non-dimensional length coordinate η. The detailed design of

the blade shape, in terms of chord, twist and percent thickness is not managed at the MDL-level: in fact, this would require a certain number of dedicated design variables which should be added to the array $\boldsymbol{p}_g$, with consequences on the computational time. As we discuss later in § 3.2.2, the blade shape is actually designed by the aerodynamic submodule, which performs a detailed sizing for the maximum AEP. The module performs a genuinely aerodynamic design, which means that, if the problem is not properly constrained, the evolution of the aerodynamic design is completely independent from the underlying structure, which is sized at a later stage. Within an economic perspective, the risks of such an approach are clear: it might happen that the aerodynamic design evolves toward a highly-efficient blade with low solidity and reduced sectional thickness. This would require to design a heavier structure and, ultimately, would achieve a high cost of energy. To avoid such kind of bad-positioning of the MDL optimization, the four shape parameters 3.5 are used to keep the aerodynamic design within certain limits. Those limits, in turn, are directly managed by the MDL on behalf of the aerodynamc design module. This allows to create a feedback between the macro design variables and the evolution of the aerodynamic design, in particular because the shape parameters are fed to the Aerodynamic Design Submodule as non-linear constraints. This mean, for example, that whenever the MDL changes the rotor solidity parameter σ_c^g, the aerodynamic design must ensure that the blade shape has exactly the prescribed solidity. Similar considerations apply to the other shape parameters: τ_c^g represents the *tapering* of the blade and it basically weights more the outboard sections to discourage the aerodynamic design to add too much solidity towards the tip. The third parameter σ_t^g, is a simple ratio between the area underlying the percent thickness distribution and an equivalent area computed for a uniform distribution of 100 percent thick airfoils. The last parameter τ_t^g is similar to the blade tapering, as it weights more the outboard sections. It is important to notice that these shape parameters are introduced only to connect the MDL with aerodynamic design, whereas no direct connection is created between the MDL and the structural design. The latter, in fact, is performed for a frozen aerodynamic shape, under the assumption that a moderate variation of the structural sizing would not dramatically affect the AEP of the wind turbine, so that there is not the need to introduce macro parameters to bound the optimization.
The main subroutine of the MDL is given by Eq. 3.1b, whose work-flow can be split into the following operations:

$$COE^* = \min_{\boldsymbol{p_g}}(\texttt{ComputeCOE}(\boldsymbol{p_a}, \boldsymbol{p_b}, \boldsymbol{p_s}, \boldsymbol{p_g}, \boldsymbol{D})) \tag{3.6a}$$

$$(\boldsymbol{p_a^*}, AEP^*) = \texttt{MaxAEP}(\boldsymbol{p_a}, \boldsymbol{p_b}, \boldsymbol{p_s}, \boldsymbol{p_g}, \boldsymbol{D}) \tag{3.6b}$$

$$(\boldsymbol{r}_\epsilon^*) = \texttt{CreateControlLaws}(\boldsymbol{p_a^*}, \boldsymbol{p_b}, \boldsymbol{p_s}, \boldsymbol{p_g}, \boldsymbol{D}) \tag{3.6c}$$

$$(\boldsymbol{p_b^*}, A_\delta^*) = \texttt{OptimizePrebend}(\boldsymbol{p_a^*}, \boldsymbol{p_b}, \boldsymbol{p_s}, \boldsymbol{p_g}, \boldsymbol{D}, \boldsymbol{r}_\epsilon^*) \tag{3.6d}$$

$$(\boldsymbol{p_s^*}, ICC^*) = \texttt{MinICC}(\boldsymbol{p_a^*}, \boldsymbol{p_b^*}, \boldsymbol{p_s}, \boldsymbol{p_g}, \boldsymbol{D}, \boldsymbol{r}_\epsilon^*) \tag{3.6e}$$

$$\tilde{AEP}^* = \texttt{UpdateAEP}(\boldsymbol{p_a^*}, \boldsymbol{p_b^*}, \boldsymbol{p_s^*}, \boldsymbol{p_g}, \boldsymbol{D}, \boldsymbol{r}_\epsilon^*) \tag{3.6f}$$

$$COE = \texttt{CostModel}(\tilde{AEP}^*, ICC^*, \boldsymbol{p_a^*}, \boldsymbol{p_s^*}, \boldsymbol{p_g}, \boldsymbol{D}) \tag{3.6g}$$

For each perturbation, or evaluation, of the global design array $\boldsymbol{p_g}$, the subroutine 3.6a is called to evaluate the COE of the corresponding solution. Within the subroutine, different design submodules are called in sequence: initially, the Aerodynamic Design Submodule 3.6b conducts an aerodynamic optimization of the rotor shape to maximize the AEP. This gives the optimal combination of the aerodynamic design variables $\boldsymbol{p_a^*}$, which is then supplied along the data-flow to the subsequent operations. Once the optimal aerodynamic

shape has been established, the Control Synthesis Tool 3.6c computes the regulation trajectory of the turbine according to the chosen control strategy. This gives the control laws $\boldsymbol{r}_{\epsilon}^{*}$, which are then shared to the following modules. Starting from the control laws, the Prebend Design Submodule 3.6d optimizes the spanwise prebend of the blades through an AEP-preserving criteria, giving as result the optimal prebend $\boldsymbol{p}_{\boldsymbol{b}}^{*}$. Then, within the Structural Design Submodule 3.6e a two-steps procedure allows to optimize the structure of the blade and tower in order to minimize the ICC. The evolution of the structural design is then clearly influenced by how the ICC is computed in the selected cost model. Within this loop, the relevant ultimate and fatigue loads, as well as the component's displacements, are continually updated by running an arbitrarily-wide set of DLC, so to give a structural optimal design which is coherent with its own loads. Once the loop is over, the optimal structure $\boldsymbol{p}_{\boldsymbol{s}}^{*}$ is found and the estimation of the AEP is repeated within a dedicated subroutine 3.6f to account for the possible modifications occurred during the various design steps. This gives the refined energy yielding, $\tilde{AEP}^{*}$, which is then used together with the optimized ICC and several other parameters to compute the COE 3.6g according to the desired model.

As discussed in Chapter 2, it is important that the merit function of a system design tool is based on the cost of energy, since it represents the actual driver of most wind energy applications (see for example Ning.et.al [7]). Like the *free-form* algorithm, `Cp-Max` supports different cost models, which can be arbitrarily selected at the beginning of the optimization. Two of the available cost models are based on scaling laws: the first is based on the already discussed NREL model by Fingersh et al [66] in its original version. However, it must be kept in mind that this model is reliable only for mid-sized, onshore wind turbines. For this reason, starting from the same NREL model, a new version has been updated and revised as part of the activities of the INNWIND.EU consortium [92]: the latter has been formulated specifically for multi-megawatts offshore turbines and provides upgraded scaling laws for most of the subcomponents. Additionally, the INNWIND cost model includes the rated torque in the evaluation of drive train and generator costs, which makes this model particularly suitable for the lightweight design studies investigated in this work. Within `Cp-Max`, it is also possible to evaluate the total blade cost through the detailed blade cost model from SANDIA as discussed in Chapter 2. It must be noticed, however, that the latter only provides the cost of the blade, so that it must be used in combination with one of the other two options for a complete assessment of the COE.

One of the advantages of the nested and modular architecture of `Cp-Max`, is that it offers several modes of operations:

1. **Automatic macro design:** in this mode, the MDL is operated automatically, so that one or more macro design variables are optimized in order to minimize the COE of the wind turbine. The required submodules, or the whole sequence in a full analysis, are automatically run at each perturbation of the macro design variables until the global optimal solution $\boldsymbol{p}_{\boldsymbol{g}}^{*}$ is found. This mode is useful to conduct a complete design of a new wind turbine, or a redesign of an existing one. This is the most demanding option in terms of computational time, as many iterations of the whole MDL are required to achieve convergence. A validation of `Cp-Max` as an automated SDO algortihm has been recently performed by Bortolotti et al. [89].
2. **Parametric macro design:** the MDL is operated manually instead of automatically. One or more macro design variables are parametrically changed and the required submodules are performed for each variation of the design variables, but without the external minimization of the COE. A set of required Key Performance Indicators

(KPI) is customarily used to compare the different designs. This mode is used to study the trends and effects of a certain design parameter (for example, the rotor solidity σ_g^c) on the aero-structural design of the turbine. Chapter 6 gives an example of such mode of operation.

3. **Individual component design:** in this scenario, each submodule is used as a standalone tool for the detailed optimization of system components, e.g. the structural design. The optimization is carried out according to the specific objective function and constraints of each module, as described in the next Sections. This mode is used for detailed component design or when specific constraints limit the possibility to explore the whole aero-structural feasibility domain. A classic example, typical of industrial projects, is the structural redesign of a rotor for a given turbine layout (radius, height) and for a given aerodynamic shape. Applications which broadly adopt this method are presented later in Chapters 4 and 5.

According to the needs and specific applications, the designer can access the most suitable mode, or exploit different modes in sequence to gain progressive detail over the integrated design.

Equation 3.6g shows that the MDL optimization problem can be bounded by suitable nonlinear constraints. Ideally, the global optimization loop should enjoy the highest possible freedom in order to identify the best combinations of the design variables and truly minimize the COE. However, depending on the applications, it might happen that specific requirements apply not only at detailed design level, but also on the MDL. Apart from bounds on the individual macro design variables, `Cp-Max` allows to conduct a design with frozen loads, which basically implies that some, or all, the driving ultimate and fatigue loads on the rotor, hub, and tower, are forced to stay within chosen ranges.

3.2.2 Aerodynamic Design Submodule

The Aerodynamic Design Submodule (ADS) is based on the optimization of chord, twist and thickness of the rotor blades in order to maximize the AEP for a fixed structure of the rotor. This way, during the aerodynamic design it is possible to avoid the computation of the dynamic loads and deflections required to redesign the structure. However, this strategy is reasonable only when the blade shape is not changed significantly during the aerodynamic loop. Otherwise, if the blade planform or its thickness are broadly modified during the aerodynamic optimization, this would typically require a complete redesign of the structure which might potentially overshadow the advantages of an improved energy capture. Depending on the outcomes of the structural redesign, this could even increase the COE if the mass and cost of the subcomponents become too large. Then, it is paramount to make sure that the MDL maintains enough authority on the individual design modules to ensure that the outcomes of a single design step do not march against the global strategy of minimizing the COE. In the aerodynamic design submodule, this is ensured by applying the four shape parameters defined at MDL level, as nonlinear constraints of the aerodynamic optimization problem. This concept is summarized in Fig. 3.4, which sketches the architecture of the module. In the definition of the constraints, it is possible to see that some requirements are directly defined at submodule level, while the four shape parameters that control the chord and thickness distributions are inherited from the Macro Design Loop. As a consequence, the aerodynamic submodule conducts a constrained maximization of the AEP for given target values of those parameters. This automatically assures that

the variations are not too sharp during the design while, at the same time, creates a bridge between the macro and the aerodynamic modules.

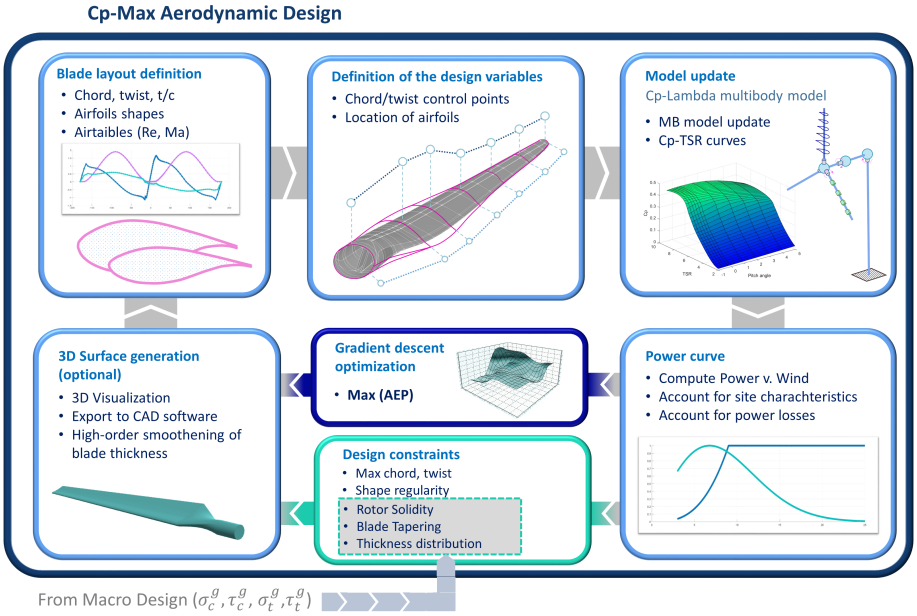

Figure 3.4: *Architecture of the Aerodynamic Design Submodule.*

Following the algorithmic notation introduced earlier, the architecture of this module can be formalized as follows:

$$(\boldsymbol{p_a^*}, AEP^*) = \texttt{MaxAEP}(\boldsymbol{p_a}, \boldsymbol{p_b}, \boldsymbol{p_s}, \boldsymbol{p_g}, \boldsymbol{D}) \tag{3.7a}$$

$$\boldsymbol{p_a} = [\boldsymbol{p_{a_c}}\ \boldsymbol{p_{a_\theta}}\ \boldsymbol{p_{a_t}}] \tag{3.7b}$$

$$AEP^* = \max_{\boldsymbol{p_a}}(\texttt{ComputeAEP}(\boldsymbol{p_a}, \boldsymbol{p_b}, \boldsymbol{p_s}, \boldsymbol{p_g}, \boldsymbol{D})) \tag{3.7c}$$

$$\boldsymbol{p_a^*} = arg(\max_{\boldsymbol{p_a}}(\texttt{ComputeAEP})) \tag{3.7d}$$

$$s.t.:$$

$$\boldsymbol{g_a}(\boldsymbol{p_a}, \boldsymbol{p_g}) \leq \boldsymbol{0} \tag{3.7e}$$

$$v_{tip} \leq v_{tip_{max}} \tag{3.7f}$$

At the end of the process, the module provides the optimal value of the energy production AEP^* and the array of the optimized aerodynamic variables $\boldsymbol{p_a^*}$.

Equation 3.7b highlights the fact that the array of the aerodynamic variables is made up of parameters associated to the chord, twist and non-dimensional thickness distributions. These are represented through dedicate parameterizations, whose control points are stored in the corresponding sub-arrays $\boldsymbol{p_{a_c}}$, $\boldsymbol{p_{a_\theta}}$ and $\boldsymbol{p_{a_t}}$. In particular, during the design chord and twist functions evolve as a direct deformation of the inital distributions by means of

suitable additive/multiplicative shape functions applied along the blade. Formally, spanwise chord and twist distributions $c(\eta)$, $\theta(\eta)$ are defined as follows:

$$c(\eta) = \overline{c}(\eta) s_c(\eta) \tag{3.8a}$$
$$\theta(\eta) = \overline{\theta}(\eta) + s_\theta(\eta) \tag{3.8b}$$

where $\eta = [0, ..., 1]$ is a non-dimensional spanwise coordinate defined along the blade axis, from the root to the tip. The functions $\overline{c}(\eta)$ and $\overline{\theta}(\eta)$ are the chord and twist distributions of the initial guess supplied at the beginning of the design loop, whereas the deforming functions $s_c(\eta)$ and $s_\theta(\eta)$ are defined as follows:

$$s_c(\eta) = \boldsymbol{n_c}(\eta)\boldsymbol{p}_{a,c} \tag{3.9a}$$
$$s_\theta(\eta) = \boldsymbol{n_\theta}(\eta)\boldsymbol{p}_{a,\theta} \tag{3.9b}$$

where $\boldsymbol{n_c}(\eta)$ and $\boldsymbol{n_\theta}(\eta)$ are cubic shape functions and $\boldsymbol{p}_{a,c}$, $\boldsymbol{p}_{a,\theta}$ are the design variables of chord and twist.
This construction allows to achieve a high authority over the chord and twist design through a relatively low number of degrees of freedom. Since the parametrization relies on deformation functions, a multiplicative approach can be used only for chord because it is ensured that this distribution always assumes non-zero values. On the other hand, this condition is not valid for the twist, so an additive deformation function gives the variability all along the blade span. The distribution of the non-dimensional thickness is treated differently, as it is reconstructed at each step from the coordinates of the pivot airfoils by means of a Cubic Hermite Spline (CHS) interpolation. The latter is defined on the unit interval $t \in [0, 1]$ as:

$$\begin{aligned}\boldsymbol{p}(t) =& (2t^3 - 3t^2 + 1)\boldsymbol{p}_0 + (t^3 - 2t^2 + t)\boldsymbol{m}_0 + \\ & (-2t^3 + 3t^2)\boldsymbol{p}_1 + (t^3 - t^2)\boldsymbol{m}_1\end{aligned} \tag{3.10}$$

where $\boldsymbol{p}_0$ is a starting point at $t = 0$ with tangent $\boldsymbol{m}_0$ and $\boldsymbol{p}_1$ is an ending point at $t = 1$ with tangent $\boldsymbol{m}_1$. The CHS interpolation can be extended to an arbitrary data set $(t_k, \boldsymbol{p}_k)$ by applying Eq. 3.10 to each interval. In the aerodynamic design module, the set of points is given by the non-dimensional coordinates of the airfoils $\boldsymbol{p}_k = \boldsymbol{p}_{\eta,af} = [\eta_{af}^j]$, $j = 1, .., n_{af}$ where n_{af} is the number of airfoils defined along the blade. Clearly, a consistent placement of the airofils requires that $\eta_{af}^1 = 0$ and $\eta_{af}^{n_{af}} = 1$. This way, although the shapes of the airfoils do not change during the design, their positioning along the blade do and this allows a control over the evolution of the non-dimensional thickness. With this formulation, the components of the aerodynamic design array 3.7b can be specified as follows:

$$\boldsymbol{p_{a_c}} = \boldsymbol{p}_{a,c} \tag{3.11a}$$
$$\boldsymbol{p_{a_\theta}} = \boldsymbol{p}_{a,\theta} \tag{3.11b}$$
$$\boldsymbol{p_{a_t}} = \boldsymbol{p}_{\eta,af} \tag{3.11c}$$

The core part of the module lies within the function `ComputeAEP`, which performs the solution of the optimization problem and produces the optimal AEP (see Eq. 3.7c) and the corresponding optimal values of the aerodynamic design variables (see Eq. 3.7d). Equation 3.7e is a set of non-linear constraints applied to the design and must be fulfilled by the optimal solution. Like the other modules of `Cp-Max`, the solution of the aerodynamic design subproblem is managed by a gradient-descent SQP method under the assumption that the merit function is sufficiently smooth with respect to the various design variables. At each iteration the gradient is computed from a forward finite difference scheme, which only requires a single evaluation of the merit function and constraints for each perturbation of the design variables. Naturally, the convergence ratio of the solution can be improved by adopting high-order finite differences, however, this would require additional evaluations of the merit function, driving up the computational time.

The evaluation of the energy production is performed iteratively by the routine `ComputeAEP` through the dedicated workflow illustrated in Fig. 3.4. At the beginning of each evaluation, the aerodynamic model is updated with the actualized values of the design variables $\mathbf{p_a}$. In the multi-body description of `Cp-Lambda`, this modifies the properties of the lifting lines associated to the rotor. Starting from the corresponding design variables, the chord and twist distributions along the blades are updated by interpolation. Similarly, the non-dimensional position of the airfoils are updated and the aerodynamic tables required by the BEM/Lifting line model are interpolated along the blade. Once the model is correctly updated, static $Cp-TSR$ curves are computed as a three-dimensional surface for varying values of the collective pitch angle and tip-speed ratio as follows:

$$\boldsymbol{\beta} = [\beta_{min}, \ \dots \ , \beta_{max}] = \beta_i, \qquad i = 1, ...n_\beta \tag{3.12a}$$

$$\boldsymbol{\lambda} = [\lambda_{min}, \ \dots \ , \lambda_{max}] = \lambda_j, \qquad j = 1, ...n_\lambda \tag{3.12b}$$

$$\boldsymbol{C_p} = \boldsymbol{C_p}(\boldsymbol{\lambda}, \boldsymbol{\beta}) = C_{p_{ij}} \tag{3.12c}$$

$$v_j = \overline{v} = v_{ref}(\mathcal{C}) \tag{3.12d}$$

$$\boldsymbol{\Omega} = [\Omega_{min}, \ \dots \ , \Omega_{max}] = \Omega_j = \frac{\lambda_j R}{v_j} \tag{3.12e}$$

According to Eqs. 3.12, a required array of pitch angles $\boldsymbol{\beta}$ is discretized into n_β values while the array of the tip-speed ratios $\boldsymbol{\lambda}$ is discretized into n_λ values. At this step, a relatively coarse grid is used, while the resulting surface is interpolated via a three-dimensional spline to recover a sufficient smoothness. Subsequently, $n_\beta * n_\lambda$ simulations are done in sequence or in parallel, depending on hardware, each one giving the power coefficient $C_{p_{ij}}$ for a given value of pitch and TSR. Since the TSR is a non-dimensional parameter, one must fix the value of either the wind v or the rotor speed Ω in order to compute the other from a known value of the TSR. In the aerodynamic design submodule, we typically fix the wind speed through Eq. 3.12d and compute the corresponding rotor speeds from the required values of the TSR according to Eq. 3.12e. Typically, $\overline{v}$ is chosen as to match the reference value of wind speed for the turbine class, which is specified by the guidelines. Alternatively, an estimation of the rated speed from previous design steps can be used as reference. This way, the conditions during the simulations are close to the real operating conditions of the turbines and deformations and aero-elastic effects can be taken into account up to a reasonable degree of fidelity. The resulting $Cp-TSR$ curves represent an aero-structural performance surface rather than a genuinely aerodynamic one, this allows in turn to derive more accurate control laws and to obtain a better estimation of the AEP.

From the envelope of the $Cp - TSR$ curves it is possible to compute the ideal regulation trajectory for the wind turbine. This can be drawn under the assumption that the control strategy is based on the tracking of the optimal power C_p^* when the turbine works in partial loading. A constant-power strategy is instead considered for the full-loading range. In a general form, this result in the definition of the following curves:

$$P(v) = P(v, \boldsymbol{C_p}(\boldsymbol{\lambda}, \boldsymbol{\beta}), v_{tip_{max}}) \tag{3.13a}$$
$$\Omega(v) = \Omega(v, \boldsymbol{C_p}(\boldsymbol{\lambda}, \boldsymbol{\beta}), v_{tip_{max}}) \tag{3.13b}$$
$$T_{el}(v) = T_{el}(v, \boldsymbol{C_p}(\boldsymbol{\lambda}, \boldsymbol{\beta}), v_{tip_{max}}) \tag{3.13c}$$
$$\beta(v) = \beta(v, \boldsymbol{C_p}(\boldsymbol{\lambda}, \boldsymbol{\beta}), v_{tip_{max}}) \tag{3.13d}$$

where P is the power output, Ω is the rotor speed T_{el} is the generator torque and β the collective pitch angle of the blades. It must be noticed that, at this level, it is possible to impose a limit on the maximum tip speed according to Eq. 3.7f, which might result in a wind range where the rotor speed is constrained and the power production is sub-optimal.

The trajectory regulation allows to draw the power curve 3.13a, which is then weighted by the site-specific parameters of the Weibull distribution, giving the AEP as follows:

$$AEP = n_{h_{yr}} \int_{v_{in}}^{v_{out}} P(v) w(v, \mathcal{C}) dv \tag{3.14}$$

where $n_{h_{yr}}$ is the number of hours in a year, v_{in} and v_{out} the cut-in and cut-out wind speeds and $w(v, \mathcal{C})$ is the Weibull distribution of the wind, which is computed from the specifications of the wind turbine class listed in $\mathcal{C}$. As mentioned, several nonlinear constraints can be applied to the design through Eq. 3.7e: as briefly discussed above, such constraints are influenced by both local aerodynamic variables and global macro variables, so that a communication channel could be established between the macro design and the aerodynamic one. The following conditions are typically enforced:

$$max(c(\eta)) \leq c_{max} \tag{3.15a}$$
$$\eta_{af}^i < \eta_{af}^j, \qquad i < j \tag{3.15b}$$
$$\eta_{af}^1 = 0 \tag{3.15c}$$
$$\eta_{af}^{n_{af}} = 1 \tag{3.15d}$$
$$\sigma_c^{aero}(c(\eta), R) = \sigma_c^g \tag{3.15e}$$
$$\tau_c^{aero}(c(\eta), \eta, R) = \tau_c^g \tag{3.15f}$$
$$\sigma_t^{aero}(t(\eta), R) = \sigma_t^g \tag{3.15g}$$
$$\tau_t^{aero}(t(\eta), \eta, R) = \tau_t^g \tag{3.15h}$$

Equation 3.15a is a simple limitation on the maximum chord, which might be enabled or not according to transportation requirements. Eqs. 3.15b, 3.15c, 3.15d impose that the first airfoil is always defined at $\eta = 0$, that the last one is always defined at $\eta = 1$ and that

the airfoils do not invert their position: the latter is a mild regulator of the shape smoothness, as it ensures that the t/c function is monotonic when the percent thickness of the pivot airfoils is non-decreasing, that is, when $t^i_{af} \geq t^j_{af}$. Relations 3.15e to 3.15h force the aerodynamic solution to fulfil the general requirements imposed by the Macro Design Loop. In particular, the rotor solidity must assume exactly the value σ^g_c controlled by the external optimizer and the same holds true for the rotor tapering τ^g_c and for the two macro parameters σ^g_t and τ^g_t computed from the non-dimensional thickness distribution.

According to the scheme in Fig. 3.3, an acoustic module for the computation of the wind turbine noise emissions is coupled to the ADS. This tool has been developed by Sucameli et al. [93] and it can be either used as an *out-of-the-loop* analysis module or employed within the aerodynamic design. However, its development is quite recent and the tool is not used in the activities presented in this work.

3.2.3 Control Synthesis Tool

One of the central features of `Cp-Max` is the possibility to include several DLC in the computation of the loads spectra. To conduct a realistic design of the turbine, such simulations should account for a significant range of scenarios, which normally include nominal operating conditions, occurrence of faults, gusts and parking conditions. Most of these simulations require that the turbine is equipped with a certain control system, so that the required performance of energy production and envelope protection can be met. For this reason, once the ADS has completed the optimization of the rotor shape, the Control Synthesis Tool (CST) generates the necessary control laws, according to the selected strategy. Schematically, the procedure can be formalized as follows:

$$(\boldsymbol{r}^*_\epsilon) = \texttt{CreateControlLaws}(\boldsymbol{p^*_a}, \boldsymbol{p_b}, \boldsymbol{p_s}, \boldsymbol{p_g}, \boldsymbol{D}) \tag{3.16a}$$

$$\boldsymbol{C_p} = \texttt{CpTSRCurves}(\boldsymbol{p^*_a}, \boldsymbol{p_b}, \boldsymbol{p_s}, \boldsymbol{p_g}, \overline{\boldsymbol{\beta}}, \overline{\boldsymbol{\lambda}}) \tag{3.16b}$$

$$\boldsymbol{r}^*_\epsilon = \texttt{ChooseControlStrategy}(\alpha_r, \boldsymbol{C_p}, \boldsymbol{D},) \tag{3.16c}$$

Within the tool, the multi-body model of the wind turbine is updated with the contents of the optimal aerodynamic solutions $\boldsymbol{p^*_a}$ and with those of the other design variables. Then, $Cp - TSR$ curves are once again computed by means of adequate static simulations, so that the matrix of the power coefficients $\boldsymbol{C_p}$ can be computed on the required grid of pitch angles $\overline{\boldsymbol{\beta}}$ and TSR $\overline{\boldsymbol{\lambda}}$. The procedure is identical to that described in Eqs. 3.12, although usually a much finer grid is built at this level, to ensure a better smoothness of the resulting surface and facilitate the following operations. Once the curves are available, the regulation stratgey $\boldsymbol{r}^*_\epsilon$ is computed according to the selected stratgey 3.16c. Here, α_r is a parameter indicating which strategy is chosen among those supported by the optimization program. In this work, three control strategies are supported, all of them based on the common assumption that the wind turbine is a variable-speed one, with pitch and torque actuators. In this light, the following strategies are selectable:

PID on collective blade pitch + LUT on torque This strategy corresponds to the choice $\alpha_r = 1$. When this option is chosen, the controller pursues different goals according to the different ranges of operation of the wind turbine. If the wind speed lies in the *partial-loading* (or *Region II*) range, it means that the wind speed is lower than the rated one, and

the controller tracks the optimal power coefficient C_p^* as computed from Eq. 3.16b. The collective blade pitch and generator torque are regulated in order to maintain the TSR of the wind turbine as close as possible to the ideal value λ^*. However, if the wind speed is in the *full-loading* (or *Region III*), the pitch and torque are monitored in order to continuously maintain the nominal power output of the turbine. Details of this strategy are given by most fundamental text books like for example Manwell et al. [32]. In this mode, the controller obtains the filtered rotor speed Ω from its own sensors and determines the required collective pitch angle β_c according to the following Proportional-Integral-Derivative (PID) regulator:

$$\beta_c = K_p(\Omega - \Omega^*) + K_i \int_{t-T_i}^{t} (\Omega - \Omega^*) d\tau + K_d \dot{\Omega} \tag{3.17}$$

$$\tag{3.18}$$

where Ω^* is a certain reference condition, typically the rated speed, and K_p, K_i, K_d are the gains of the proportional, integral and derivative terms. In the partial-loading region, this strategy usually leads the pitch to collapse to its minimum allowable value, which can be given for varying wind speeds in a tabulated form. The required generator torque is instead computed, for the sensed rotor speed, from a dedicated Look-Up-Table (LUT) which is computed by the subroutine 3.16c:

$$T_c = T_c^{LUT}(\Omega) \tag{3.19}$$

$$\tag{3.20}$$

This control strategy, which is the standard one in `Cp-Max`, has been developed internally and and allows a basic monitoring of the turbine operations. However, this controller can not handle the *Region* $II_{\frac{1}{2}}$, that is, a sub-region which is below rated but where the rotor could not be accelerated due to an active constraint on the tip speed. A complete discussion of the subject is given, among others, by Bottasso et al. [60].

PID on collective blade pitch + PID on torque This strategy, which corresponds to $\alpha_r = 2$, has been developed at DTU by Hansen and Henriksen [94] and, unlike the previous one, allows to manage velocity-constrained regions by means of a dedicated PID controller on the torque.

In partial load operation, the torque reference $Q_{ref,k}$ at a certain step k is computed as $K\overline{\Omega}_k$. The torque PID controller is always bounded by its limiting values $[Q_{min,k}, Q_{max,k}]$ so that, by tuning these limits, one can relax or constraint the distribution of the torque. In the partial loading region, this is done depending on the value of the filtered rotor speed $\overline{\Omega}_k$: when the rotor speed is well within its pre-assumed operative range $[\Omega_{min}, \Omega_r]$, then the PID must provide exactly the torque $K\overline{\Omega}_k$. This is granted by choosing $Q^k_{min} = Q^k_{max} = K\overline{\Omega}_k$. On the contrary, whenever the rotor speed approaches either Ω_r or Ω_{min}, the torque limits are relaxed so that the control action is truly managed by the PID through the rotor speed error $e_{Q,k} = \overline{\Omega}_k - \Omega_{set,k}$, where the set point is given by the rated speed or the minimum one according to which one is closer. Simultaneously, a filtered hub wind speed $\overline{V}_k$ is used to manage the minimum pitch angle, which is read from a User-supplied look-up table for varying wind speeds.

In full load operation, the torque limits are closed around a certain value, which depends on the current strategy: when the *constant power* is enabled, the target torque is given by P_r/Ω_k, where P_r is the rated power. Instead, when the *constant torque* strategy is chosen, the target torque is given by P_r/Ω_r. The reference pitch angle is the output of a PI controller, which receives a combined feedback from a speed error (which is computed from the filtered rotor speed and the rated speed) and a power error. The latter is computed as the difference between the rated power and $P_{ref,k} = Q_{ref,k}\Omega_k$. Both errors contribute to both the proportional and the integral terms of the controller.

Model-based control of pitch, torque This implementation corresponds to $\alpha_r = 3$ and is more sophisticated, since it uses a reduced model of the wind turbine to uniquely compute an optimal control strategy. The controller can be used in all speed ranges: in partial-loading it applies a variable-torque/constant-pitch strategy whereas in full-loading it applies a constant-torque/variable-pitch strategy. If present, in Region $II_{\frac{1}{2}}$ the torque and the pitch are applied to minimize the losses due to the sub-optimal tip-speed ratio. A full-state Linear Quadratic Regulator (LQR) is tuned by considering a non-linear reduced model of the turbine, which is linearized at a certain set of conditions. The nonlinear model is based on the following set of equations:

$$M_T\ddot{(d)} + C_T\dot{d} + K_T d - F_A(\Omega, \beta_e, v_w - \dot{d}, v) = 0 \tag{3.21a}$$

$$(J_{LSS} + J_{HSS})\dot{\Omega} + T_L(\Omega) - T_A(\Omega, \beta_e, v_w - \dot{d}, v) = 0 \tag{3.21b}$$

$$\ddot{\beta_e} + 2\xi\omega\dot{\beta_e} + \omega^2(\beta_e - \beta_c) = 0 \tag{3.21c}$$

$$\dot{T_{el_e}} + \frac{1}{\tau}(T_{el_e} - T_{el_c}) \tag{3.21d}$$

Equation 3.21a is the tower dynamics, d is the tower top displacement in the direction of fore-aft, M_T, C_T, K_T are equivalent mass, damping and stiffness of the tower and F_A is the aerodynamic force. Equation 3.21b represents the dynamics of the drive-train: here J_{LSS} and J_{HSS} are the inertia associated to the low-speed and the high-speed shafts, T_L is the dissipated torque due to mechanical loss and T_A the aerodynamic torque. The dynamics of the pitch and torque actuators are represented by Eqs. 3.21c and 3.21d: here β_e and T_{el_e} are the collective pitch angle and the electrical torque supplied to the turbine, while β_c and T_{el_c} are the corresponding inputs defined by the controller. v_w is the instantaneous wind speed and v the mean wind speed at the hub. The rotor force and moment coefficients are computed from the known envelope of the $C_p - TSR$ and $C_f - TSR$ curves computed by subroutine 3.16b:

$$T_A = \frac{1}{2}\rho\pi R^3 \frac{C_p(\lambda, \beta_e, v)}{\lambda}(v_w - \dot{d})^2 \tag{3.22a}$$

$$F_A = \frac{1}{2}\rho\pi R^2 C_f(\lambda, \beta_e, v)(v_w - \dot{d})^2 \tag{3.22b}$$

$$\tag{3.22c}$$

as discussed earlier, the dependence of C_f, C_p on the mean wind speed v means that the deformability of the flexible elements can be taken into account when computing the curves by choosing v such as it is a good approximation of the real operating conditions of the

turbine. The states of the LQR are collected into the array $\boldsymbol{x} = [d, \dot{d}, \Omega, \beta_e, \dot{\beta}_e, T_{el_e}]$ while the controls are collected in $\boldsymbol{u} = [\beta_c, T_{el_c}]$ so that the reduced model can be represented as $\dot{\boldsymbol{x}} = f(\boldsymbol{x}, \boldsymbol{u}, v_m)$. During the generation of the control laws, Eqs. 3.21 are numerically linearized around steady trimmed conditions, in order to compute the reference points of the LQR at different wind speeds. Then, for each set point, the optimal LQR is computed by minimizing the functional

$$J = \frac{1}{2}\int_0^\infty (\boldsymbol{\Delta x}^{\boldsymbol{T}} \boldsymbol{Q} \boldsymbol{\Delta x} + \boldsymbol{\Delta u}^{\boldsymbol{T}} \boldsymbol{R} \boldsymbol{\Delta u}) \tag{3.23a}$$

$s.t.:$

$$\boldsymbol{\Delta \dot{x}} = \boldsymbol{A}\boldsymbol{\Delta x} + \boldsymbol{B}\boldsymbol{\Delta u} \tag{3.23b}$$

where the dynamic equations of the reduced model 3.23b enter as contraints of the problem: those are enforced by means of Lagrange multipliers, which are then determined as part of the optimal solution. The problem 3.23 can be solved over an infinite time-span by means of the Riccati equation, so that a control law in the form:

$$\boldsymbol{\Delta u}(v_m) = \boldsymbol{K_{LQR}}(v_m)\boldsymbol{\Delta x}(v_m) \tag{3.24}$$

can be readily established for each of the set points v_m. Clearly, the full-state feedback formulation of the MIMO-LQR controller implies that all the states can be directly measured or reconstructed through a dedicated observer. It must be noticed that, for additional rotor speed tracking, it is possible to compute the LQR gains on the augmented state $\boldsymbol{x} = [d, \dot{d}, \Omega, \beta_e, \dot{\beta}_e, T_{el_e}, \int \Omega dt]$, in which the integral weighting of the rotor speed globally ensures better performance.

3.2.4 Prebend Design Submodule

The goal of the Prebend Design Submodule (PDS) is to optimize the prebend, i.e. the native out-of-plane deflection of the blade in order to minimize the deformed rotor area under normal loadings A_δ. In fact, while a certain amount of prebend can relax an active tip deflection constraint, especially in glass-fiber rotors, we must consider that large deformations typically reduce the energy production of the turbine. Then, by minimizing the deformed area we make sure that the structural advantages do not come at the expenses of the energy output. Formally, this could be written as:

$$\min_{\boldsymbol{p}_b}(A_\delta(\boldsymbol{p}_a, \boldsymbol{p}_b, \boldsymbol{p}_s, \boldsymbol{p}_g, \boldsymbol{r}_\epsilon)) \tag{3.25a}$$

$$A_\delta = \int_0^1 f(\eta, \delta_y(\boldsymbol{p}_a, \boldsymbol{p}_b, \boldsymbol{p}_s, \boldsymbol{p}_g), \boldsymbol{r}_\epsilon)^2 d\eta \tag{3.25b}$$

where $f(\eta, \delta_y)$ is the local distance between the rotor plane and the *deformed* blade. Quite intuitively, f depends on the spanwise location η but also depends on the out-of-plane deflections of the blade δ_y. In turn, the latter depend on the aero-structural design of the blade, on the distribution of prebend and on the regulation trajectory of the wind turbine, whose parameters are collected in the structure $\boldsymbol{r}_\epsilon$ A qualitative scheme of this concept is given in

Fig. 3.5, in which the spanwise distance $f(\eta)$ that should be minimized is represented by the shaded grey area. Like any design submodule within `Cp-Max` architecture, the PDS can be operated as a standalone tool. However, if the aerodynamic parameters come from an ADS optimization as described in § 3.2.2, then $\boldsymbol{p}_a$ becomes $\boldsymbol{p}_a^*$ inside Eqs. 3.25. Similarly, if the regulation trajectory has been computed from a CST synthesis procedure as described in § 3.2.3, $\boldsymbol{r}_\epsilon$ becomes $\boldsymbol{r}_\epsilon^*$. In this case, which is the normal procedure when the PDS is operated within the Macro Design Loop, the optimization problem becomes:

$$\min_{\boldsymbol{p}_b}(A_\delta(\boldsymbol{p}_a^*, \boldsymbol{p}_b, \boldsymbol{p}_s, \boldsymbol{p}_g, \boldsymbol{r}_\epsilon^*)) \tag{3.26a}$$

$$A_\delta = \int_0^1 f(\eta, \delta_y(\boldsymbol{p}_a^*, \boldsymbol{p}_b, \boldsymbol{p}_s, \boldsymbol{p}_g), \boldsymbol{r}_\epsilon^*)^2 d\eta \tag{3.26b}$$

where $\boldsymbol{p}_b$ is an array containing the design variables of the prebend. A simplified sketch of the PDS workflow is given in Fig. 3.6. It must be noted that, unlike the ADS, all the constraints are defined at local level, which means that the Macro Design Loop has no direct feedback on the outcomes of the PDS optimization. A fundamental consequence is that the optimal prebend shape is not directly controlled by the macro design. Obviously, within the module the action of the macro design is sensed through the values of the arrays $\boldsymbol{p}_a^*, \boldsymbol{p}_s, \boldsymbol{p}_g$ and through the control laws $\boldsymbol{r}_\epsilon^*$: all these structures change during the global design in accordance to the optimization process. There is not, however, a variable which connects directly the PDS with the macro design variables. This can create problems in the conditioning of the Macro Design Loop, as the prebend shape can potentially evolve independently from the global optimization, and even undermine the overall COE minimization. We discussed aplenty about this potential shortcoming, and we came up with the idea to introduce a new macro variable which regulates the prebend at tip. In that case, the PDS would optimize the prebend for a certain value at tip, exactly like the ADS optimizes the chord for a certain value of the solidity. Eventually, however, we concluded that introducing an additional variable at macro design level would have a great impact on the computational time. As a workaround, we introduced a limit on the total prebend at tip which is manually defined through a nonlinear constraint instead of linking it to the Macro Design. This conclusion is also based on the fact that usually the maximum prebend is set by manufacturing requirements rather than by a proper optimization procedure, so that introducing a manual limit on the evolution of the prebend would not drive the optimization towards unrealistic solutions.
The structure of the PDS can be formalized in the algorithmic form as follows:

$$(\boldsymbol{p_b^*}, A_\delta^*) = \texttt{OptimizePrebend}(\boldsymbol{p_a^*}, \boldsymbol{p_b}, \boldsymbol{p_s}, \boldsymbol{p_g}, \boldsymbol{D}, \boldsymbol{r}_\epsilon^*) \tag{3.27a}$$

$$\boldsymbol{p_b} = \texttt{FindCP}(\boldsymbol{p_b}, \boldsymbol{D}) \tag{3.27b}$$

$$A_\delta^* = \min_{\boldsymbol{p}_b}(\texttt{MaxArea}(\boldsymbol{p_a^*}, \boldsymbol{p_b}, \boldsymbol{p_s}, \boldsymbol{p_g}, \boldsymbol{D}, \boldsymbol{r}_\epsilon^*)) \tag{3.27c}$$

$$(\boldsymbol{\delta_y}) = \texttt{ComputeDeformed}(\boldsymbol{p_a^*}, \boldsymbol{p_b}, \boldsymbol{p_s}, \boldsymbol{p_g}, \boldsymbol{D}, \boldsymbol{r}_\epsilon^*) \tag{3.27d}$$

$$(A_\delta) = \texttt{ComputeArea}(\boldsymbol{\delta_y}, \boldsymbol{p_g}) \tag{3.27e}$$

$$\boldsymbol{p_b^*} = arg(\min_{\boldsymbol{p}_b}(\texttt{MaxArea})) \tag{3.27f}$$

$$s.t.:$$

$$\boldsymbol{g_b}(\boldsymbol{p_b}) \leq \boldsymbol{0} \tag{3.27g}$$

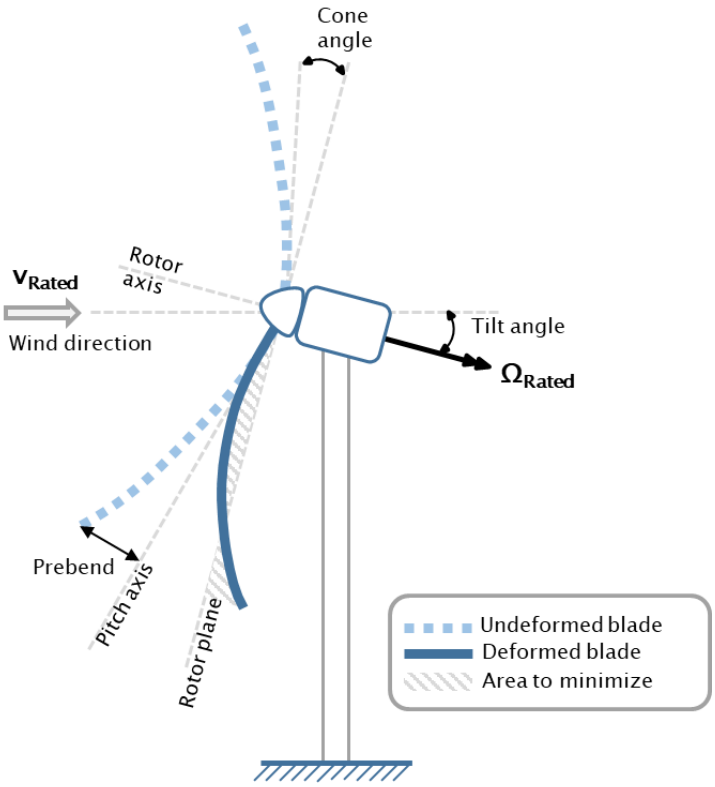

Figure 3.5: *Qualitative scheme of the prebend design.*

Equation 3.27a is the main I/O gate of the module: as discussed, the tool takes as inputs the optimal aerodynamic design $\boldsymbol{p}_{\boldsymbol{a}}^{*}$, the variables from the MDL $\boldsymbol{p}_{\boldsymbol{g}}$ and those related to the structure $\boldsymbol{p}_{\boldsymbol{s}}$. As discussed, the module also requires the knowledge of the regulation laws of the turbine, supplied through the parameter $\boldsymbol{r}_{\epsilon}^{*}$. The previous shape of the prebend, or the initial if the module is run for the first time, is collected in the array $\boldsymbol{p}_{\boldsymbol{b}}$ and is also sent to the module as part of the input.
The core of the tool lies in the function `MaxArea`, whose basic workflow is illustrated in Fig. 3.6. Unlike the variables of the ADS, which are directly defined on the initial shape through additive or multiplicative functions, the shape of the prebend is parametrized by means of the Bézier polynomials introduced in the *free-form* algorithm (See § 2.3.1). Then, the spanwise distribution of prebend $\zeta = \zeta(\eta)$ can be parametrized as follows:

$$\zeta(\eta) = \sum_{i=0}^{n_\zeta} \binom{n_\zeta}{i} (1-t)^{n_\zeta - i} t^i \mathbf{p}_{\zeta_i} \tag{3.28}$$

(3.29)

where n_ζ is the order of the Bézier curve and $\mathbf{p}_{\zeta_i}, i = 1, ..., n_\zeta + 1$ are the corresponding control points. Then, the array of the design variables of the PDS contains the control points of the Bèzier curve as follows:

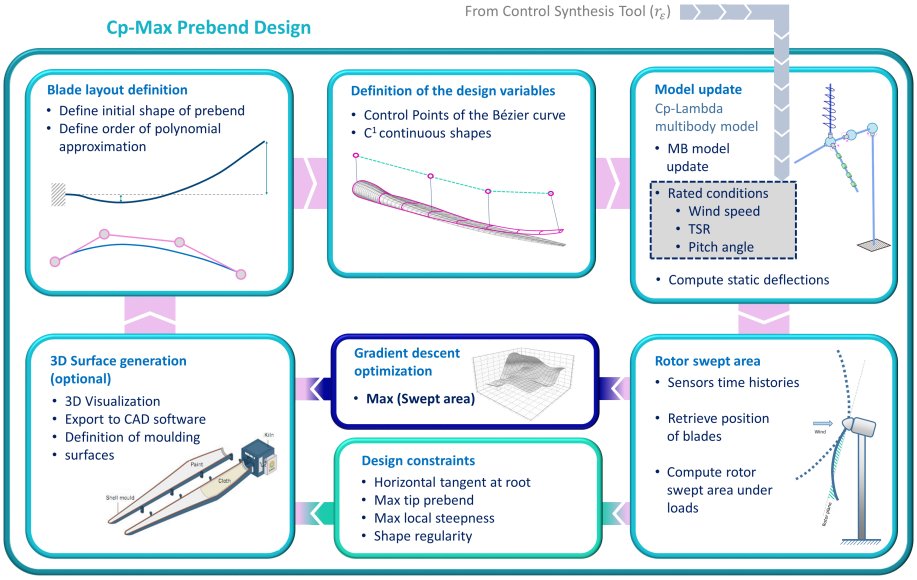

Figure 3.6: *Architecture of the Prebend Design Submodule.*

$$\boldsymbol{p}_b = \mathbf{p}_{\zeta_i}, \qquad i = 1, ..., n_\zeta + 1 \tag{3.30}$$

Bézier curves of any order can be employed to describe the prebend, although a degree between 4 and 6 is typically sufficient to achieve enough flexibility without falling into overfitting problems. When the module is initialized, the subroutine 3.27b identifies the initial guess of the PDS by finding the Bézier curve of degree n_ζ which best approximates the last available distribution of prebend. This is done by solving the following unconstrained minimization problem:

$$\min_{\mathbf{p}_{\zeta_i}} (e(\zeta, \mathbf{p}_{\zeta_i})), \qquad i = 1, ..., n_\zeta + 1 \tag{3.31a}$$

$$e(\zeta, \mathbf{p}_{\zeta_i}) = \int_0^1 (\bar{\zeta}(\eta) - \zeta(\eta, \mathbf{p}_{\zeta_i}))^2 d\eta \tag{3.31b}$$

where $\bar{\zeta}(\eta)$ is the last known distribution of prebend and $\zeta(\eta, \mathbf{p}_{\zeta_i})$ a Bézier curve originated by the control points $\mathbf{p}_{\zeta_i}$. It must be noticed that in `Cp-Max` an arbitrary shape of prebend can be given as part of the initial guess. Then, at the first iteration of the Macro Design Loop, the solution of problem 3.31 identifies the curve which best represents the initial shape and, depending on the chosen degree, it might happen that the Bézier representation does not exactly match the given distribution. In this case, the residual $e(\zeta, \mathbf{p}_{\zeta_i})$ at the end of the problem is different from zero. At subsequent iterations, on the contrary, since the distribution $\bar{\zeta}(\eta)$ has already been designed by the PDS, the solution of 3.31 allows to exactly recover the values of the control points, giving a residual equal to zero.

According to the workflow of Fig. 3.6, once the Bézier curve has been initialized or modified during optimization, the multi-body model is modified by updating the lifting lines

and the geometric description of the blades. Then, subroutine 3.27d conducts a static `Cp-Lambda` simulation at the operating conditions identified by the control parameters $\boldsymbol{r}_\epsilon$. The resulting out-of-plane deflections $\delta_y(\eta)$ along the blades are registered by a spanwise distribution of sensors and supplied to subroutine 3.27e, which computes the shaded area A_δ according to Eqs. 3.25. Then, the control points of the prebend are updated, a new Bézier description is generated and the process is repeated until convergence.

Like other submodules, the PDS ensures that the optimal prebend fulfils a set of nonlinear constraints, which are listed below:

$$max(\zeta(\eta)) \leq \zeta_{max} \tag{3.32a}$$
$$min(\zeta(\eta)) \geq \zeta_{min} \tag{3.32b}$$
$$\frac{\partial \zeta(\eta)}{\partial \eta} \leq \epsilon_\zeta \tag{3.32c}$$
$$\left.\frac{\partial \zeta(\eta)}{\partial \eta}\right|_{\eta \leq \overline{\eta}} = 0 \tag{3.32d}$$

constraints 3.32a and 3.32b simply pose limits on the maximum and minimum values of prebend: while the former is usually achieved at blade tip, the prebend can become negative in certain parts of the blade, and thus a minimum value controls how negative the prebend shape can be. Relation 3.32c forces the steepness of the shape to be lower than a certain threshold ϵ_ζ, typically defined by the manufacturer. Eventually, constraint 3.32d forces the prebend to have a horizontal tangent from the root of the blade up to the coordinate $\overline{\eta}$.

3.2.5 Structural Design Submodule

The Structural Design Submodule (SDS) is the original core of `Cp-Max`, and is discussed by Bottasso et al. [13]. It allows to conduct a fully feasible structural optimization of blades and tower with the aim of minimizing the capital costs associated to the turbine manufacturing (ICC). The computation of this figure basically depends on the choice of the cost model. The essential feature of the tool is that the loads employed for sizing the structural components are extracted from an arbitrarily-large set of DLC so that, if sufficient conditions are considered, the optimal solution automatically complies with international guidelines [62, 61]. Clearly, the amount of load cases can be customized according to the specific needs of the design, in particular because the run of the dynamic simulations is computationally expensive and could easily become a bottleneck along the optimization process. According to the multi-level architecture of `Cp-Max`, the goal of the SDS is to optimize the set of structural design variables $\boldsymbol{p}_s$, which contains the thickness of the structural components defined along the sectional arrangement. In this context, the structure is optimized for a given aerodynamic shape and for a given prebend, so that the computation of the loads can take into account the previous optimization steps conducted by the ADS

and by the PDS. The algorithmic description of the module is the following:

$$(\boldsymbol{p}_s^*, ICC^*) = \texttt{MinICC}(\boldsymbol{p}_{\boldsymbol{a}}^*, \boldsymbol{p}_{\boldsymbol{b}}^*, \boldsymbol{p}_{\boldsymbol{s}}, \boldsymbol{p}_{\boldsymbol{g}}, \boldsymbol{D}, \boldsymbol{r}_\epsilon^*) \tag{3.33a}$$

$$\boldsymbol{p}_s = [\boldsymbol{t}_b^{Fabrics}\ \boldsymbol{t}_b^{Core}\ \boldsymbol{t}_t,\ \boldsymbol{\rho}_t] \tag{3.33b}$$

$$(\boldsymbol{F}_U, \boldsymbol{F}_{DEL}, \boldsymbol{\delta}_U) = \texttt{UpdateLoads}(\boldsymbol{p}_{\boldsymbol{a}}^*, \boldsymbol{p}_{\boldsymbol{b}}^*, \boldsymbol{p}_{\boldsymbol{s}}, \boldsymbol{p}_{\boldsymbol{g}}, \boldsymbol{D}, \boldsymbol{r}_\epsilon^*) \tag{3.33c}$$

$$ICC^* = \min_{\mathbf{p}_s}(\texttt{ComputeICC}(\boldsymbol{p}_{\boldsymbol{a}}^*, \boldsymbol{p}_{\boldsymbol{b}}^*, \boldsymbol{p}_{\boldsymbol{s}}, \boldsymbol{p}_{\boldsymbol{g}}, \boldsymbol{D}, \boldsymbol{F}_U, \boldsymbol{F}_{DEL}, \boldsymbol{\delta}_U)) \tag{3.33d}$$

$$\boldsymbol{p}_s^* = arg(\min_{\mathbf{p}_s}(\texttt{ComputeICC})) \tag{3.33e}$$

$$s.t.:$$

$$\boldsymbol{g}_{\boldsymbol{s}}(\boldsymbol{p}_{\boldsymbol{b}}^*, \boldsymbol{p}_{\boldsymbol{s}}, \boldsymbol{p}_{\boldsymbol{g}}, \boldsymbol{D}, \boldsymbol{r}_\epsilon^*, \boldsymbol{F}_U, \boldsymbol{F}_{DEL}, \boldsymbol{\delta}_U) \leq \mathbf{0} \tag{3.33f}$$

Equation 3.33a takes as input all the design variables from the MDL and from the ADS and PDS, as well as the array of known information $\boldsymbol{D}$. The control laws $\boldsymbol{r}_\epsilon^*$ are also supplied to the module, as they define the control strategy adopted by the turbine during the dynamic simulations.

Equation. 3.33b shows that the array of the structure-related design variables, here indicated with $\boldsymbol{p}_s$, includes the thickness of the blade structural components, including both stress-bearing composite fabrics $\boldsymbol{t}_s^{Fabrics}$ and the various fillers $\boldsymbol{t}_s^{Core}$ employed in sandwich layups. It also includes the diameter and thickness of the tower segments, collected respectively into $\boldsymbol{\rho}_t$ and $\boldsymbol{t}_t$ arrays. The structural variables are not parametrized, on the contrary, the value of the spanwise thickness of a certain component is directly discretized at the required optimization stations. When the design variables are changed along the optimization, the distribution is recovered through interpolation.

The core of the module is the combination of subroutines 3.33c and 3.33d, which are both repeated iteratively until convergence. A qualitative scheme of the workflow of the SDS is given in Fig. 3.7.
At the beginning of the loop, the structural definition of the model is initialized with the starting values $\boldsymbol{p}_s^0$ or, during optimization, updated with the actualized variables $\boldsymbol{p}_s$. It is important to notice that only the thickness of the structural components are optimized, whereas the sectional topology of blade and tower (i.e. number of webs, location of the spar caps) are not. Recently, Bortolotti et al. [95] discussed an approach to include the mechanical properties of laminates within the optimization loop of the SDS, however, that capability is still being investigated and has not been exploited in this work. As a consequence, here we always assume that the mechanical properties of materials, as well as the features of the lamination (like fiber orientation, number of plies, etc..) are provided in the array $\boldsymbol{q}_s$ as part of the input data (see Eq. 3.3). Once the variables have been updated, the structural definition of the blades and the tower are modified accordingly. As discussed, the flexibility model embedded in `Cp-Lambda` requires the knowledge of the structural properties along the beam axis. Sectional characteristics of the blades are computed numerically through finite elements cross-sectional analysis, which is specifically performed by the module ANBA developed originally by Giavotto et al [65]. At each section, the tool requires the sectional topology, the lamination sequence of each structural element and the thickness of each component, then it computes fully-populated mass and stiffness matrix, as well as the characteristic centers of the section. The full stress and strain systems can

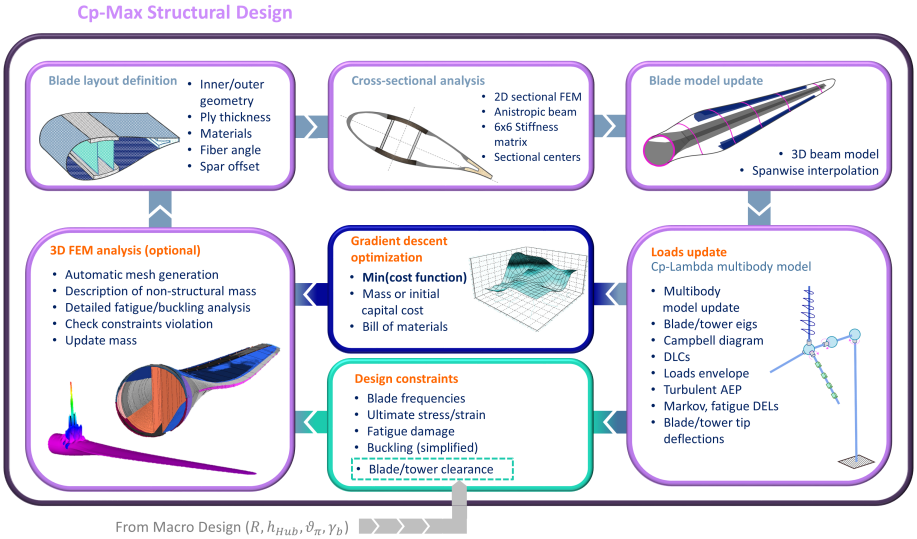

Figure 3.7: *Architecture of the Structural Design Submodule.*

also be computed, whenever a loading condition is supplied to the program. Since the tower is assumed to be piece-wise cylindrical, the corresponding sectional properties and stress distributions are directly computed by analytical relations.

When the multi-body model is correctly updated, subroutine 3.33c runs the required set of simulations (DLC) with the chosen control strategy $\boldsymbol{r}_{\epsilon}^{*}$ and computes the envelope of the ultimate loads $\boldsymbol{F}_U$ and displacements $\boldsymbol{\delta}_U$, as well as equivalent fatigue loads $\boldsymbol{F}_{DEL}$. The latter are extracted from a dedicated subset of DLC, in particular Normal Turbulence Model (NTM) simulations, by applying a Rainflow-counting algorithm as described by Sutherland [96]. Fundamental system frequencies, including blade and tower modes, are also computed at this step. To capture a better estimation of the power production in operating condition, a refined value of the AEP is also computed from Weibull-averaged NTM simulations. This way, it is possible to correct the estimation of the energy yielding which comes from the ADS (see § 3.2.2) by including the effects of the system deformations and the effects of the required category of turbulence. The resulting value is then supplied to the cost model at the end of the structural optimization. Once the computation of the sizing loads and displacements is over, the proper structural optimization begins. The loading systems $\boldsymbol{F}_U, \boldsymbol{F}_{DEL}$ are frozen and directly supplied to the operating part of the SDS: ultimate loads are then directly used to evaluate the stress in the structure and to verify the corresponding constraints, whereas fatigue DEL are applied to evaluate the compliance of the structure with the required fatigue life. However, the ultimate displacements require some subtlety: since the sizing displacement can occur during an arbitrary DLC, there would be the necessity to repeat that DLC at every evaluation of the optimization process. Since the number of the structural variables is usually high, this would require to repeatedly perform the sizing DLC, with a dramatic increase of the computational time. Then, in `Cp-Max`, an equivalent loading system is computed so that the blade displacements given by the equivalent system fairly approximates the actual ultimate displacements. This can be formalized

by the following optimization scheme:

$$\min_{\tilde{\boldsymbol{F}}_\delta}(e_\delta) \tag{3.34a}$$

$$e_\delta = \int_0^1 (\delta_U(\eta) - \delta(\tilde{F}_\delta(\eta)))^2 d\eta \tag{3.34b}$$

The solution of problem 3.34 allows to compute the required set of equivalent loads $\tilde{\boldsymbol{F}}_\delta$, which are then frozen during the optimization. With this formalization, during the single evaluation of the SDS, it is possible to compute the ultimate displacements of the blade by applying the set of static equivalent loads to a cantilevered beam, instead of re-running a costly DLC every time. The procedure is presented by Hong et al. [97]. Once the loading set $\boldsymbol{F}_U, \boldsymbol{F}_{DEL}, \tilde{\boldsymbol{F}}_\delta$ has been established, the actual structural optimization begins and the structural variables are sized for the minimum ICC. This is achieved by a sequence of two design steps: a *coarse*, or *aeroelastic* level, in which the structural integrity verifications are performed by the combination of 1D beam model and the 2D cross-sectional analysis of `ANBA`. In most preliminary applications, the coarse-level design is sufficient to ensure the fulfilment of basic integrity constraints. However, when a deeper level of detail is needed, typically for industry and manufacturing applications, the coarse solution can be refined by a *fine* level of design, based on a complete 3D FEM model of the blade and, possibly, of the tower as described by Bottasso et al. [38]. At this step, a complete 3D mesh of the blade structural arrangement is automatically generated, and relevant verifications are repeated, for the same loading set $\boldsymbol{F}_U, \boldsymbol{F}_{DEL}, \tilde{\boldsymbol{F}}_\delta$, to identify possible shortcomings of the coarse-level solution. Typically, the fine-level allows a better description of localized stress at the conjunction of different sectional elements (e.g. the connection between the spar caps and the webs). Additionally, a complete characterization of the first buckling modes is possible, which typically results in a better sizing of the sandwich panels.

Once that both the coarse- and fine-level are completed, the structural optimization is concluded. However, it might happen that the optimal structure is quite different from the initial, that is, $\|\boldsymbol{p}_s^{Opt} - \boldsymbol{p}_s^0\| > \epsilon_s$, where ϵ_s is the desired tolerance. In this case, the assumption of frozen loads could not be satisfied, resulting in a structure which produces loads which differ significantly from the set $\boldsymbol{F}_U, \boldsymbol{F}_{DEL}, \tilde{\boldsymbol{F}}_\delta$ assumed for optimization. In this case, the whole procedure of load computation and coarse/fine level design summarized by Eqs. 3.33c and 3.33d is repeated until convergence. Intuitively, the procedure can be costly in terms of computational time, since a great deal of DLC is computed multiple times within a single run of the SDS. Then, a great care is always recommended in order to tune the set of the DLC under consideration and the tolerance of the structural module. There is a twofold advantage, however: firstly, the procedure ensures that the optimal structural design is fully compliant with the strict constraints required by certification bodies. Secondly, the re-computation of the loads allows the design to be fully correlated with the loading system, so that the impact of the ongoing design on the loads and displacements of the turbine is directly taken into account. Then, the optimal solution is coherent with its own loading system. Since the verification of the structural safety is a paramount step of a feasible design, a variety of constraints are imposed on both levels of design, as

summarized by Eq. 3.33f. The following constraints are applied to the SDS module:

$$\boldsymbol{g}_s^{man}(\boldsymbol{p}_s, \boldsymbol{D}) \leq \boldsymbol{0} \tag{3.35a}$$
$$\boldsymbol{\omega}_b(\boldsymbol{p}_s, \boldsymbol{p}_b^*, \boldsymbol{D},) \in [\boldsymbol{\omega}_b^L(\boldsymbol{p}_s, \boldsymbol{r}_\epsilon^*), \boldsymbol{\omega}_b^U(\boldsymbol{p}_s, \boldsymbol{r}_\epsilon^*)] \tag{3.35b}$$
$$\boldsymbol{\omega}_t(\boldsymbol{p}_s, \boldsymbol{D},) \in [\boldsymbol{\omega}_t^L(\boldsymbol{p}_s, \boldsymbol{r}_\epsilon^*), \boldsymbol{\omega}_t^U(\boldsymbol{p}_s, \boldsymbol{r}_\epsilon^*)] \tag{3.35c}$$
$$\boldsymbol{\delta}_y(\boldsymbol{p}_s, \tilde{\boldsymbol{F}}_\delta)\Big|_{\eta=1} \leq \delta_{tip_{max}}(\boldsymbol{p}_b^*, \boldsymbol{p}_s, \boldsymbol{p}_g, \boldsymbol{D}) \tag{3.35d}$$
$$\boldsymbol{\sigma}_{b,t}(\boldsymbol{p}_s, \boldsymbol{D}, \boldsymbol{F}_U) \leq \boldsymbol{\sigma}_{b,t}^{adm}(\boldsymbol{f}_{mat,b},\ \boldsymbol{f}_{mat,t}) \tag{3.35e}$$
$$\boldsymbol{\epsilon}_{b,t}(\boldsymbol{p}_s, \boldsymbol{D}, \boldsymbol{F}_U) \leq \boldsymbol{\epsilon}_{b,t}^{adm}(\boldsymbol{f}_{mat,b},\ \boldsymbol{f}_{mat,t}) \tag{3.35f}$$
$$\boldsymbol{d}_b(\boldsymbol{p}_s, \boldsymbol{D}, \boldsymbol{F}_{DEL}) \leq \boldsymbol{1} \tag{3.35g}$$
$$\boldsymbol{d}_t(\boldsymbol{p}_s, \boldsymbol{D}, \boldsymbol{F}_{DEL}) \leq \boldsymbol{1} \tag{3.35h}$$
$$\boldsymbol{\lambda}_b(\boldsymbol{p}_s, \boldsymbol{D}, \boldsymbol{F}_U) \geq \boldsymbol{1} \tag{3.35i}$$
$$\tag{3.35j}$$

Equation 3.35a includes a list of requirements specific to the manufacturing which must be embedded in the design. These may account for maximum lamination thickness of the structural components, or starting and ending locations of the elements for both blades and tower.

Equations 3.35b and 3.35c encompass all the resonance-avoidance criteria which result in the suitable placement of blade and tower natural frequencies. Here, $\boldsymbol{\omega}_b$ and $\boldsymbol{\omega}_t$ collect the eigenfrequencies of the blade and, respectively, the tower. Each frequency must lie within a certain range specified by the boundaries $\boldsymbol{\omega}_b^L$, $\boldsymbol{\omega}_b^U$, for the blade, and by $\boldsymbol{\omega}_t^L$, $\boldsymbol{\omega}_t^U$ for the tower. In particular, the first flapwise and edgewise frequencies of the blade should be adequately separated from the N_b per revolution, where N_b is the number of blades. Additionally, they must be adequately separated from each other. Similar considerations hold for the tower first fore-aft and side-side modes. It is important to notice that the range of the admissible values for each frequency depends on the structural design $\boldsymbol{p}_s$, but also on the regulation strategy $\boldsymbol{r}_\epsilon^*$, specifically because the definition of the *per revolution* frequencies depends on the nominal rotor speed Ω_R.

Equation 3.35d states that the blade tip deflection in the out-of-plane direction must not exceed a limiting value $\delta_{tip_{max}}$. This value is continually updated through the design because its value depends on the blade/tower clearance and, ultimately, the value of the clearance depends on several fixed parameters as well as on design variables coming from different submodules:

$$\delta_{tip_{max}} = \alpha(\boldsymbol{I_{DLC}})\Delta_{bt} \tag{3.36a}$$
$$\Delta_{bt} = \delta_{Hub} + Rsin(\theta_\pi + \gamma_b) + \zeta_{tip} - \frac{1}{2}d_t(y_t = y_{b,tip}) \tag{3.36b}$$
$$y_{b,tip} = h_{Hub} - Rcos(\theta_\pi + \gamma_b) \tag{3.36c}$$

The maximum allowable tip deflection is computed from Eq. 3.36a, where a simulation-dependent safety factor α is applied to the blade/tower clearance Δ_{bt}. The latter is estimated, under the assumptions that the tilt and cone angle are small, from geometric relations along the turbine: δ_{Hub} is the rotor overhang, R the rotor radius, θ_π and γ_b are respectively the tilt and cone angles optimized by the MDL. ζ_{tip} is the prebend at tip, which might be given or optimized through the PDS, while $d_t(y_t)$ is the distribution of the tower radius along the tower axis y_t. This function should be evaluated at a suitable height $y_{b,tip}$ in order to account for the fact that the tower has a certain radius, which must be subtracted from the available clearance. In most applications, the coarse-level design is sufficient to fulfil this constraint with a high level of confidence, and a further verification with the fine-level is typically made only to double-check the results.

Equations 3.35e, 3.35f ensure that the stress and strain in the blade and tower structures are always within their maximum admittable values. The latter are obtained from the properties of the materials as specified by international standards, and account for relevant safety factors. These constraints are checked at both coarse-level and fine-level design steps, in particular because local stress concentrations due to the three-dimensional blade shape could be missed during the coarse-level optimization.

Equations 3.35g, 3.35h ensure the integrity of structures under fatigue loads. During the load computation phase, a rainflow counting analysis is performed on the required subset of DLC which must, at the very least, include fully-turbulent DLC 1.2. Then, a complete fatigue analysis is performed at sectional level along the whole blade, in order to provide a preliminary assessment of the integrity of the structural components. A full fatigue analysis is a costly one and can not be performed during the subsequent optimization. To ease the computational time, during optimization a partial fatigue analysis is done only on those points identified as the most critic. On each verification point, it is possible to compute the fatigue damage associated to a single stress component:

$$d_{\sigma_r} = \sum_{i,j,k} F_{v_k} \frac{n(\sigma_{m_i}, \sigma_{a_j}, v_k)}{N(\sigma_{m_i}, \sigma_{a_j}, \sigma_{adm}, \gamma)} \tag{3.37}$$

where F_{v_k} represents the ratio between the time spent by the turbine at wind speed v_k (along its operational time) and the duration of the simulation. n is the number of cycles at mean stress σ_{m_i}, amplitude σ_{a_j} and wind speed v_k. The corresponding admittable number of cycles is N, which is suitably corrected through a safety factor γ. Once the fatigue damage 3.37 is computed for each component of stress, a multi-axial damage index can be defined according to Philippidis and Vassilopoulos [98]:

$$d_b = d_{\sigma_1}^{2/m} + d_{\sigma_2}^{2/m} - (d_{\sigma_1} d_{\sigma_1})^{1/m} + d_{\sigma_6}^{2/m} \tag{3.38}$$

where m is the inverse slope of the Wöhler curve, and the indices 1,2,6 identify respectively the longitudinal, transverse and shear components of stress. For the verification of tower, the index d_t must be computed according to the relevant standards [99]:

$$d_t = \left(\frac{\gamma_{F_f} \Delta\sigma_{E,2}}{\Delta\sigma_c / \gamma_{M_f}}\right)^3 + \left(\frac{\gamma_{F_f} \Delta\tau_{E,2}}{\Delta\tau_c / \gamma_{M_f}}\right)^5 \tag{3.39}$$

both blade and tower fatigue damage indexes are forced during the optimization to be lower than one.

Equation 3.35i forces the buckling eigenvalues λ_b to be larger than one. This requirement typically impacts the sizing of the core panels and the shell and shear webs of the blade. However, when the blade is made of carbon, the onset of buckling can dramatically affect the design of the spar caps. During the design, a preliminary verification of buckling is performed during the coarse-level design, by means of the procedure by Lindenburg and de Winkel [100]. This allows to conduct an initial buckling sizing of the shell and shear webs panels by assessing the critical buckling stresses as follows:

$$\sigma_{adm,buck} = \frac{\pi^2}{t_{panel} b^2} K_c \sqrt{D_{11} D_{22}} \tag{3.40}$$

$$\tau_{adm,buck} = \frac{\pi^2}{t_{panel} b^2} K_s \sqrt{D_{11} D_{22}^3} \tag{3.41}$$

where t_{panel} is the thickness of the shell (or web) panel, b is the width of the panel edge, D_{11} and D_{22} are the diagonal components of the out-of-plane bending matrix of the sandwich panels when computed with classic lamination theory. K_c and K_s are suitable buckling factors which account for the topology of the sandwich structure (curvature, orthotropy, shear flexibility). At several stations along the blade span, the shell panels are sized so that $\lambda_b^{shell} \geq 1$, where the buckling eigenvalue is estimated as follows:

$$\lambda_b^{shell} (\frac{\sigma}{\sigma_{adm,buck}}) + \lambda_b^{shell^2} (\frac{\tau}{\tau_{adm,buck}})^2 = 1 \tag{3.42}$$

where the stresses σ and τ are computed by applying the equivalent load system $\tilde{\boldsymbol{F}}_\delta$ to the blade. Similarly, the core within the web panels is sized so that $\lambda_b^{web} \geq 1$:

$$\lambda_b^{web^2} ((\frac{\sigma}{\sigma_{adm,buck}})^2 + (\frac{\tau}{\tau_{adm,buck}})^2) = 1 \tag{3.43}$$

Through these simplified relations it is possible to account for buckling also at the coarse-level design, while a more thorough investigation in usually performed at fine-level through the linearized buckling model.

3.3 Concluding remarks

In this Chapter, we presented a multi-layer and modular approach to the system design of wind turbines. The novelty of this method is that a nested architecture is built from the interface of a Macro Design Loop, whose task is to minimize the COE, and several individual design sub-modules, which perform the detailed sizing of specific components. In Chapter 1 we discussed how a system-engineering approach to the design of wind turbines requires to trade-off between the fidelity of the simulations and the number of variables treated by the algorithm. In our opinion, the multi-level architecture supported by `Cp-Max` is a satisfactory compromise for two reasons: firstly, the set of the design variables is split into different modules, and this allows to manage a high number of variables than those of a more traditional monolithic approach. Additionally, this broad design set does not come

at the expenses of the modelling, since the algorithm is based on a multi-body formulation that is invoked for the computation of all the necessary loads. As mentioned, `Cp-Max` is the result of a combined effort between research units at Politecnico di Milano and TUM Munich, and its capabilities have been exploited extensively in recent years. In particular, the application of the program as an SDO algorithm has been carried out by Bortolotti et al. [89] and in the context of IEA Wind Task 37 [101]. In the following, instead, we present a series of applications developed in this work in which the tool has been applied to lightweight rotor design studies.

CHAPTER 4

Definition of the PoliMI baseline rotors

In this Chapter, we introduce the design activities conducted in this work as part of our effort to develop lightweight rotor configurations for large wind turbines. As mentioned in the introductory considerations, the goal is to focus on next generation wind turbines to identify strategies for reducing the loads on the components so that a larger rotor could be designed for a given infrastructure or, alternatively, a given rotor could produce significantly lower loads, with benefits on the expected life-time of the system. As we discussed in the previous Chapter, a system-level design framework is the ideal tool for conducting such studies in particular when the underlying simulations of the turbine are based on mid-to-high fidelity models as in `Cp-Max`: the main advantage, in this case, is that the impact of a certain design choice can be directly investigated at a good level of accuracy. For a design activity to be consistent, it is paramount that all the configurations are designed according to the same objective, the same loads and the same constraints. Then, as a first step of our research, we produced different concepts which serve as baseline, or reference configurations, for subsequent analysis. At this level we started from available data of conceptual wind turbines, mainly developed within EU-funded projects, and used the SDS module of `Cp-Max` to optimize the rotor structure for a certain set of DLC. This way, we ensure that the initial guess of a certain design study has already been structurally optimized, and thus, possible beneficial or detrimental effects of a certain configuration can only be due to that configuration, and not to the fact that the initial baseline is sub-optimal. To cover a variety of applications and rotor sizes, we developed three different baseline rotors, whose fundamental properties are briefly presented in the next Sections. The first concept is widely based on the INNWIND.EU 10 MW wind turbine, which is equipped here with a fully redesigned structure made of glass-fiber. A second concept is based on the AVATAR 10 MW turbine and, similarly, we provided a new structure based on carbon-fiber. Both 10 MW baseline configurations are used in Chapter 5 to investigate

the effects of the structural tailoring on the performance of such turbines. Finally, a third configuration is a structurally feasible model of a conceptual 20 MW wind turbine, and is used in Chapter 6 to demonstrate the capabilities of `Cp-Max` through a dedicated full redesign of the rotor.

4.1 General assumptions on the design procedure

In this Section, we summarize the main assumptions supporting the design of the baseline rotors, so to clarify the choices we made and to identify the range of applications of these designs. A first and fundamental choice was to focus initially on the sole structural redesign, which was conducted with a high level of detail. Our idea was to produce, for each baseline, a fully-feasible structural layout through the combination of a coarse/aero-elastic design and a finer one based on 3D FEM, as discussed in § 3.2.5. Since the focus of this work is on structural techniques for lightweight solutions, it was important to rely on fully-validated initial layouts. Through the development of our baselines, then, the aerodynamic shape of the rotor is given and frozen, and similarly, the air tables of the airfoils along the blade are known. The redesign focuses on the structural part of the rotor, so that the other components of the turbine, in particular the tower, are fixed. For what concerns the prebend of the blade, all three solutions have been designed with a straight axis, to simplify the configurations as much as possible and to possibly conduct the redesign of the prebend through the PDS module at a later stage.

4.1.1 Structural topology

The SDS module of `Cp-Max` does not introduce significant limitations on the sectional topology of the blade, and in fact, a wide library of sectional arrangements is available: different part of the blade can actually be associated to different sectional topologies, to offer the maximum flexibility and adaptability. The development of our baselines was conducted with simplicity in mind, so we selected a rather typical sectional arrangement which is based on the *spar-box* layout rendered in Fig. 4.1.

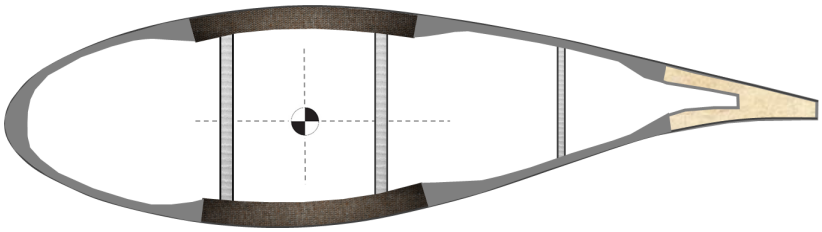

Figure 4.1: *Rendering of the assumed sectional topology.*

The essential elements of this frame are two spar caps and two shear webs, which are bonded together to form the main box. Given the wide chord of multi-megawatt rotors, however, a third web has been selectively added to the section: is main purpose is to reduce the free-length of the shell panels and to retard the onset of buckling, whereas its impact on the internal redistribution of stresses is only modest. The sectional description in the SDS is based on `ANBA`, and requires that the section is described by means of equivalent panels, each of them associated to a certain distribution of materials. In the following, the panels which the section is divided into are named *sectional elements*, as they represent

fundamental units within the section which carry unmodifiable properties. Their spanwise starting and ending positions, as well as the chord-wise placement within each section are defined by the variable τ_{sec} and supplied to the MDL through the structure 3.3. A sketch of the various sectional elements is given by the top picture of Fig. 4.2.

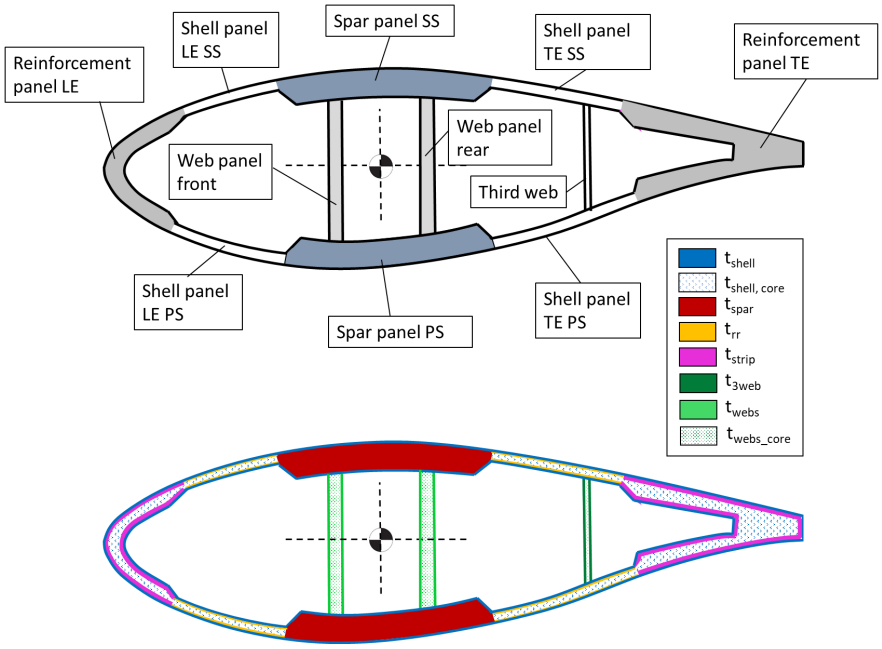

Figure 4.2: *Modelling of the section: sectional elements (top) and structural components (bottom).*

As we mentioned in § 3.2.5, an arbitrary distribution of materials can be assigned to each sectional element, and this typically allows to describe highly-detailed layups. In the design of the baseline, we assumed that a certain number of *structural components* is assigned to the various layers according to the stacking sequence of Fig. 4.2 (see the bottom picture). According to the legend, eight components are defined, and each of them is linked to one, or more, structural design variables. In fact, the thickness of a given component can assume everywhere in the section a unique value, which is controlled by a single design variable, but it can also be described by different values at each panel: in that case, multiple design variables are associated to the thickness of the same components in different panels. Recalling the definition of the structural variables array 3.33b, in our applications we assume

that it follows the breakdown:

$$\boldsymbol{p}_s = [\boldsymbol{t}_b^{Fabrics},\ \boldsymbol{t}_b^{Core}] \tag{4.1a}$$
$$\boldsymbol{t}_b^{Fabrics} = [\boldsymbol{t}_{shell},\ \boldsymbol{t}_{spar},\ \boldsymbol{t}_{strip},\ \boldsymbol{t}_{webs},\ t_{rr},\ t_{3web}] \tag{4.1b}$$
$$\boldsymbol{t}_{shell} = [t_{shell}^{TE,SS},\ t_{shell}^{LE,SS},\ t_{shell}^{LE,PS},\ t_{shell}^{TE,PS}] \tag{4.1c}$$
$$\boldsymbol{t}_{spar} = [t_{spar}^{SS},\ t_{spar}^{PS}] \tag{4.1d}$$
$$\boldsymbol{t}_{webs} = [t_{webs}^{front},\ t_{webs}^{rear}] \tag{4.1e}$$
$$\boldsymbol{t}_{strip} = [t_{strip}^{LE},\ t_{strip}^{TE}] \tag{4.1f}$$
$$\boldsymbol{t}_b^{Core} = [\boldsymbol{t}_{shell,core},\ \boldsymbol{t}_{webs,core},\ t_{3web,core}] \tag{4.1g}$$
$$\boldsymbol{t}_{shell,core} = [t_{shell,core}^{TE,SS},\ t_{shell,core}^{LE,SS},\ t_{shell,core}^{LE,PS},\ t_{shell,core}^{TE,PS}] \tag{4.1h}$$
$$\boldsymbol{t}_{webs,core} = [t_{webs,core}^{Front},\ t_{webs,core}^{Rear}] \tag{4.1i}$$

Where TE and LE indicate respectively the panels towards the trailing edge and those towards the leading edge. Similarly, SS and PS indicate panels defined on the suction-side (and, respectively, on the pressure-side) of the section. According to Eq. 4.1c for example, we see that the thickness of the shell fabric is independent on the four shell panels, so that four design variables are associated to this component. Similarly, the two spar cap components are assumed to be independent, so that each of them can evolve independently during the design (see Eq. 4.1d). Similar considerations hold true for the leading and trailing reinforcements declared in Eq. 4.1e and for the distribution of the core components along the section, whose layout is summarized by Eqs. 4.1f, 4.1g and 4.1h. The component t_{rr} represents what we called a *root reinforcement*, that is, a thin extra-layer of material which is added to certain sectional elements in the vicinity of the root. Its main purpose is to help the internal distribution of stress in that area, although it typically contributes also to the in-plane and out-of-plane stiffness of the blade. In addition to the specification of the components, it is necessary to define a lamination sequence for each panel, so that the correct order of plies can be accurately accounted for. In this study we defined two different lamination sequences, whose mapping on the various sectional elements is defined in Tab. 4.1. Sequence A is used for the design of the two 10 MW references, whereas sequence B is used for the 20 MW baseline. For each panel, the Table lists all the components which make-up the stacking sequence. For surface panels, the components are given from the outer-most to the inner-most. For internal elements (mainly the three webs), the order is from the one at the front to the one at the rear. The main difference between the two sequences lies in the lamination of the root reinforcement t_{rr}. In Sequence A this layer is only added to the shell panels, while in sequence B it is applied to all the surface elements. It was found, mainly at 3D FEM level, that such distribution ensures better performance of the structure. It must be noticed that all the layers of a certain lamination sequence are either associated to one of the design variables 4.1 or computed from a combination of them. See, for example, how the shell thickness at the outer surface of the spar panels is computed as the average of the closest shell panels. This is intended to limit the number of degrees of freedom. Clearly, one could define his/her own lamination sequence within the SDS in `Cp-Max`, as long as a mapping between the sectional elements and the structural components is correctly filed. Eventually, for each design variable, it is necessary to define a suitable discretization on a certain number of optimization sections $\boldsymbol{\eta}_{OptiSec}$ and provide the initial thickness distribution $\boldsymbol{t_i} = \boldsymbol{t_i}(\boldsymbol{\eta}_{OptiSec})$.

Table 4.1: *Stacking sequences of the sectional elements, where* $xx = [TE, LE]$, $yy = [PS, SS]$ *and* $zz = [front, rear]$

Sectional element	Sequence A	Sequence B
Shell panel xx yy	$0.5 * t_{shell}^{xx,yy}$ $0.5 * t_{rr}$ $t_{shell,core}^{xx,yy}$ $0.5 * t_{shell}^{xx,yy}$ $0.5 * t_{rr}$	Same
Spar panel yy	$0.5 * (t_{shell}^{TE,yy} + t_{shell}^{LE,yy})$ t_{spar}^{yy} $0.5 * (t_{shell}^{TE,yy} + t_{shell}^{LE,yy})$	$0.5 * (t_{shell}^{TE,yy} + t_{shell}^{LE,yy})$ $0.5 * t_{rr}$ t_{spar}^{yy} $0.5 * t_{rr}$ $0.5 * (t_{shell}^{TE,yy} + t_{shell}^{LE,yy})$
Web panel zz	$0.5 * t_{webs}^{zz}$ $t_{webs,core}^{zz}$ $0.5 * t_{webs}^{zz}$	Same
Reinforcement panel xx	$0.5 * (t_{shell}^{xx,SS} + t_{shell}^{xx,PS})$ $0.5 * t_{strip}^{xx}$ $max(t_{shell,core}^{xx,PS}, t_{shell,core}^{xx,SS})$ $0.5 * t_{strip}^{xx}$ $0.5 * (t_{shell}^{xx,SS} + t_{shell}^{xx,PS})$	$0.5 * (t_{shell}^{TE,yy} + t_{shell}^{LE,yy})$ $0.5 * t_{rr}$ $0.5 * t_{strip}^{xx}$ $max(t_{shell,core}^{xx,PS}, t_{shell,core}^{xx,SS})$ $0.5 * t_{strip}^{xx}$ $0.5 * t_{rr}$ $0.5 * (t_{shell}^{TE,yy} + t_{shell}^{LE,yy})$
Third web	$0.5 * t_{3web}$ $t_{3web,core}$ $0.5 * t_{3web}$	Same

4.1.2 Materials

To correctly build a sectional layout, each structural component must be uniquely assigned to a certain material. In the definition of the baseline rotors, we followed a quite common strategy, in which the main stress-bearing elements are laminated from a unidirectional material. The mechanical properties of two different unidirectional materials are given in Tab. 4.2, in terms of longitudinal and lateral Young modulus E_{11}, E_{22}, Poisson's ratio

ν_{12}, shear modulus G_{12} and the density ρ of the fabric. For brevity, only the longitudinal admittable stress under both tension $\sigma_{zz,max}$ and compression $\sigma_{zz,min}$ are provided. A first unidirectional, identified by the code UD-(G) represents a classic laminate made of E-glass fibers. It is used on the 10 MW glass design and for the 20 MW one. A second material is based on the properties of pre-preg carbon fiber and is identified by the code UD-(C): this is employed for the design of the 10 MW (C) rotor. We always assume that both of the spar components and the root reinforcement are made of unidirectional material. The leading and trailing edge reinforcement, instead are always assumed to be made of UD-(G), regardless of which material is used for the spar. It is also assumed that the shell components are made of triaxial glass fiber. The same material is used for the external layers of the third web. The two main webs, on the contrary, are assumed to be made of biaxial glass fiber. A unique core material, namely balsa wood, has been assigned to all the sandwich panels of the shell and the webs.

Table 4.2: *Mechanical properties of the materials.*

Property	Units	UD-(G)	UD-(C)	Triaxial	Biaxial	Balsa
Components		$\boldsymbol{t_{spar}}$ t_{rr} $\boldsymbol{t_{strip}}$	$\boldsymbol{t_{spar}}$ t_{rr}	$\boldsymbol{t_{shell}}$ t_{3web}	t_{webs}	$\boldsymbol{t_{shell,core}}$ $\boldsymbol{t_{webs,core}}$ $t_{3web,core}$
E_{11}	[GPa]	41.63	115.1	21.79	13.92	0.05
E_{22}	[GPa]	14.93	7.56	14.67	13.92	0.05
ν_{12}	[-]	0.241	0.3	0.478	0.533	0.38
G_{12}	[GPa]	5.047	3.96	9.413	11.50	0.15
ρ	[kg/m3]	1915	1578	1845	1845	110
$\sigma_{zz,max}$	[MPa]	876.1	1318	480.4	223.2	0.4
$\sigma_{zz,min}$	[MPa]	625.8	620	393	209.2	0.31

In addition to the structural mass, which directly depends on the thickness of the individual components, a dedicated model allows to compute the parasitic masses due to several contributions. The latter do not typically provide any property of strength or stiffness, however, their computation can have an impact on the frequencies and the displacements of the blades. The parasitic or *non-structural* masses can be split into surface or linear contributions, as detailed by Table 4.3.
In addition to these masses, an uniform layer of paint is included in the lamination sequence of all the surface sectional elements along the blade. An example of the resulting spanwise distribution of the non-structural masses is given in Fig. 4.3.

4.1.3 Design load cases

The choice of the relevant DLC to be included in the set of the dynamic analysis was made in two stages. At first, a full set of DLC was performed on the initial guess according

Table 4.3: *Breakdown of the non-structural masses.*

Model	Units	Value	Component
Surface	[kg/m2]	2.5	Resin uptake shell
		0.80	Resin uptake single web
Linear	[kg/m]	2.30	Glue mass single web
		2.88	Glue mass leading/trailing edge
		0.50	Lightning system
		3.90	Bonding plies single web

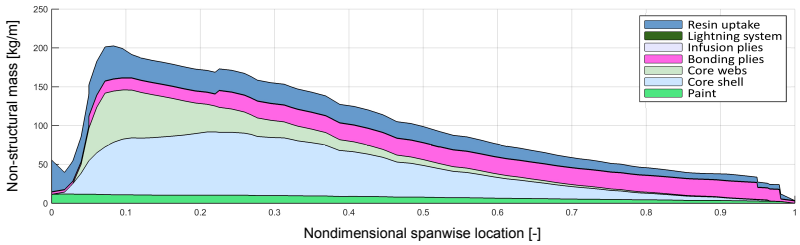

Figure 4.3: *Distribution of the non-structural masses components for a 10 MW rotor.*

to the IEC standards. This included multi-seeds simulations for turbulent cases. Then, a sub-set was built so that all the DLC giving the ultimate loads and displacements could be accounted for during the design. The resulting subset is briefly summarized in Tab. 4.4, and includes normal operating conditions, extreme turbulence, several faults including grid loss and individual pitch runaway and parking conditions with and without control. During the design, only one seed was considered in turbulent simulations, however, for each turbulent case, the seed giving the highest loads and deflection was employed. With this construction, the number of sizing DLC was reduced to approximately one-hundred cases, with a total computational time of 6-8 hours on a normal desktop.
All the baseline rotors have been designed with the same control strategy, which corresponds to option $\alpha_r = 2$ in the CST (see § 3.2.3). The logic is then based on the combination of a PID controller which manages the collective blade pitch and a second PID on the electrical torque. For each configuration, the setting of the target rotor speed, as well as that of the minimum pitch schedule comes directly form the computation of the $Cp - TSR$ curves, while the tuning of the different gains has been mainly performed by a trial-and-error procedure.

4.1.4 General features of the turbines

The structural definition described in the following Sections aims at providing a feasible structural design of the rotor for each of the three baseline turbines considered in this work.

Table 4.4: *Selected DLC for the design of the baseline rotors.*

DLC	Wind Type	Wind Speed	Yaw Mis.	Fault	Safety Factor
1.1	NTM	$v_{in} : v_{out}$	-	-	1.35
1.2	NTM	$v_{in} : v_{out}$	-	-	1
1.3	ETM	$v_{in} : v_{out}$	-	-	1.35
2.1	NTM	$v_{in} : v_{out}$	-	Grid Loss	1.35
2.2	NTM	$v_{in} : v_{out}$	-	Pitch Runaway	1.35
2.3	EOG	$v_r,\ v_r \pm 2,\ v_{out}$	-	Grid Loss	1.1
6.1	EWM	v_{ref}	$-8° : 8°$	-	1.35
6.2	EWM	v_{ref}	$-180° : 180°$	Grid Loss	1.1

This means that a full structural design is conducted by the SDS of `Cp-Max` for a given turbine, so that its rotor-related ICC is minimized through the optimization of all the structural components. The general characteristics of the reference turbines are provided in Tab. 4.5.

The first configuration is based on the INNWIND.EU 10 MW wind turbine and is representative of a next-generation concept in which the rotor structure is basically designed with glass-fiber composites. The aero-elastic model of the turbine is built on the original data sheet from Bak et al. [75], which implies that the global properties of the turbine like diameter, hub height and blade length are assumed to be the same. Similarly, the blade aerodynamic shape, the distribution of airfoils and the corresponding aerodynamic tables are assumed to be coherent to those of the original turbine. To simplify the initial structural definition, we conducted a design based on a straight axis with no prebend, whereas the original INNWIND.EU rotor has a tip prebend of 6 metres. However, preliminary load analysis showed that the maximum tip displacement was a severe constraint on the design of the structural components, and in particular the spar caps: to relieve a bit this constraint we introduced an additional cone angle, which is then increased from the original value of 2.5 degrees.

The second concept is based on the reference wind turbine developed during project AVATAR: the general assumptions on the wind turbine configuration are summarized in Tab. 4.5 and fully detailed by Lekou et al. [102]. In this case, the turbine is designed to be a Low-Induction Rotor, which means that the blade is designed to work sub-optimally in order to develop lower loads, as we discussed previously in § 2.4.3. Clearly, this requires that a longer blade is designed in order to compensate for the energy drop and, in our studies, this led us to use carbon instead of glass for this configuration. Like the previous turbine, the structural design is conducted for a frozen model of the wind turbine and for a given aerodynamic design.

Our last definition concerns a preliminary design of a 20 MW wind turbine, whose aero-elastic properties have been obtained by upscaling the INNWIND.EU wind turbine (see Chaviaropoulos et al. [103]). Our idea is to conduct a full structural design of the concept

Table 4.5: *Characteristics of the baseline wind turbines.*

	Baseline 10 MW (G)	Baseline 10 MW (C)	Baseline 20 MW
Design concept	Classic, glass	Low-Induction, carbon	Classic, glass
Rated power [MW]	10	10	20
IEC class [-]	1A	1A	1C
Blade length [m]	86.35	100.08	122.15
Rotor diameter [m]	178.3	205.76	252.2
Hub height [m]	119	132.5	167.9
Nacelle up-tilt [deg]	5	5	5
Rotor cone [deg]	4.65	2.5	2.5

to investigate if a feasible design based on glass is achievable for such size of rotors.

4.2 Definition of the Baseline 10 MW (G) glass design

The internal layout for the **Baseline 10 MW (G)** follows the assumptions discussed in § 4.1. A full structural design has been conducted by the SDS through both the aero-elastic or *coarse* level and the finer description through the detailed 3D FEM model. For this solution, we chose a number of optimization sections equal to 20, for a total number of design variables close to 100. The original (and frozen) distributions of twist is reported for completeness in the left portion Fig. 4.4, while the right part shows the distribution of the percent thickness.

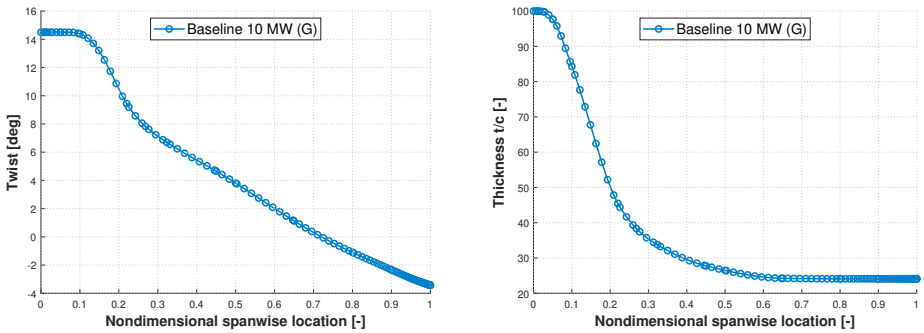

Figure 4.4: *Baseline 10 MW (G): spanwise twist (left) and percent thickness (right).*

Figure 4.5 shows the planform of the blade and the positioning of the various sectional elements. In this view, it is assumed that the x-axis coincides with the blade axis, while the y-axis id defined form the leading edge to the trailing edge. Consistently, the z-axis goes from the pressure to the suction side of the blade. It is possible to see the two spar panels highlighted by the red lines: for simplicity, both caps are defined at the same chordwise position, which lies exactly across the blade axis. It is interesting to notice how the definition

of the spar can be divided into a monolithic portion of constant width and a trapezoidal region which connects the spar caps to the root region: this solution has been studied at FEM level and we found that this transitional zone ensures a better transmission of the stresses from the spar to the blade root. Two main webs are defined by the continuous green lines, with the *front* one lying toward the leading edge and the *rear* one toward the trailing edge. The positioning and extension of the reinforcement panels, identified by continuous purple lines, has been decided through a dedicated parametric analysis. A third web, identified by the aquamarine line, contributes to reduce the free-length of the shell panels, as discussed previously.

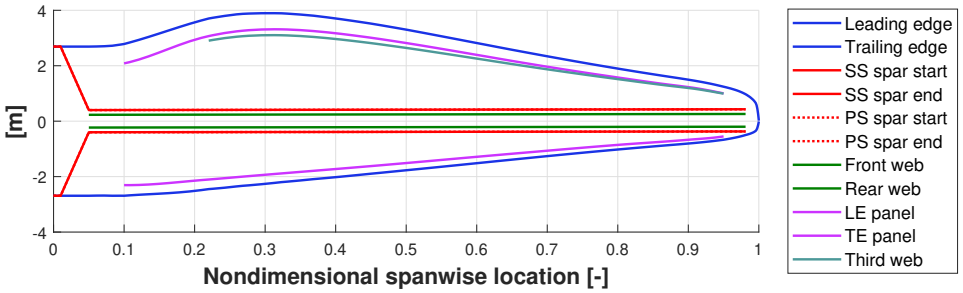

Figure 4.5: *Baseline 10 MW (G): blade planform and positioning of the sectional elements.*

Considering the relatively high number of fully-resolved DLC that we included in the design, we decided to introduce some topological assumption in order to reduce the total number of design variables. Specifically, we assumed that the thickness of shell components are identical in the four shell panels. Similarly, we assumed that the thickness of the webs component is identical for the two main webs. This can be formalized as follows:

$$t_{shell}^{TE,SS} = t_{shell}^{LE,SS} = t_{shell}^{LE,PS} = t_{shell}^{TE,PS} \tag{4.2a}$$

$$t_{webs}^{front} = t_{webs}^{rear} \tag{4.2b}$$

while these assumption are broadly justifiable for the design of the composite layers of the sandwich panels, the core thickness along the panels have been left free to evolve independently, as their design is primarily driven by buckling, which could affect certain regions of the blade more than others. The association of a certain component to a certain material follows that presented in Tab. 4.2, where the glass unidirectional is used for the lamination of the spar caps, the strip reinforcements and the root reinforcement. The design has been conducted by assuming the INNWIND.EU cost models, so that a minimization of the ICC usually coincides with a minimization of the total blade mass.

The optimal value of each structural component along the 20 optimization sections is given in Tab. 4.6, which lists all the variables related to the composites, and in Tab. 4.7, which gives the spanwise distribution of the core. The lamination of the structural component on the sectional elements follows the Sequence A summarized in Tab. 4.1. A sketch of the components-breakdown is given for different sectional elements in Fig. 4.6 (Shell panel TE SS), 4.7 (Spar panel SS),Fig. 4.8 (Web panel front), and 4.9 (Reinforcement panel LE). It must be noticed that the root reinforcement is identified by yellow shades in the picture, while the unidirectional in the spar is red and that in the reinforcements is purple. This notation has been adopted to match that of Fig. 4.2, however, all these components are based on the same unidirectional material. For the optimal solution, Fig. 4.10 gives the sectional stiffness in the flapwise (left) and edgewise(right) directions. Those graphics are given in a *spanwise local frame* in which, at a certain section, the y axis goes along the chord from the trailing to the leading edge.The z axis goes normal to chord from the pressure to the suction side so that, by construction, the x axis goes along the blade fro root to tip. The local frame, then follows the local aerodynamic twist. Figure 4.11 provides instead the torsional stiffness (on the left) and the spanwise distributed mass. The latter accounts for the mass of the materials as well as the parasitic contributions discussed in § 4.1.2. A list of selected KPIs for the rotor are provided in Table 4.8: the left column provides some useful information about the aero-structural design. From the top to the bottom, the Table lists the first flapwise frequency of the isolated clamped blade, the maximum ultimate tip displacement registered along the DLC considered, the total blade mass, the AEP as computed from time-averaged simulations in Normal Turbulence Model (NTM), and the corresponding COE. The central column provides a list of important ultimate loads, as computed along different components of the turbine. It must be kept in mind that the bending moment here refers to the maximum multi-directional load rather than to a single component. Then, for example, the bending at blade root (BR) indicates the maximum value of the combined flapwise/edgewise moment. The right-most column, eventually, provides selected figures of the fatigue equivalent loads. All these indicators will be used as reference value in the lightweight design activities discussed in the next Chapters.

Table 4.6: *Baseline 10 MW (G): spanwise optimal values of the structural components (fabrics)*

	Component thickness [mm]											
η	$t_{shell}^{TE,SS}$	$t_{shell}^{LE,SS}$	$t_{shell}^{TE,PS}$	$t_{shell}^{LE,PS}$	t_{spar}^{SS}	t_{spar}^{PS}	t_{webs}^{front}	t_{webs}^{rear}	t_{3web}	t_{strip}^{LE}	t_{strip}^{TE}	t_{rr}
0.000	50.00	50.00	50.00	50.00	15.00	15.00	-	-	-	-	-	15.00
0.010	50.00	50.00	50.00	50.00	15.00	15.00	-	-	-	-	-	15.00
0.025	32.00	32.00	32.00	32.00	21.00	21.00	-	-	-	-	-	15.00
0.050	11.00	11.00	11.00	11.00	31.00	31.00	2.50	2.50	-	-	-	7.52
0.083	7.00	7.00	7.00	7.00	37.00	37.00	2.50	2.50	-	-	-	6.00
0.100	6.20	6.20	6.20	6.20	41.00	41.03	2.50	2.50	-	4.71	4.71	4.71
0.163	3.90	3.90	3.90	3.90	55.60	56.08	2.50	2.50	-	5.95	6.30	4.59
0.220	2.40	2.40	2.40	2.40	81.29	81.20	4.43	4.43	4.00	5.31	7.83	4.20
0.268	2.20	2.20	2.20	2.20	91.25	91.36	5.62	5.62	4.01	4.55	7.78	2.57
0.323	2.51	2.51	2.51	2.51	94.13	94.26	6.36	6.36	4.01	4.42	7.67	1.23
0.369	2.65	2.65	2.65	2.65	97.42	95.93	6.77	6.77	4.01	3.81	7.43	0.84
0.450	2.76	2.76	2.76	2.76	98.76	92.77	7.41	7.41	4.01	3.50	7.01	-
0.500	2.63	2.63	2.63	2.63	101.17	93.76	7.25	7.25	4.01	3.02	7.02	-
0.650	1.70	1.70	1.70	1.70	66.76	69.15	7.02	7.02	4.01	1.84	4.62	-
0.800	1.50	1.50	1.50	1.50	42.94	43.96	5.37	5.37	4.00	0.81	1.77	-
0.900	1.50	1.50	1.50	1.50	27.60	27.87	5.37	5.37	4.00	0.80	1.53	-
0.950	1.50	1.50	1.50	1.50	14.66	14.67	5.37	5.37	4.00	0.80	1.00	-
0.981	1.50	1.50	1.50	1.50	14.66	14.67	5.37	5.37	-	-	-	-
1.000	1.50	1.50	1.50	1.50	-	-	-	-	-	-	-	-

Table 4.7: *Baseline 10 MW (G): spanwise optimal values of the structural components (fillers)*

	Component thickness [mm]						
η	$t^{TE,SS}_{shell,core}$	$t^{LE,SS}_{shell,core}$	$t^{LE,PS}_{shell,core}$	$t^{TE,PS}_{shell,core}$	$t^{front}_{webs,core}$	$t^{rear}_{webs,core}$	$t_{3web,core}$
0.000	-	-	-	-	-	-	-
0.010	-	-	-	-	-	-	-
0.025	1.00	1.00	1.00	1.00	-	-	-
0.050	21.00	23.00	19.00	17.00	99.00	97.00	-
0.083	29.00	29.00	25.00	25.00	101.00	97.00	-
0.100	33.00	27.00	27.00	27.00	99.00	95.00	-
0.163	63.00	27.00	25.00	77.00	81.00	77.00	-
0.220	75.00	23.00	23.00	47.00	63.00	57.00	9.00
0.268	81.00	23.00	23.00	57.00	55.00	49.00	7.00
0.323	81.00	21.00	19.00	61.00	47.00	43.00	5.00
0.369	77.00	21.00	19.00	59.00	41.00	39.00	3.00
0.450	69.00	17.00	17.00	53.00	33.00	31.00	1.00
0.500	61.00	15.00	17.00	49.00	29.00	27.00	1.00
0.650	45.00	13.00	15.00	35.00	21.00	19.00	1.00
0.800	25.00	7.00	9.00	19.00	13.00	11.00	1.00
0.900	13.00	3.00	5.00	7.00	7.00	5.00	1.00
0.950	7.00	1.00	3.00	3.00	3.00	3.00	1.00
0.981	5.00	1.00	1.00	3.00	3.00	1.00	-
1.000	-	-	-	-	-	-	-

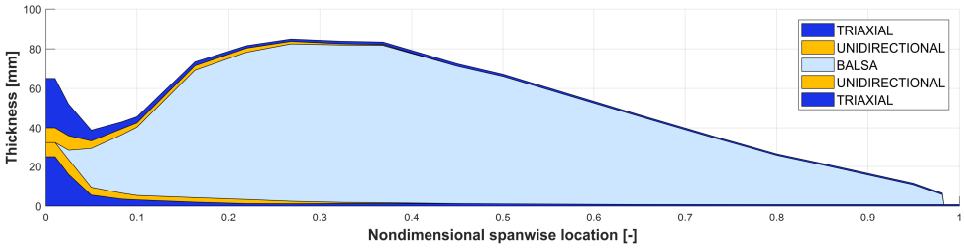

Figure 4.6: *Baseline 10 MW (G): lamination of the Shell TE SS panel.*

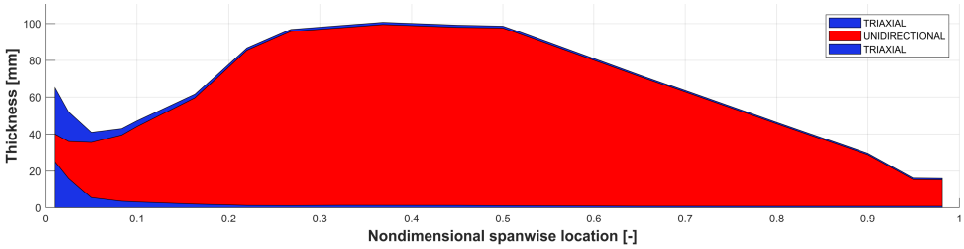

Figure 4.7: *Baseline 10 MW (G): lamination of the Spar SS panel.*

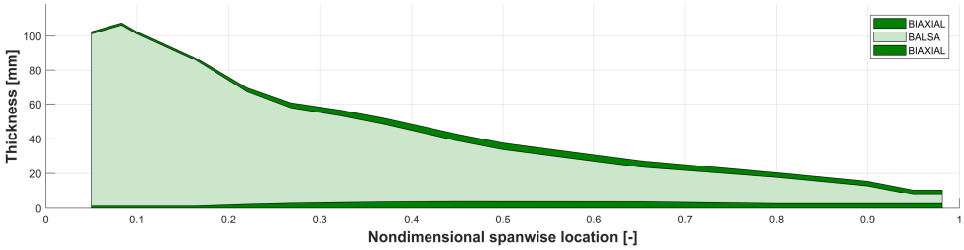

Figure 4.8: *Baseline 10 MW (G): lamination of the Web panel front.*

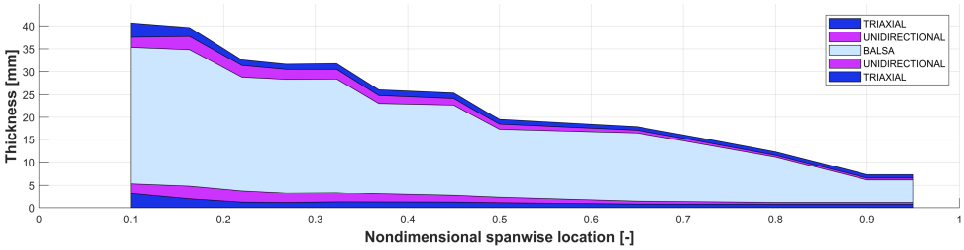

Figure 4.9: *Baseline 10 MW (G): lamination of the Reinforcement panel LE.*

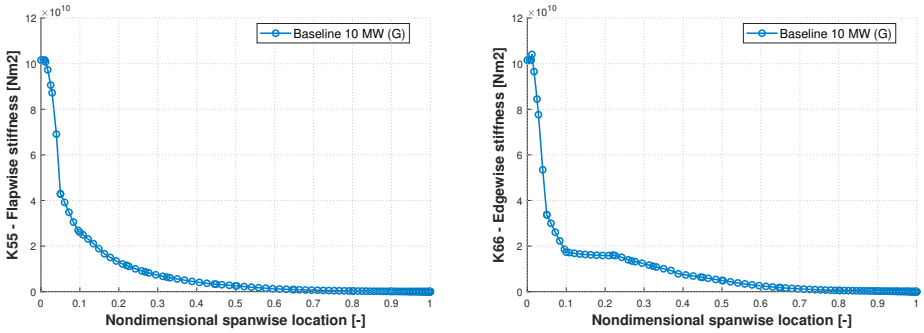

Figure 4.10: *Baseline 10 MW (G): flapwise (left) and edgewise (right) stiffness.*

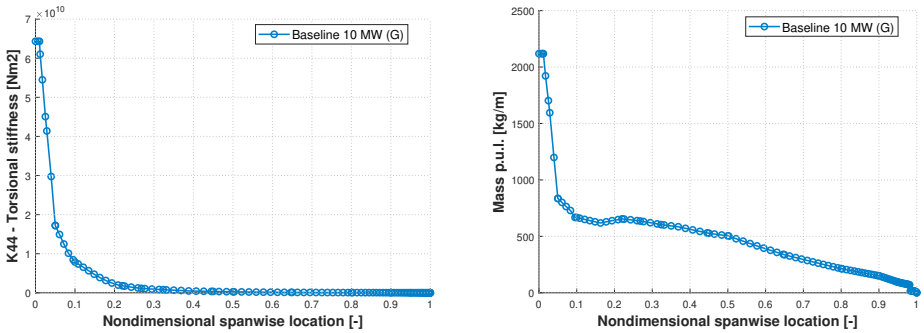

Figure 4.11: *Baseline 10 MW (G): torsional stiffness (left) and mass per unit length (right).*

Table 4.8: *Baseline 10 MW (G): KPI, ultimate and fatigue loads. BR is blade root, HC is hub center, TT is tower top and TB is tower root*

Baseline 10 MW (G)					
Performance		Ultimate loads		Fatigue DELs	
Frequency:	0.56 Hz	BR bending:	73.37 MNm	BR flapwise:	35.14 MNm
Displacement:	13.04 m	HC thrust:	3.15 MN	HC nodding:	26.84 MNm
Blade mass:	42575 kg	HC bending:	59.67 MNm	HC yawing :	24.87 MNm
AEP:	46.40 GWh	TT bending:	62.47 MNm	TT FA:	26.53 MNm
CoE:	74.93 €/MWh	TB bending:	491.7 MNm	TB FA:	135.6 MNm

4.3 Definition of the Baseline 10MW (C) carbon design

A second structural definition has been conducted for the carbon-based version of the 10 MW wind turbine, hereafter referred as **Baseline 10 MW (C)**. This solution is based on the Low-Induction configuration developed within project AVATAR, which implies that the blade is longer than that of the glass-based design. In this application, then, the spar caps and the root reinforcement are laminated with the carbon material presented in Table 4.2. However, the leading and trailing edge reinforcement along the strips are made of unidirectional glass. Like the previous case, we decided to perform the structural redesign on a set of 20 optimization stations. However, since the carbon has a very high longitudinal modulus, we adopted a finer discretization towards the root of the blade, mainly to better control the thickness of the carbon elements and thus preserve the smoothness of the stiffness distributions. The functions of the twist and the percent thickness are reported in Fig. 4.12 while a full description of the aerodynamic model is provided by Lekou et al. [102]. It must be noticed that the distribution of twist has been conceived to work along the low-induction concept: then, it should be expected that the sections work quite far from their ideal aerodynamic efficiency. A planform-view of the main sectional elements is given in Fig. 4.13: it is possible to see that we adopted, like the previous case, two constant-width spar caps. However, their placement is no longer symmetric with respect to blade axis but, on the contrary, there is a small twist towards the trailing edge. This placement was obtained through a small geometric optimization which allowed to place the spar caps close to the maximum local thickness of the section. The trapezoidal transition region between the monolithic spar cap and the root of the blade was maintained, in particular because this is a critical region when high compressive stresses are transmitted from the spar to the root. Figure 4.14, for example, shows the first buckling eigenvalue computed with the loads coming from one of the most demanding conditions, namely ETM wind close to the rated wind speed. Unlike the glass version of the 10 MW, whose design is mainly constrained by deflection requirements, the carbon version is severely affected by buckling, up to the point that almost the entire spar caps are sized for local concentration of stress. Unlike the previous case, here to obtain a fully-feasible solution required several interfaces between the aero-elastic design performed by the SDS and the 3D FEM analyses. The structural design follows the same assumptions of § 4.2, in particular, the simplifications introduced by Eqs. 4.2 hold true for the carbon design. The optimal values of the structural components is given in Table 4.9 (fabrics) and in Table 4.10. The corresponding lamination sequence of the sectional elements, which still follows the stacking sequence A, is shown in Figs. 4.15 to 4.18. The resulting flapwise and edgewise stiffness of the optimal blade are given in Fig. 4.19, while the torsional stiffness and the mass per unit length in Fig. 4.20. Ultimately, the same KPI computed for the **Baseline 10 MW (G)** are provided for the carbon-based rotor in Table 4.11. It must be noticed that, although the wind turbine is based on the low-induction concept, the driving loads are significantly higher than those of the glass design. The multi-directional bending at the hub center, in particular, is almost doubled and similar considerations apply to the bending at the tower base. Similarly, most fatigue loads are higher for the carbon design, although interestingly enough DEL in the fore-aft direction at tower base are similar between the two turbines. We can draw the partial conclusion that, when a full lot of loading conditions is considered, a longer blade produces significantly higher loads, regardless to the fact that it follows a classic design or a low-induction one. However, it is true that the carbon design, being larger in size, produces a higher energy capture and reduces the COE. However, we must remark that the computation of the COE is made according to a scaling model and a thorough evaluation of the bill of materials

with a detailed blade cost model would almost certainly result in a higher blade cost. A full account of the design procedure of the **Baseline 10 MW (C)** is given in a dedicated report by Croce et al. [104].

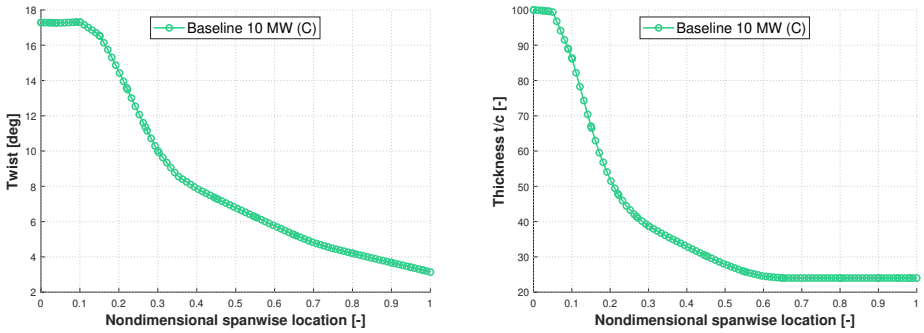

Figure 4.12: *Baseline 10 MW (C): spanwise twist (left) and percent thickness (right).*

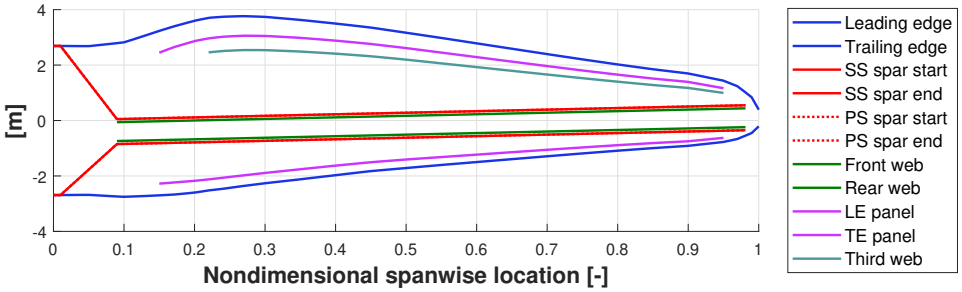

Figure 4.13: *Baseline 10 MW (C): blade planform and positioning of the sectional elements.*

Table 4.9: *Baseline 10 MW (C): spanwise optimal values of the structural components (fabrics)*

	Component thickness [mm]											
η	$t_{shell}^{TE,SS}$	$t_{shell}^{LE,SS}$	$t_{shell}^{TE,PS}$	$t_{shell}^{LE,PS}$	t_{spar}^{SS}	t_{spar}^{PS}	t_{webs}^{front}	t_{webs}^{rear}	t_{3web}	t_{strip}^{LE}	t_{strip}^{TE}	t_{rr}
0.000	38.00	38.00	38.00	38.00	22.00	-	-	-	-	-	-	22.00
0.010	38.00	38.00	38.00	38.00	22.00	-	-	-	-	-	-	22.00
0.025	15.00	15.00	15.00	15.00	27.00	27.00	-	-	-	-	-	22.00
0.037	13.00	13.00	13.00	13.00	30.00	30.00	-	-	-	-	-	9.15
0.051	12.50	12.50	12.50	12.50	34.00	34.00	-	-	-	-	-	8.51
0.071	12.00	12.00	12.00	12.00	40.85	40.85	-	-	-	-	-	7.50
0.090	11.00	11.00	11.00	11.00	49.35	52.00	1.00	1.00	-	-	-	7.14
0.100	10.00	10.00	10.00	10.00	50.59	53.79	1.00	1.00	-	-	-	7.20
0.150	9.00	9.00	9.00	9.00	52.00	72.62	1.00	1.00	-	17.32	14.81	6.49
0.220	8.50	8.50	8.50	8.50	53.00	75.15	1.00	1.00	2.60	16.10	14.90	4.23
0.268	8.00	8.00	8.00	8.00	54.42	77.41	2.04	2.04	2.60	15.56	13.65	3.43
0.300	7.50	7.50	7.50	7.50	55.27	79.22	2.78	2.78	2.60	14.67	13.65	3.25
0.450	7.00	7.00	7.00	7.00	56.54	85.00	5.71	5.71	2.60	13.95	12.54	-
0.550	6.50	6.50	6.50	6.50	56.19	79.00	6.74	6.74	2.60	10.01	9.40	-
0.650	6.00	6.00	6.00	6.00	42.63	61.05	6.48	6.48	2.60	7.63	6.17	-
0.800	5.00	5.00	5.00	5.00	30.00	30.00	4.42	4.42	2.38	1.00	1.00	-
0.900	4.00	4.00	4.00	4.00	10.00	10.00	3.29	3.29	1.58	0.10	0.34	-
0.950	3.75	3.75	3.75	3.75	10.00	10.00	3.29	3.29	0.95	0.10	0.18	-
0.981	3.50	3.50	3.50	3.50	10.00	10.00	3.29	3.29	-	-	-	-
1.000	2.50	2.50	2.50	2.50	-	-	-	-	-	-	-	-

Table 4.10: *Baseline 10 MW (C): spanwise optimal values of the structural components (fillers)*

	Component thickness [mm]						
η	$t^{TE,SS}_{shell,core}$	$t^{LE,SS}_{shell,core}$	$t^{LE,PS}_{shell,core}$	$t^{TE,PS}_{shell,core}$	$t^{front}_{webs,core}$	$t^{rear}_{webs,core}$	$t_{3web,core}$
0.000	-	-	-	-	-	-	-
0.010	-	-	-	-	-	-	-
0.025	1.00	1.00	1.00	1.00	-	-	-
0.037	7.00	7.00	7.00	7.00	-	-	-
0.051	9.00	9.00	11.00	9.00	-	-	-
0.071	13.00	13.00	13.00	15.00	-	-	-
0.090	19.00	15.00	15.00	21.00	63.00	63.00	-
0.100	21.00	17.00	17.00	23.00	63.00	63.00	-
0.150	43.00	13.00	15.00	67.00	57.00	57.00	-
0.220	49.00	15.00	15.00	49.00	53.00	53.00	25.00
0.268	51.00	13.00	15.00	49.00	47.00	47.00	15.00
0.300	51.00	13.00	13.00	49.00	43.00	45.00	11.00
0.450	45.00	9.00	9.00	41.00	27.00	29.00	3.00
0.550	39.00	7.00	9.00	33.00	19.00	21.00	1.00
0.650	31.00	7.00	9.00	25.00	17.00	17.00	1.00
0.800	15.00	5.00	7.00	11.00	13.00	13.00	1.00
0.900	9.00	3.00	5.00	5.00	11.00	9.00	1.00
0.950	3.00	1.00	1.00	1.00	7.00	5.00	1.00
0.981	3.00	1.00	1.00	1.00	3.00	3.00	-
1.000	-	-	-	-	-	-	-

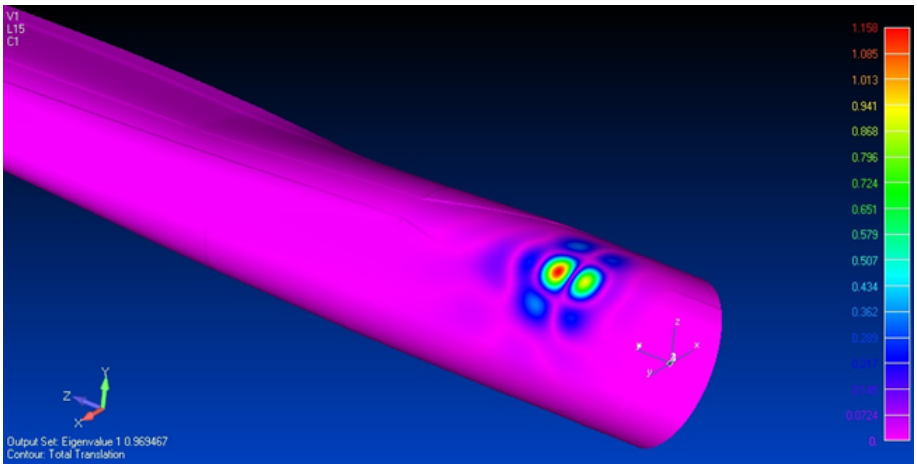

Figure 4.14: *Baseline 10 MW (C): Buckling waves due to ETM wind at 13 m/s.*

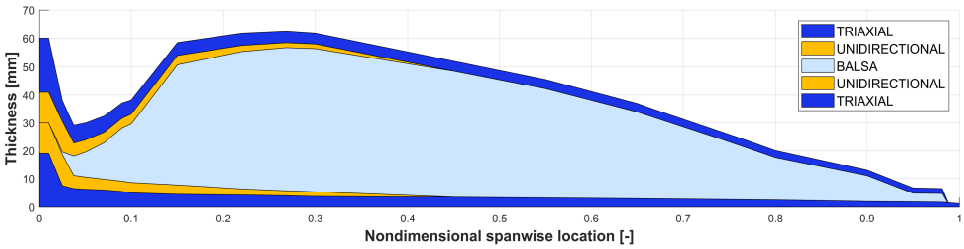

Figure 4.15: *Baseline 10 MW (C): lamination of the Shell TE SS panel.*

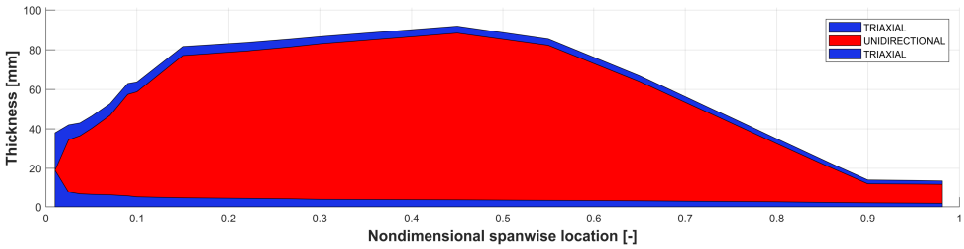

Figure 4.16: *Baseline 10 MW (C): lamination of the Spar PS panel.*

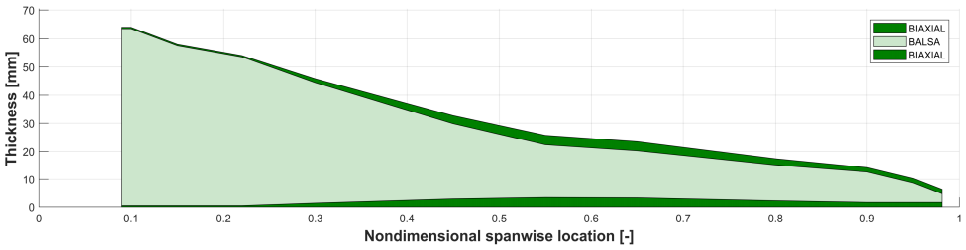

Figure 4.17: *Baseline 10 MW (C): lamination of the Web panel front.*

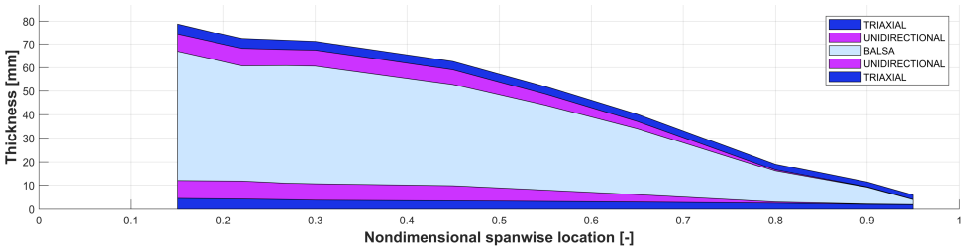

Figure 4.18: *Baseline 10 MW (C): lamination of the Reinforcement panel TE.*

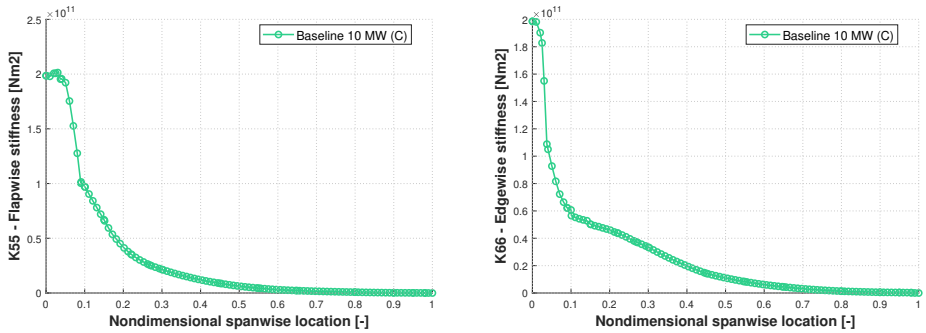

Figure 4.19: *Baseline 10 MW (C): flapwise (left) and edgewise (right) stiffness.*

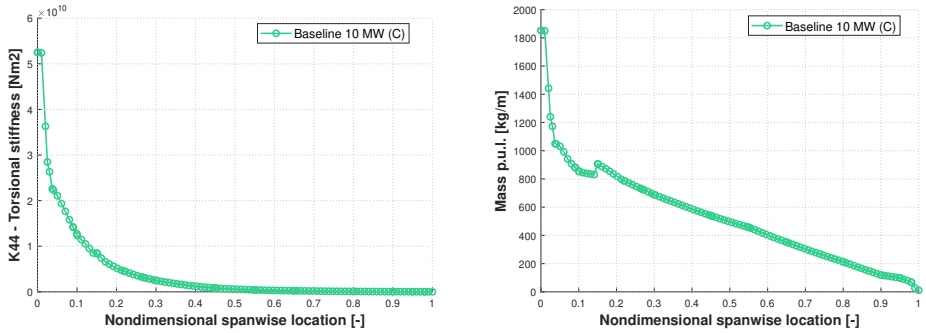

Figure 4.20: *Baseline 10 MW (C): torsional stiffness (left) and mass per unit length (right).*

Table 4.11: *Baseline 10 MW (C): KPI, ultimate and fatigue loads. BR is blade root, HC is hub center, TT is tower top and TB is tower base*

Baseline 10 MW (C)					
Performance		Ultimate loads		Fatigue DELs	
Frequency:	0.68 Hz	BR bending:	81.4 MNm	BR flapwise:	51.6 MNm
Displacement:	9.6 m	HC thrust:	3.24 MN	HC nodding:	44.5 MNm
Blade mass:	52620 kg	HC bending:	105.0 MNm	HC yawing :	39.4 MNm
AEP:	48.75 GWh	TT bending:	89.0 MNm	TT FA:	44.0 MNm
CoE:	73.67 €/MWh	TB bending:	899.1 MNm	TB FA:	140.3 MNm

4.4 Definition of the Baseline 20MW design

Our last baseline is a 20 MW rotor whose reference aero-elastic properties have been obtained by upscaling the INNWIND.EU reference [103]. We used these data to define an initial distribution of the structural components, and then, the SDS conducted a full structural optimization in accordance with the procedure described previously. The distribution of twist along the blade, together with the percent thickness, are given in Fig. 4.21. The sketch of the blade planform with the sectional elements is given in Fig. 4.22. It must be underlined that, in this case, the outstanding length of the blade required a very wide spar cap in certain parts of the blade, so that it was no longer possible to design a constant-width spar. The corresponding spar panels, then, are slightly tapered towards the tip of the blade. Again, the placement of the third web was established so that to reduce the onset of buckling in the most demanding loading conditions. The result of the optimization are given in Table 4.12, which shows the optimized thickness of the fabrics. The corresponding values of the core components are provided in Table 4.13.

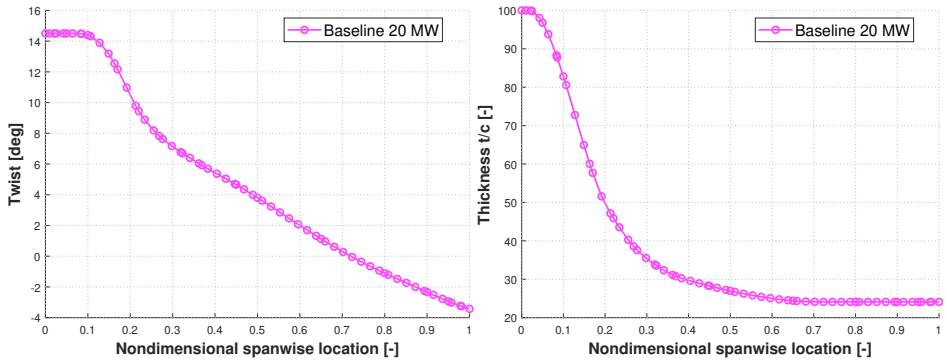

Figure 4.21: *Baseline 20 MW: spanwise twist (left) and percent thickness (right).*

The stacking sequence of some of the sectional elements is given in Figs. 4.23 to 4.26. In this case, the structural components have been laminated on the elements according to the Sequence B illsutrated in Table 4.1. The main difference is that the root reinforcement is no longer added to the sole shell panels, but it is laminated also along the spar panels (see

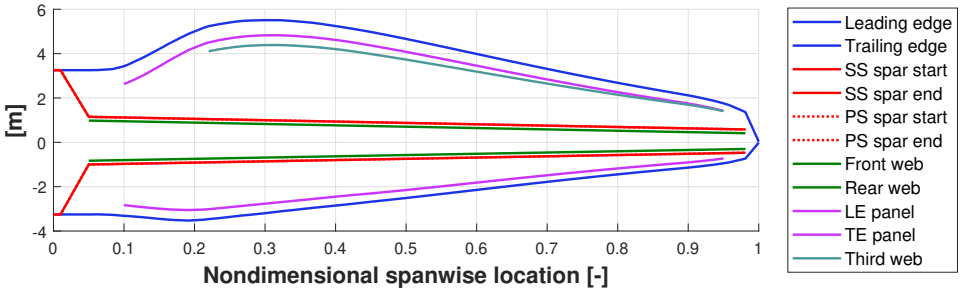

Figure 4.22: *Baseline 20 MW: blade planform and positioning of the sectional elements.*

for example Fig. 4.24) and along the reinforcement strips at LE and TE (see Fig. 4.26). The resulting structural properties are given in Fig. 4.27 that shows the flapwise (left) and edgewise (right) stiffness distributions, and by Fig. 4.28 which gives the torsional stiffness (left) and the mass per unit length (right). Again, Table 4.14 reports the main KPIs as they result from the SDS optimization.Those values will be used to establish a basis for comparison against the lightweight configuration designed in in Chapter 6.

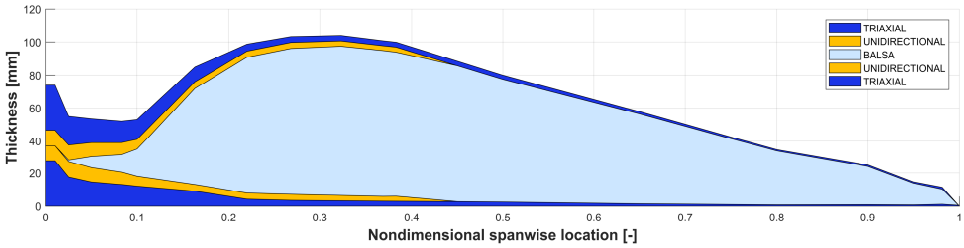

Figure 4.23: *Baseline 20 MW (C): lamination of the Shell TE SS panel.*

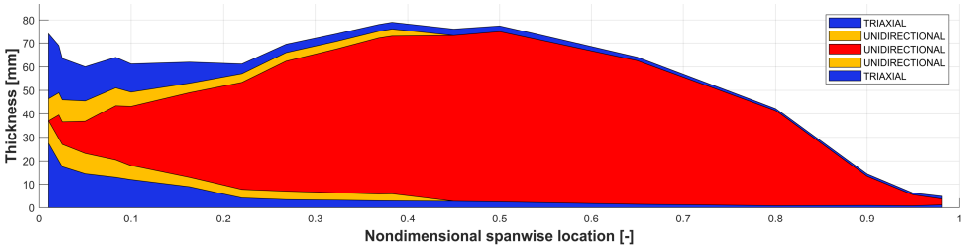

Figure 4.24: *Baseline 20 MW (C): lamination of the Spar SS panel.*

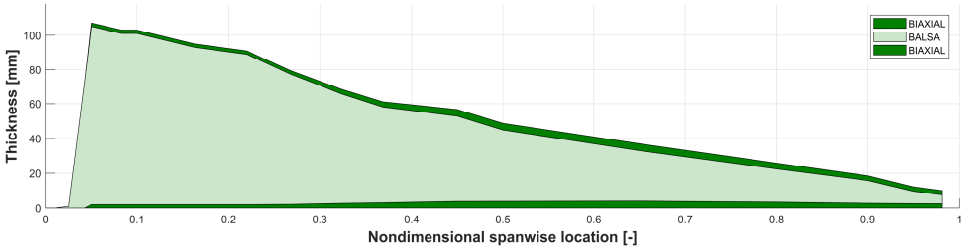

Figure 4.25: *Baseline 20 MW (C): lamination of the Web panel front.*

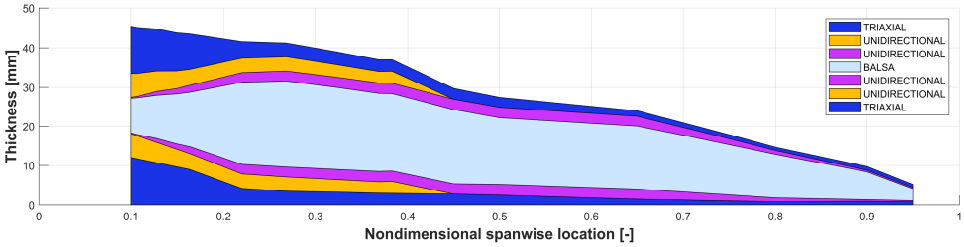

Figure 4.26: *Baseline 20 MW (C): lamination of the Reinforcement panel LE.*

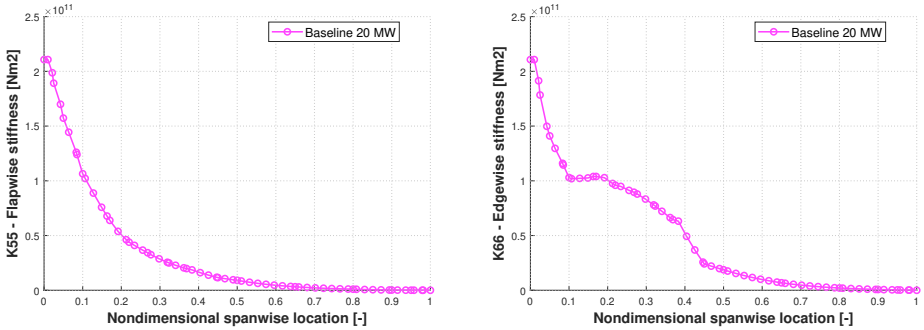

Figure 4.27: *Baseline 20 MW: flapwise (left) and edgewise (right) stiffness.*

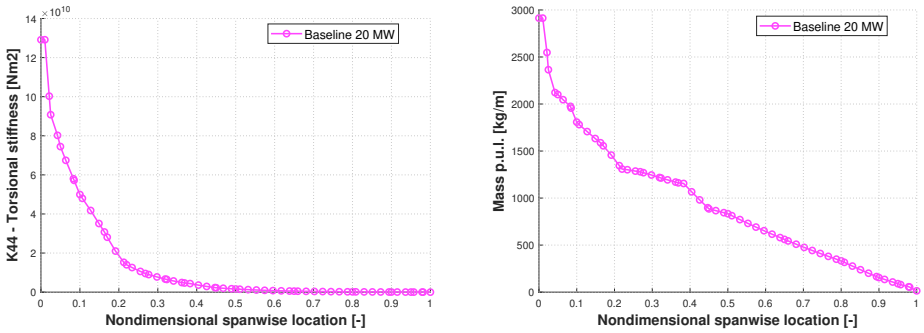

Figure 4.28: *Baseline 20 MW: torsional stiffness (left) and mass per unit length (right).*

4.5 Conclusions

In this Chapter, we employed the SDS sub-module of `Cp-Max` to conduct a structural definition of three different baseline rotors. Initially, we defined and optimized the internal structure of two 10 MW rotors, one based on glass and the the second on carbon. Then, we conducted a preliminary structural optimization of a 20 MW rotor, based on glass. The main goal was to develop reference configurations which will be used in the next Chapters to conduct specific design studies about lightweight rotors. To this end, it is paramount that the baseline rotors are initially designed with the same algorithms and methods we use later: this to make sure that a KPI-based comparison is meaningful and that the compared solutions come from the same design process. Additionally, the solutions presented in this Chapter could serve as a reference basis for further design studies or to conduct validations of structural design tools.

Table 4.12: *Baseline 20 MW: spanwise optimal values of the structural components (fabrics)*

	Component thickness [mm]											
η	$t_{shell}^{TE,SS}$	$t_{shell}^{LE,SS}$	$t_{shell}^{TE,PS}$	$t_{shell}^{LE,PS}$	t_{spar}^{SS}	t_{spar}^{PS}	t_{webs}^{front}	t_{webs}^{rear}	t_{3web}	t_{strip}^{LE}	t_{strip}^{TE}	t_{rr}
0.000	55.00	55.00	55.00	55.00	-	-	-	-	-	-	-	19.00
0.010	55.00	55.00	55.00	55.00	-	-	-	-	-	-	-	19.00
0.025	35.00	35.00	35.00	35.00	9.55	4.14	0.00	0.00	-	-	-	19.00
0.050	29.00	29.00	29.00	29.00	13.57	13.86	4.00	4.00	-	-	-	17.50
0.083	26.00	26.00	26.00	26.00	23.04	23.24	4.00	4.00	-	-	-	15.00
0.100	24.00	24.00	24.00	24.00	25.27	26.75	4.00	4.00	-	0.50	0.70	12.00
0.163	18.00	18.00	18.00	18.00	36.02	37.93	4.00	4.00	-	3.54	4.26	8.00
0.220	8.40	8.40	8.40	8.40	45.52	48.40	4.00	4.00	6.79	4.86	5.37	7.31
0.268	7.00	7.00	7.00	7.00	55.31	59.37	4.33	4.33	6.84	5.02	5.50	7.19
0.323	6.50	6.50	6.50	6.50	61.11	65.50	5.43	5.43	6.87	5.14	5.61	6.36
0.369	6.00	6.00	6.00	6.00	66.33	72.41	6.09	6.09	6.88	5.26	5.64	5.75
0.450	5.51	5.51	5.51	5.51	70.56	74.94	7.67	7.67	6.83	5.23	5.57	-
0.500	5.00	5.00	5.00	5.00	72.45	78.99	7.73	7.73	6.82	5.47	5.09	-
0.650	2.93	2.93	2.93	2.93	61.18	62.18	8.00	8.00	6.70	5.16	3.82	-
0.800	1.65	1.65	1.65	1.65	40.65	44.68	6.82	6.82	6.78	1.95	2.65	-
0.900	1.90	1.90	1.90	1.90	12.49	13.60	5.51	5.51	6.82	0.82	1.20	-
0.950	1.60	1.60	1.60	1.60	4.76	4.94	5.16	5.16	6.81	0.62	0.75	-
0.981	2.35	2.35	2.35	2.35	2.57	3.59	5.00	5.00	-	-	-	-
1.000	1.00	1.00	1.00	1.00	-	-	-	-	-	-	-	-

Table 4.13: *Baseline 20 MW: spanwise optimal values of the structural components (fillers)*

	Component thickness [mm]						
η	$t^{TE,SS}_{shell,core}$	$t^{LE,SS}_{shell,core}$	$t^{LE,PS}_{shell,core}$	$t^{TE,PS}_{shell,core}$	$t^{front}_{webs,core}$	$t^{rear}_{webs,core}$	$t_{3web,core}$
0.000	-	-	-	-	-	-	-
0.010	-	-	-	-	-	-	-
0.025	1.00	1.00	1.00	1.00	1.00	1.00	-
0.050	7.00	5.00	5.00	5.00	103.00	93.00	-
0.083	11.00	7.00	7.00	11.00	99.00	85.00	-
0.100	17.00	9.00	9.00	19.00	99.00	85.00	-
0.163	59.00	13.00	15.00	77.00	91.00	71.00	-
0.220	83.00	21.00	21.00	53.00	87.00	65.00	15.00
0.268	89.00	21.00	23.00	67.00	75.00	61.00	11.00
0.323	91.00	21.00	21.00	75.00	63.00	53.00	7.00
0.369	89.00	19.00	21.00	73.00	55.00	49.00	5.00
0.450	83.00	19.00	19.00	71.00	49.00	41.00	3.00
0.500	75.00	17.00	17.00	63.00	41.00	37.00	3.00
0.650	55.00	15.00	17.00	47.00	29.00	25.00	1.00
0.800	33.00	11.00	11.00	25.00	19.00	15.00	1.00
0.900	23.00	7.00	7.00	15.00	13.00	11.00	1.00
0.950	13.00	3.00	3.00	7.00	7.00	5.00	1.00
0.981	9.00	1.00	1.00	5.00	5.00	3.00	-
1.000	-	-	-	-	-	-	-

Table 4.14: *Baseline 20 MW: KPI, ultimate and fatigue loads. BR is blade root, HC is hub center, TT is tower top and TB is tower base*

Baseline 20 MW					
Performance		Ultimate loads		Fatigue DELs	
Frequency:	0.45 Hz	BR bending:	172.8 MNm	BR flapwise:	83.8 MNm
Displacement:	15.0 m	HC thrust:	5.7 MN	HC nodding:	53.5 MNm
Blade mass:	113.5 ton	HC bending:	112.9 MNm	HC yawing :	49.9 MNm
AEP:	91.62 GWh	TT bending:	105.0 MNm	TT FA:	53.4 MNm
CoE:	84.97 €/MWh	TB bending:	1480 MNm	TB FA:	278.5 MNm

CHAPTER 5

Integration of passive load alleviation techniques on large rotors

In this Chapter, we investigate the possibility to embed different layers of structural tailoring within the design of our 10 MW baseline rotors. The ultimate scope is the reduction of the driving loads on the turbine and, possibly, the design of lighter blades. Structural tailoring embraces a set of techniques which purposely exploit the anisotropy of the composite materials used in the lamination of the blade to trigger certain aero-elastic mechanisms which typically reduce the loads along the blade. In this view, built-in structural tailoring can be included in the family of passive control strategies. The idea behind the design process is to investigate different techniques separately and then to combine them in a unique solution. Our first topic discusses how the introduction of a certain fiber angle in the stacking sequence of an element can modify the stiffness matrix of the section and create a relation between the deflection of the blade and its torsional deformation. By properly tuning the fiber orientation, it is possible to exploit the induced torsion to automatically reduce the angle of attack of the section. We conduct a preliminary assessment of such technique on both the 10 MW (G) and the 10 MW (C) references, then, we exploit the beneficial effects on the loads to design lightweight versions of both rotors. We'll see how the design concept of the baseline, whether highly-efficient or low-induction, influences the evolution of the lightweight solutions. A second study focuses on topological bend/twist coupling. It is shown how the introduction of a geometric offset between the two spar caps further modifies the stiffness matrix, and ultimately originates a coupling similar to that achieved by fiber rotation. It is shown that, depending on the rotor design, this technique can work along with the previous one or not. Finally, we apply a fiber orientation to the laminae of the shear webs: this introduces a relation between the in-plane edgewise deflection of the blade and its torsional deformation. We show that, depending on the edgewise deformation

of the blade, this technique can provide a further load alleviation. Since the focus of this study lies on the structural design of large rotors, during the investigation all the solutions have been recursively redesigned through the SDS module of `Cp-Max`. Although quite time-consuming, this choice allows a consistent comparison of different rotors, mainly because all of them are designed for the same set of loads and are bounded by the same constraints. However, given that the focus is on the demonstration of the lightweight concept, we limited the analysis to the sole coarse/aero-elastic loop of the SDS, thus saving the computational effort usually required by a full FEM verification. Naturally, this implies that the resulting solutions are not fully-feasible in a strict term, however, all the baseline rotors have been verified through FEM and we judged that the wide set of DLC used for the design should grant a sufficient accuracy in the structural optimization.

5.1 Fiber-induced structural coupling

The possibility to introduce a coupling between the flapwise deflection of the blade and its torsional deformation through a certain rotation of the material fibers has been largely investigated in the literature. The theoretical foundations were posed by Lobitz and Veers [105, 106], who also observed the induced torsion through dedicated experiments. Later, Cox and Echtermeyer [107] applied the concept to increasing blade lengths to assess a possible correlation between the amount of BTC and the upscaling of rotors. Recently, several researchers have studied the integration of the technique within optimization procedure: Bottasso et al. [108] performed a sequence of parametric studies to demonstrate the load mitigating effect on a 2 MW rotor, while Vesel and McNamara conducted a full redesign of the NREL 5 MW wind turbine [109]. A similar procedure has been applied, on a much smaller rotor, by McWilliam et al. [110].

In this Section, we integrate the fiber-induced BTC, hereafter referred as F-BTC, in the structural definition of our glass and carbon 10 MW rotors, to investigate the resulting aeroelastic coupling in the context of a high-fidelity structural design. Initially, we demonstrate the working principle of the concept through simplified test cases of increasing complexity. Then, we conduct a parametric analysis in which both rotors are completely redesigned for varying angles of fiber misalignment, showing that there is a potential for a significant reduction of the main load components. Eventually, we design two lightweight configurations for our baselines in which the load mitigation is exploited in different ways to improve the KPIs of the turbine.

5.1.1 Characterization of the F-BTC mechanism

The working principle of the F-BTC is based on the fact that the composite fabrics employed in the manufacture of the blade have a certain level of embedded anisotropy, which is engineered to maximize the performance of the laminate in certain directions. In the case of an unidirectional laminate, for example, the build-up of the material aims at achieving the maximum strength and stiffness in the direction of the laminate axis. In a typical scenario, the orientation of the various layers of material is chosen as to match the longitudinal axis of the section, so that the fibers can maximize their efficiency when the blade is loaded. In this case, the value of the diagonal terms of the stiffness matrix depends largely on the preferred direction of the fibers, while extra-diagonal terms are null, or very small. However, if a certain rotation is introduced during the lamination of the fibers, the value of the

extra-diagonal stiffness terms are modified and a coupling is introduced in the response of the blade.

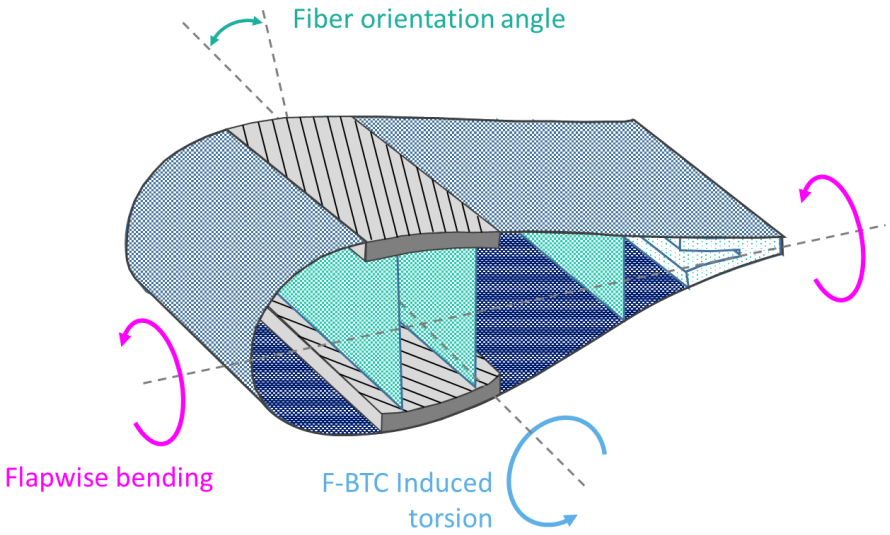

Figure 5.1: *Qualitative description of the F-BTC mechanism.*

Figure. 5.1 shows a qualitative sketch of the F-BTC concept applied to the fibers of the spar caps: by rotating the fibers away from the sectional axis, a coupling between the flapwise deflection and the torsional deformation of the section is established. When loaded, then, the section will automatically twist in a direction which depends on whether the fibers are rotated towards the leading or the trailing edge. If the rotation is suitably chosen, the induced twist occurs in the direction of the wind, so that the angle of attack of the section is automatically reduced, with the ultimate effect of reducing the loads.

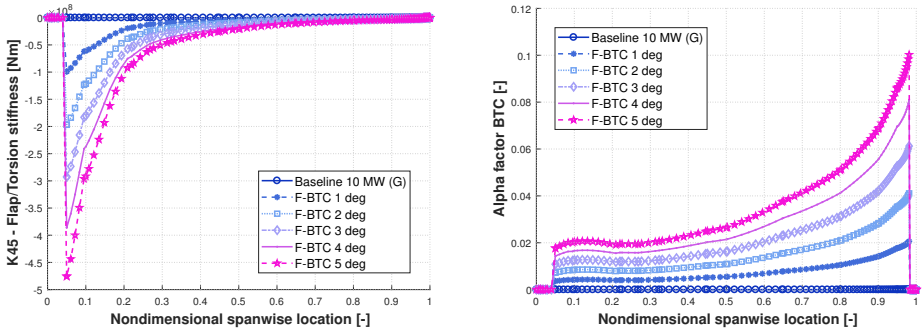

Figure 5.2: *Spanwise flap/torsion stiffness (left) and α_{BTC} factor (right) for varying fiber orientations.*

To quantify this effect, we conducted a parametric analysis in which an increasing amount of fiber orientation was applied to the spar caps of the **Baseline 10 MW (G)** designed in § 4.2. The corresponding distribution of the extra-diagonal stiffness K_{45} relating flapwise

bending and torsion is given in Fig. 5.2 (left): while this term is null for the baseline design, it grows depending on the amount of fiber orientation. It must be noticed that no structural redesign has been done at this step: the fibers are parametrically rotated for a given structure, so that the different behaviours can be only ascribable to the F-BTC mechanism. Since the magnitude of the coupling stiffness depends on the properties of the material and it is sometimes hard to assess, according to Lobitz and Veer [105], it is possible to define a non-dimensional coupling factor as follows:

$$\alpha_{BTC} = |\frac{K_{45}}{\sqrt{K_{55}K_{44}}}| \tag{5.1}$$

where K_{45} is the BTC term of the stiffness matrix, K_{55} is the flapwise stiffness and K_{44} the torsional stiffness term. All the stiffness components are expressed in a local frame within `Cp-Lambda` so they represent purely-sectional quantities that do not depend on the local twist, sweep or prebend. The spanwise value of the coupling factor is given for the parametric F-BTC solutions in Fig. 5.2 (right), and confirms that a stronger coupling can be achieved through a higher fiber orientation.

5.1.2 Application to simplified test cases

The parametric stiffness analysis demonstrates the correlation between an orientation of the fibers of the spar caps and the F-BTC mechanism. To understand the potential benefits at design level, however, it is necessary to characterize the response of the coupled blade when it is subjected to loads, specifically to check if the coupling is strong enough to modify substantially the torsional deformation of the blade. We tested the parametric F-BTC solutions through three simplified test cases, in which the blade is simulated with increasing levels of detail. The outcomes of the simplified tests, all run by `Cp-Lambda`, are briefly summarized in the following.

Test case 0: Clamped blade with dead load In the first test case, a single blade is clamped at the root and subjected to an out-of-plane concentrated force at tip. The force is a follower load, which means that it follows the deformation of the blade at any time step. A schematic view of the simulation layout is given in Fig. 5.3. The blade is simulated *in vacuo* with no gravity field applied and no aerodynamics. Then, the blade is deformed by the sole action of the tip load.
In this case, it is not possible to evaluate the F-BTC on the flapwise bending at root. In fact, since the bending is externally applied through the dead load, its value is identical for all the solutions. However, the F-BTC is visible when looking at the deformations. Figure 5.4 gives the spanwise distribution of the out-of-plane (OOP) deflection: although the differences are small, given the over-simplified loading condition, it is clearly seen that the displacement is higher in the coupled blades. This is a consequence of the reduction of the flapwise stiffness K_{55} associated to the rotation of the fibers.
Figure 5.5 shows the spanwise torsion of the blade which is, as expected, much higher as the fiber are rotated away from the sectional axis. It must be noticed that, in this frame, a negative value of the twist implies a nose-in-the-wind rotation of the section.

Test case 1: Blade as a wing In this case, a single blade is posed in a steady, uniform wind speed of 42 m/s. Since the blade is non rotating, there is no inflow modelling and the aerodynamic loads are directly computed from the wind field impinging on the lifting

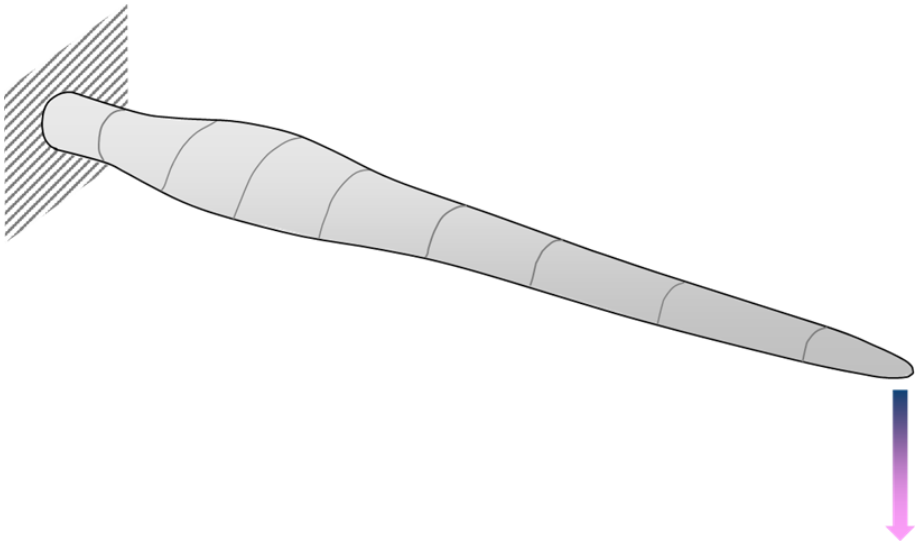

Figure 5.3: *Definition of test case 0.*

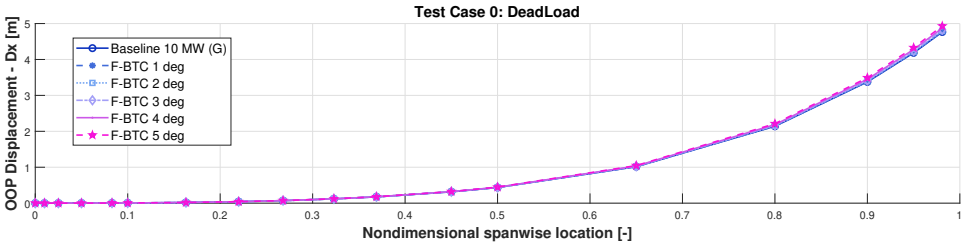

Figure 5.4: *Test case 0 with F-BTC: out-of-plane deflection.*

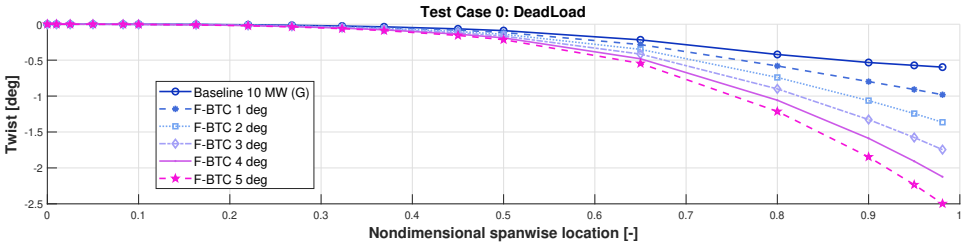

Figure 5.5: *Test case 0 with F-BTC: torsional deformation.*

line, according to a strip theory model. Gravity is not modelled. The blade is mounted on a revolute joint which allows to manually modify the pitch angle β and thus the relative orientation of the blade with respect to the incoming wind. The bottom face of the revolute joint is clamped. Figure 5.6 shows a simplified view of the model.
A set of dynamic simulations has been run on all the F-BTC simulations for varying pitch angles. Figure 5.7 shows a close-up of the flapwise bending at root achieved for the condition $\beta = 80°$, which is a fair approximation of the real angles of attack of the blade in operation. Although the variations are small, it is clearly visible how the flap load is re-

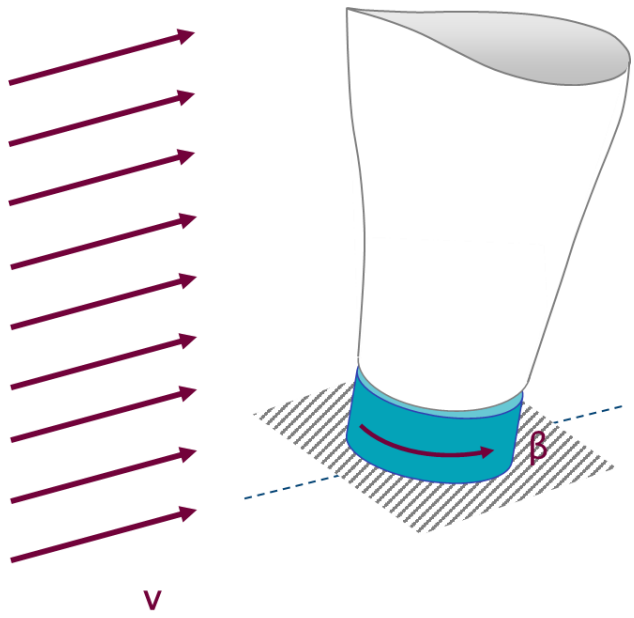

Figure 5.6: *Definition of test case 1.*

duced when F-BTC is introduced in the structure. Similarly, Fig. 5.8 shows the twist and, again, the effect of the F-BTC on the torsional deformation of the blade is clear.

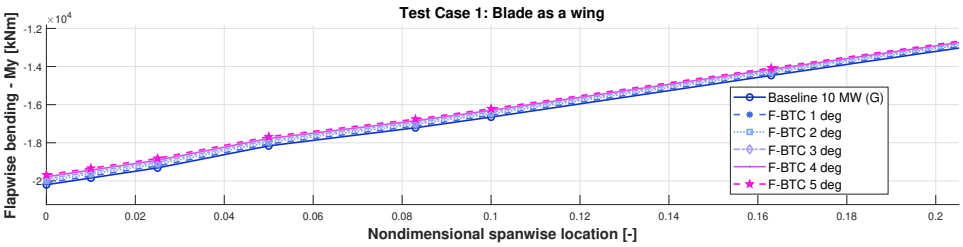

Figure 5.7: *Test case 1 with F-BTC: flapwise bending at root.*

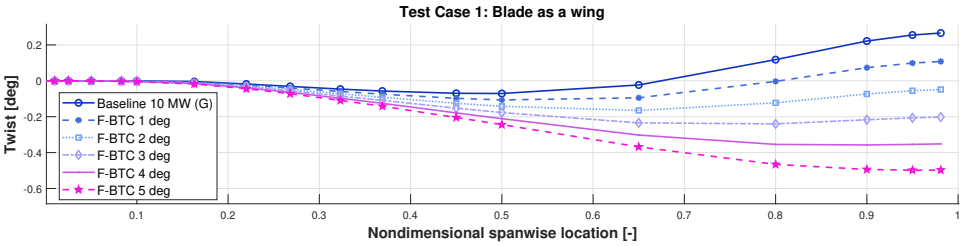

Figure 5.8: *Test case 1 with F-BTC: torsional deformation.*

Test case 2: Single blade rotating The third case represents an approximation of the operating conditions of the rotor. A single blade is rotating at the rated rotor speed, with a uniform wind speed equal to the rated speed of the turbine. Again, a revolute joint at the root of the blade allows to control the relative orientation of the blade with respect to the incoming wind. The aerodynamic model is active and based on the BEM inflow model, so that the induction factors can be properly computed. The results presented in this paragraph refer to a condition when the blade pitch is imposed and equal to zero: this condition is chosen to approximate the actual collective pitch at nominal conditions. Figure 5.9 gives a sketch of the model.

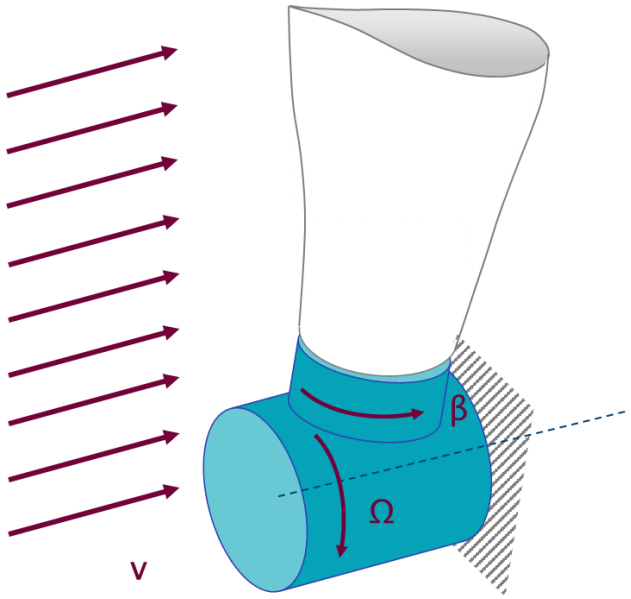

Figure 5.9: *Definition of test case 2.*

The load-alleviating mechanism of the F-BTC is widely confirmed by simulations of test case 2. Figure 5.10 shows a close-up of the lift coefficient, magnified towards the tip of the blade: as expected, the induced torsion associated to the rotation of the fibers results in an automatic reduction of the angle of attack, which globally reduces the generated lift. In turn, this causes a reduction of the flapwise bending, as shown in Fig. 5.11, which magnifies the flap loading towards the blade root. Figure 5.12 shows the sectional torsion, which is increased according to the amount of fiber rotation. A similar qualitative behaviour was observed when the F-BTC was applied to the carbon-based baseline rotor developed in § 4.3.

5.1.3 Parametric structural redesign with F-BTC

The verification of the F-BTC through the simplified test cases shows potential for load mitigation when applied to our 10 MW rotors. However, to properly assess the effects of this technique on the performance of the turbine, it is necessary to study the F-BTC at a design level. To do this, we conducted a parametric structural redesign for both 10 MW baseline rotors: in this analysis, we compare several solutions equipped with varying degrees of fiber orientation. For each solution, the internal structure is completely redesigned

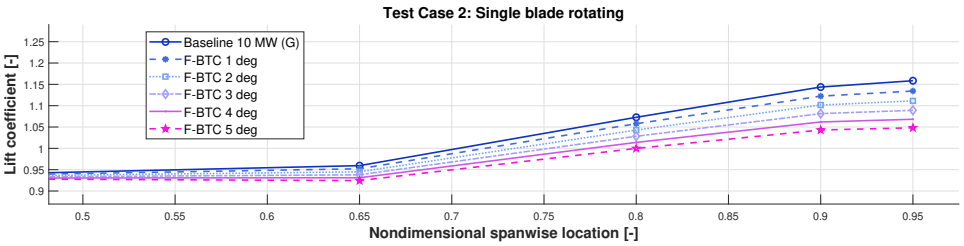

Figure 5.10: *Test case 2 with F-BTC: lift coefficient.*

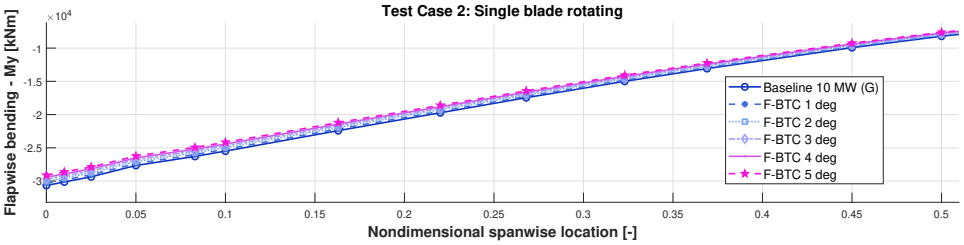

Figure 5.11: *Test case 2 with F-BTC: blade root flapwise bending.*

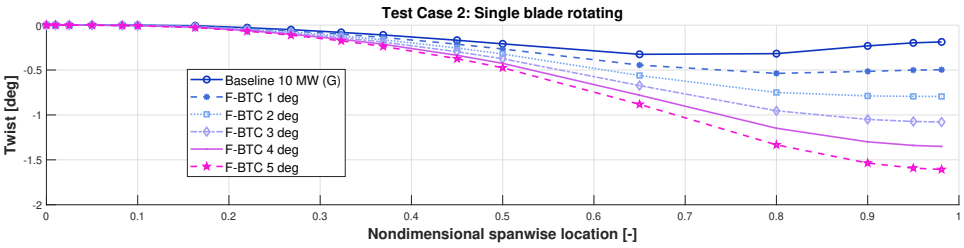

Figure 5.12: *Test case 2 with F-BTC: torsional deformations.*

with the SDS module of `Cp-Max` for the same set of DLC employed for the design of the baseline. Then, we evaluate the trends of the main loads, in particular those related to fatigue, and those of selected KPIs of the turbine, specifically the turbulent AEP, the total blade mass and the cost of energy. We conducted a first parametric analysis on the Baseline 10 MW (G) rotor with fiber orientations progressively increased from 3 to 7 degrees, as this interval allows to uniquely identify an optimal solutions with respect to the cost of energy. Figure 5.13 shows the percent variation of selected fatigue Damage Equivalent Loads (DEL) along the turbine for all the redesigned configurations. Here *BRflp* represents the flapwise equivalent load at blade root, *HCnod* is the nodding load at the hub center while *TTFA* and *TBFA* are the fore-aft fatigue loads at the tower top and tower base. It emerges that all the F-BTC solutions succeed in reducing the load components on the whole turbine, and the recursive redesign of the structure allows a consistent comparison of the solutions, in particular because the wide set of DLC considered during the design provides a wide spectra of operating conditions along which the impact of the load mitigation technique is thoroughly accounted for.
Figure 5.14 shows the percent variation of chosen KPIs (namely the blade mass, AEP and COE) compared against the Baseline 10 MW (G): as expected, one main achievement

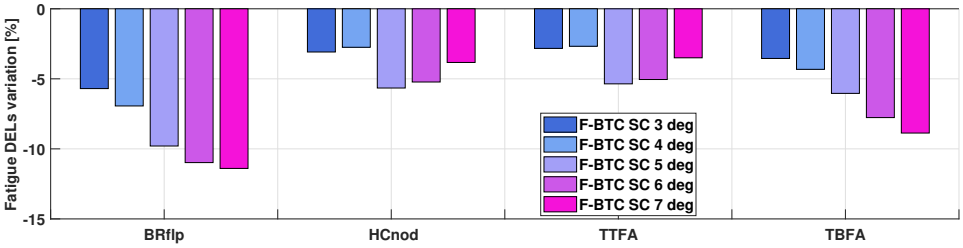

Figure 5.13: *Parametric F-BTC redesign: percent variation of the DEL against the Baseline 10 MW (G) rotor.*

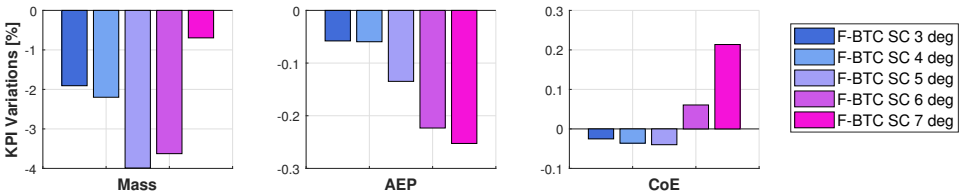

Figure 5.14: *Parametric F-BTC redesign: percent variation of the KPIs against the Baseline 10 MW (G) rotor.*

of the F-BTC solutions is a consistent reduction of the blade mass. This is in part due to the lower loads which consequently reduce the ultimate displacement, and in part to the reduction of fatigue loads which results in a lighter design of some components, specifically the shell and the shear webs. However, a known drawback of this mechanism is a reduction of the energy capture: this effect, which is stronger for larger fiber rotations, is related to the larger torsional deformations which drive away the sections from their point of maximum efficiency. The combination of these effects on the COE is mild, as the cost savings from lighter blades are compensated by the drop in the AEP, however, when the fiber rotation becomes larger the energy drop becomes significant and the COE actually increases. It is important to notice that conceptually it is possible to induce some amount of BTC through a rotation of the fibers in the shell, and in some cases the simultaneous rotation of the shell and the spar cap fibers can show advantages when compared against a pure rotation of the spar cap fibers. However, there was no evidence of such beneficial effect in the rotor under investigation. In our opinion, the poor correlation between the shell rotation and the BTC effect depends on the low amount of anisotropy of the triaxial texture, which makes difficult to exploit the intrinsic anisotropy of the material to induce BTC. A similar parametric analysis, performed on the **Baseline 10 MW (C)** carbon rotor, gave similar qualitative results.

5.1.4 Lightweight redesign with F-BTC

Lightweight glass design

The parametric redesign analysis conducted for both baseline rotors showed a potential for significant load alleviation when the F-BTC is applied to the structure of the blades. However, a direct comparison of the KPIs shows that, although the load mitigation can result in a reduction of the blade mass, a typical by-product is the reduction in the energy capture. Then, unless some strategy is undertaken in order to restore or possibly increase the AEP

of the baseline, the introduction of the F-BTC has only limited economic advantages. At this stage, then, we used the Macro Design Loop of `Cp-Max` to design lightweight rotors with embedded F-BTC. A first configuration was derived from the glass 10 MW baseline: a fiber rotation of 5 degrees was introduced in the structural definition of the spar caps, since this configuration is the one giving the largest advantages in the parametric structural redesign. Then, the code was used to optimize the rotor diameter for a given set of target loads. Then, in this case the load reduction given by the F-BTC was exploited to design a larger rotor and increase the AEP. Since we didn't expect dramatic variations of the radius, the aerodynamic shape of the rotor, including the solidity and the other shape parameters at macro-level were not redesigned. Conversely, the structural design was always re-optimized to ensure consistency. The MDL was operated under the requirement that the loads transmitted by the optimal rotor on the fixed infrastructure should not exceed the 105% of those of the baseline. This was formalized by introducing constraints on the loads at the hub and and the tower top/base. We judged, in fact, that a 5% increase of some of the loads is acceptable without a dedicated redesign of the hub and the tower. The loads on the rotor, on the contrary are basically unconstrained, because the SDS module of `Cp-Max` automatically produces solutions which fulfil the structural constraints coming from the updated loads. The resulting rotor, hereafter called **LW 10 MW (G) F-BTC** where LW identifies a relatively *lightweight* solution, has a rotor diameter of 185m, that is, the introduction of the F-BTC allows to design a 3.9% wider rotor.

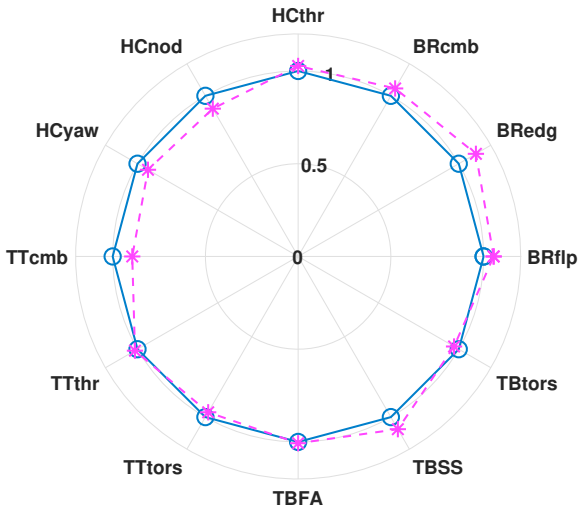

Figure 5.15: *Comparison between the ultimate loads of the Baseline 10 MW (G) wind turbine (solid blue line) and the LW 10 MW (G) F-BTC (pink dashed line).*

Figure 5.15 provides a comparison of the ultimate loads between the redesigned lightweight rotor, represented by the pink dashed line and the Baseline 10 MW (G) (solid blue). Here, *BR* is the blade root, *HC* is the hub center, *TT* and *TB* are the tower top and the tower base. The load components are given in terms of flapwise (flp), edgewise (edg), combined/multidirectional (cmb), torsion (tors), thrust (thr), fore-aft (FA) and side-side (SS). Figure 5.16 provides a similar comparison between the most important fatigue loads along the turbine. It is immediate to show that the rotor sizing is actively constrained by fatigue loads at the hub and the tower top, while both ultimate and fatigue loads at the tower base are comparable against the two solutions. This is a remarkable result, as it states

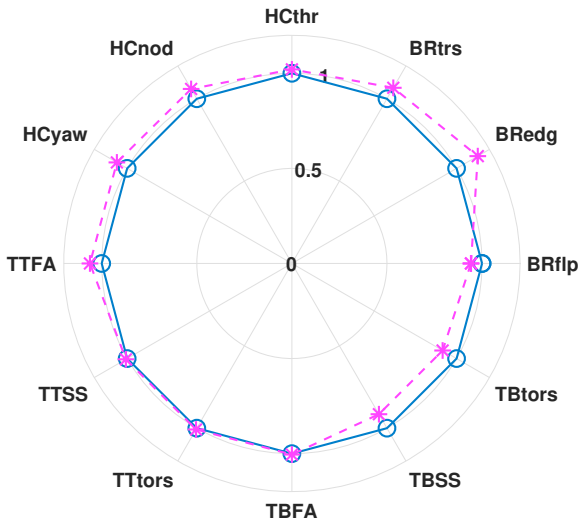

Figure 5.16: *Comparison between the fatigue loads of the Baseline 10 MW (G) wind turbine (solid blue line) and the LW 10 MW (G) F-BTC (pink dashed line).*

Table 5.1: *Comparison between the KPIs of the Baseline 10 MW (G) wind turbine and the LW 10 MW (G) F-BTC.*

Performance	Baseline 10 MW (G)	LW 10 MW (G) F-BTC	Variation
Blade mass:	42574 kg	46335 kg	+8.83%
AEP:	46.4 GWh	47.3 GWh	+2.00%
CoE:	74.93 €/MWh	74.03 €/MWh:	-1.19%

that both rotor could equip the same wind turbine without the need to redesign the tower. Ultimate loads on the blades are slightly higher for the lightweight rotor, in particular the edgewise bending which largely depends on the blade mass. The fatigue in the flapwise direction, however, is reduced. Table 5.1 summarizes the KPIs of both rotors: as expected the increase in the diameter led to a higher blade mass, however, the larger rotor surface allows a 2% higher energy capture and it overall reduces the COE of about 1.2%. We conclude, in this case, that the introduction of the F-BTC opens the possibility of designing larger rotors with the same loading system of the baseline.

Lightweight carbon design

We conducted a second redesign on the carbon baseline. Although the design implications of the F-BTC are similar to the previous case, we followed a different strategy to restore the AEP of the original rotor. In fact, considering that the Baseline 10 MW (C) is based on the low-induction concept, the collective pitch in the partial-loading region is chosen as to limit the efficiency, and thus the loading, of the rotor. Then, with this configuration it is possible to restore the energy production by re-tuning the collective pitch β_{min}. In this application we set a fiber rotation of 5 degrees as we did in the glass case. The MDL, however, was used to optimize the collective minimum pitch instead of the rotor diameter.

Table 5.2: *Comparison between the KPIs of the Baseline 10 MW (C) wind turbine and the LW 10 MW (C) F-BTC.*

Performance	Baseline 10 MW (C)	LW 10 MW (C) F-BTC	Variation
Blade mass:	52621 kg	52023 kg	-1.13%
AEP:	48.7 GWh	48.9 GWh	+0.41%
CoE:	73.67 €/MWh	73.34 €/MWh:	-0.44%

This time all the loads, including those of the blades, were constrained not to exceed a 5% threshold from those of the baseline. The resulting optimal rotor reduces the collective minimum pitch form 0 to -2 degrees. Figure 5.17 compares the ultimate loads of the redesigned rotor, here called LW 10 MW (C) F-BTC, against those of the carbon baseline, A similar comparison of fatigue DELs is given in Fig. 5.18. Unsurprisingly, the limiting loads is the torsion at the blade root, whose fatigue equivalent load increased due to the introduction of the F-BTC. However, most ultimate and fatigue loads achieve significant reductions. Table 5.2 shows a comparison of the KPIs: quite interestingly, the blade mass is not significantly reduced: this is a consequence of the fact that the carbon spar caps are sized by ultimate stress. These ultimately depends on the ultimate combined bending, which is only modestly reduced by the introduction of the F-BTC. The AEP is increased as a consequence of the re-tuning of the collective minimum pitch. The combination of these factors leads to a 0.4% reduction of the COE. However, since the rotor diameter has been maintained, the main effect of the F-BTC is a consistent reduction of the driving loads. The important alleviation at the hub and at the tower base could possibly imply a lighter redesign of these components, giving additional contributions to the reduction of the COE.

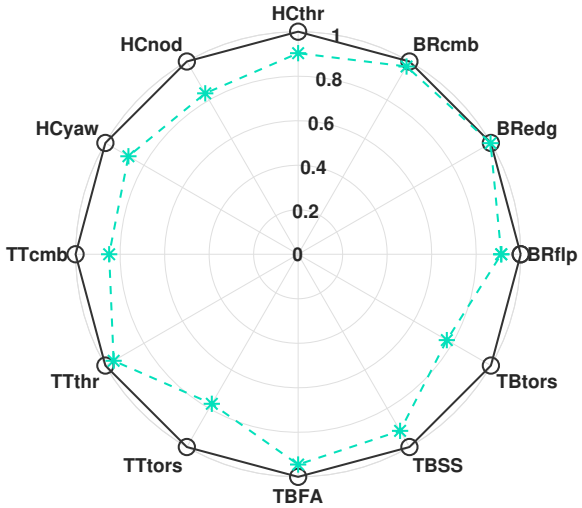

Figure 5.17: *Comparison between the ultimate loads of the Baseline 10 MW (C) wind turbine (solid black line) and the LW 10 MW (C) F-BTC (acquamarine line).*

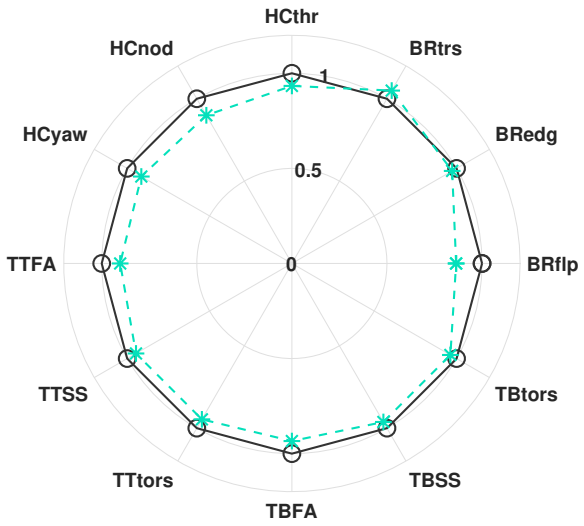

Figure 5.18: *Comparison between the fatigue loads of the Baseline 10 MW (C) wind turbine (solid black line) and the LW 10 MW (C) F-BTC (acquamarine line).*

5.2 Load alleviation through topological tailoring

A second approach to passive load mitigation is based on the idea of changing the topology of the blade section to achieve a desired level of coupling. The idea of introducing an offset between the suction-side and the pressure-side spar caps was first proposed by Pirrera et al. [111], who achieved this layout as the solution of a topology optimization problem. Later, Buckney et al. [112, 113] provided a preliminary characterization of the resulting coupling mechanism, showing how an offset topology alleviates the multi-directional flap/edge bending. The Authors also hinted the possibility of exploiting the particular behaviour to induce bend/twist coupling in the blade, a concept which is explored in this Section. Preliminary investigations of the offset concept to achieve BTC where conducted in parallel by Zahle et al. (see [114] pp. 27-38) and by Croce et al. [115] in the context of the INNWIND.EU research project, while recently Capuzzi et al. [116, 117] proposed a combination of fiber-induced and topology-induced load alleviation, although the latter is based on the back-sweeping of the blade rather than the spar offset. Nevertheless, their work shows results which are consistent with those presented later on in this Section.

Figure 5.19 shows the basic functioning of this mechanism, hereafter referred as O-BTC to differentiate it from the one based on the fiber orientation. The two spar caps, which are typically defined at the same chord-wise position, are shifted in opposite directions, with the total achievable offset depending on the available space between the shear webs. To highlight the mechanism, we conducted a parametric stiffness analysis similar to that discussed in § 5.1. We just started from the structural design of the Baseline 10 MW (G) and progressively introduced an offset between the spar caps. Offset of 10, 20 and 30cm were tested, with a uniform shift applied along the entire monolithic part of the spar caps. As it can be seen in Fig. 5.20 (left), the main effect of this arrangement is the modification of the extra-diagonal stiffness term which couples the flapwise and the edgewise response

of the blade. Unlike the case of the F-BTC, this term is typically non-zero, as some degree of flap/edge coupling is introduced by the curved surface of the blade. However, it is clear form the Figure that increasing the offset leads to an increase, in magnitude, of the coupling term. Similar findings where presented by Buckney et al. [113, 118], who also defined suitable shape factors to study the strength of the coupling term. In the context of this work, to encourage a direct comparison between different mechanisms, we define a non-dimensional sectional parameter similar to that of Eq. 5.1:

$$\alpha_{FEC} = \frac{K_{56}}{\sqrt{K_{55}K_{66}}} \tag{5.2}$$

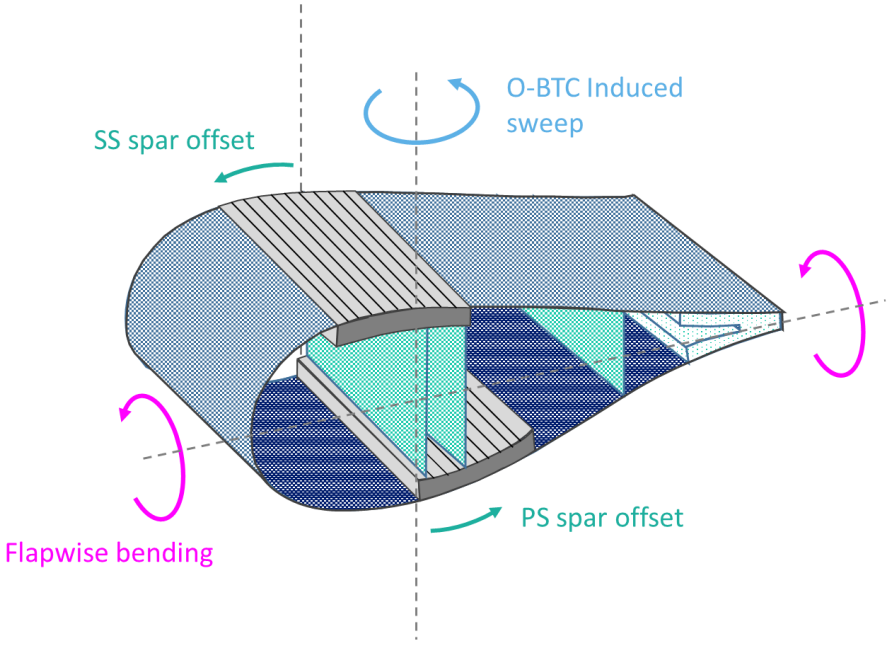

Figure 5.19: *Qualitative description of the O-BTC mechanism.*

in which K_{56} is the flap/edge extra-diagonal term, K_{55} is the flapwise bending stiffness and K_{66} the edgewise contribution. The spanwise distribution of α_{FEC} is given for the various values of the offset in Fig 5.20 (right) and shows that, like the case of the F-BTC, a wider offset between the caps gives a stronger coupling. The influence of the O-BTC on the response of the blade is quite different from the one triggered by the fiber orientation. The higher contribution of the flap/edge stiffness causes part of the out-of-plane displacement of the loaded blade to transform into an in-plane deflection. If the direction of the offset is suitably chosen, such in-plane deflections happens so that the blade deflects backwards, that is, towards the trailing edge. The resulting behaviour is similar to that of a scimitar, or swept, blade: the backward sweep shifts the resultant of the aerodynamic forces and this in turn induces an automatic torsion of the blade, with the resulting load alleviation effect discussed previously. Then, the load alleviating mechanism is similar to those induced by the fibers (that's why we kept the term BTC), but radically different in its functioning.
To demonstrate such coupled behaviour, we followed the same steps introduced with the F-BTC and conducted a series of simplified test cases according to the assumptions dis-

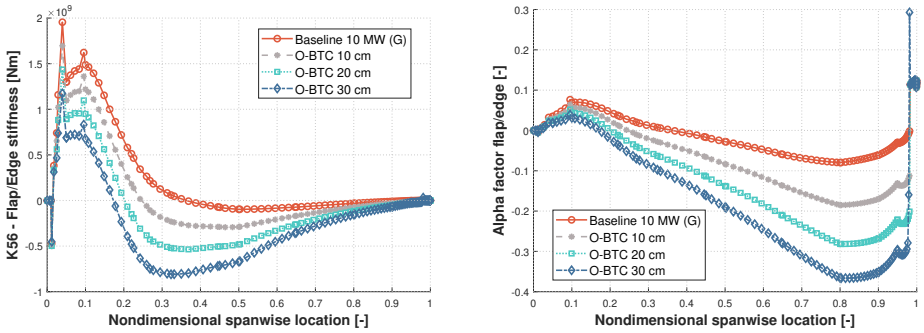

Figure 5.20: *Flap/Edge stiffness (left) and α_{FEC} factor (right) for varying values of the spar caps offset.*

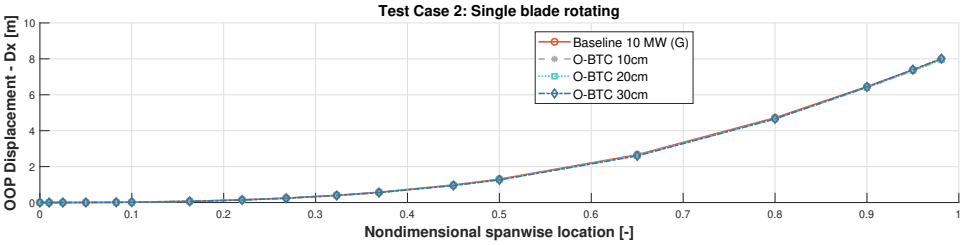

Figure 5.21: *Test case 2 with O-BTC: out-of-plane displacement.*

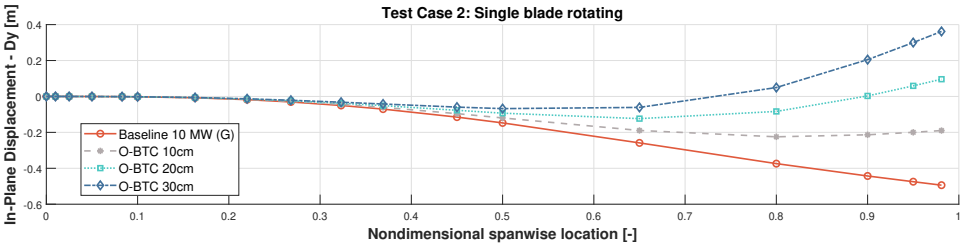

Figure 5.22: *Test case 2 with O-BTC: in-plane displacement.*

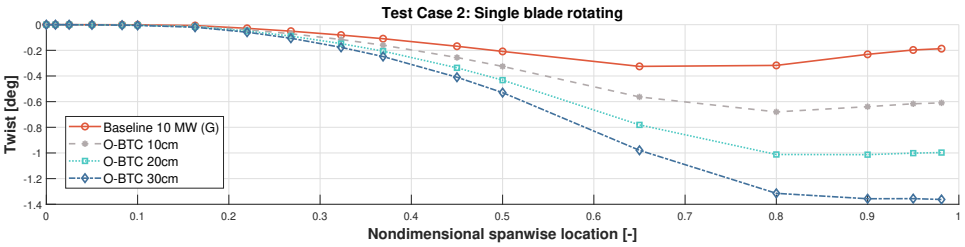

Figure 5.23: *Test case 2 with O-BTC: torsional deformation.*

cussed therein. The coupling effect between the flapwise and the edgewise deflections has been detected in all the cases, although for brevity we limit ourselves to present the out-

comes of test case 2, which is the application which resembles the most the real conditions of the turbine. In this test, we recall that a single blade is rotating at the nominal conditions of rotor and wind speed. The aerodynamic inflow is on, so that the aerodynamic loads are computed from the induction factors according to the BEM model. Figure 5.21 shows the out-of-plane deflection of the blade, while Fig. 5.22 shows the corresponding in-plane deflection. In accordance to our considerations, for a given flapwise deflection the edgewise one is higher for a higher level of coupling (offset). It must be noticed that the displacements are measured in a localized frame in which a positive Dy implies a backward deflection. As expected, the ultimate effect of the flap/edge coupled response is an induced torsion, whose distribution is visible in Fig. 5.23.

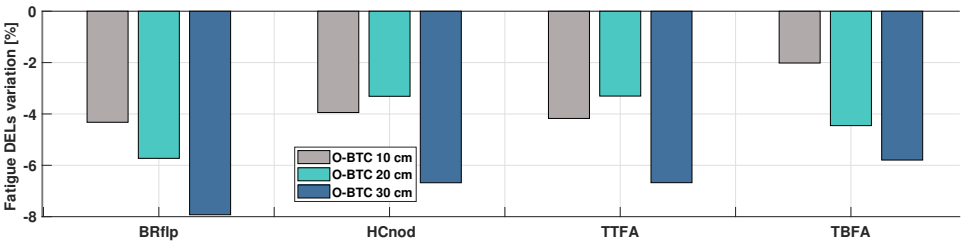

Figure 5.24: *Parametric O-BTC redesign: percent variation of the DEL against the Baseline 10 MW (G) rotor.*

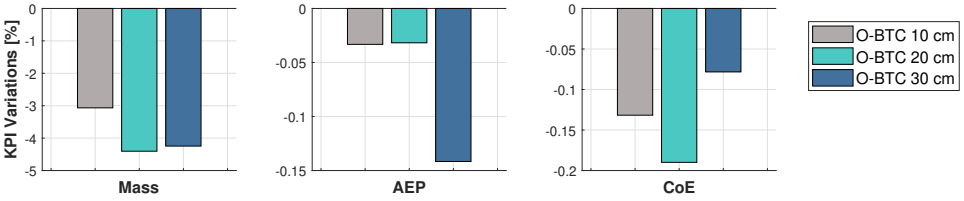

Figure 5.25: *Parametric O-BTC redesign: percent variation of the KPIs against the Baseline 10 MW (G) rotor.*

Like the case of the F-BTC analysis, it is important to understand if and how far can the coupling associated to the O-BTC influence the structural redesign of the rotor. To gain some light, we conducted a new parametric redesign in which the O-BTC solutions studied so far (10, 20 and 30cm) were completely re-optimized through the SDS module of `Cp-Max`. Figure 5.24 gives the percent variation of all the redesigned solutions against the Baseline 10 MW (G): the selected loads show that all the three configurations achieve a certain reduction, although the trend is not so clearly dependent on the amount of offset. Figure 5.25 shows the corresponding variations of the KPIs: it is important to underline an important difference between the F-BTC and the O-BTC. The former technique is based on the rotation of the fibers, which means that when the fibers are rotated, part of the flapwise stiffness is lost in favour of the coupling term. Usually, this requires to increase the thickness of the spar caps during the redesign, to compensate for this loss. With the O-BTC, instead, the fibers still work along their preferred direction, as the coupling is triggered by the geometry of the section rather than the anisotropy of the composites. This means that a load reduction is not correlated to an increase of the blade mass, and in fact, all the offset solutions achieve a lower mass. While the mechanism is still associated to a

certain AEP loss, this is almost neglectable for the solutions corresponding to 10 and 20 cm offsets. Quite interestingly, all the solutions succeed in reducing the COE.

5.2.1 Lightweight redesign with combined F/O-BTC

The fact that the functioning of the F-BTC and the O-BTC relies on different mechanisms might open the possibility to exploit the two techniques together. To investigate this opportunity, we repeated the optimal rotor sizing in which a rotor simultaneously equipped with F-BTC (5° of fiber rotation) and O-BTC (20cm offset) is re-designed in order to optimize the diameter. The design procedure was managed by the MDL of `Cp-Max` and, again, the design was constrained so that the loads on the fixed infrastructure (hub and tower) delivered by the optimal design should not exceed the 105% of those of the baseline. The optimal design, hereafter called LW 10 MW (G) F/O-BTC, resulted in a rotor diameter of 185.8 meters. The comparison between the fatigue loads of this solution and those of the baseline are given in Fig. 5.26: again, the rotor sizing is bounded by fatigue loads at hub, which grows with the size of the rotor and represent an active constraint.

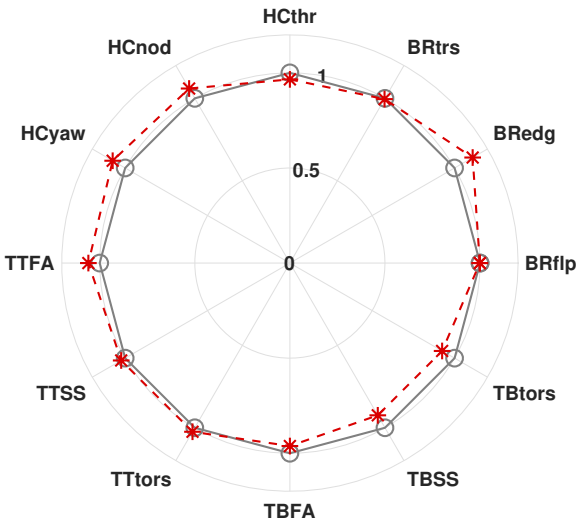

Figure 5.26: *Comparison between the fatigue loads of the Baseline 10 MW (G) wind turbine (solid grey line) and the LW 10 MW (G) F/O-BTC (red dashed line).*

A comparison of the KPIs is given in Table 5.3: an interesting result is that the combination of the two load mitigating techniques allows to achieve a slightly longer blade than the one designed in § 5.1.4. A consequence is a higher energy production and a cost reduction of about 2.5%. It is interesting to notice that, although the new rotor is slightly larger than the lightweight design with the sole F-BTC, the total blade mass is actually lower. This is due to the combined load alleviating effects which work in synergy and result in a further benefit on the cost of energy. In conclusion, the combination of F- and O-BTC summarized in the identifier F/O-BTC achieves a better design than the sole fiber-orientation technique. We conducted a similar study starting from the carbon baseline. Quite remarkably, the flap/edge coupling was clearly visible in the simplified test cases while its impact was very modest at design level. This different behaviour might be due to the different chordwise

Table 5.3: *Comparison between the KPIs of the Baseline 10 MW (G) wind turbine and the LW 10 MW (G) F/O-BTC.*

Performance	Baseline 10 MW (G)	LW 10 MW (G) F/O-BTC	Variation
Blade mass:	42574 kg	46099 kg	+8.28%
AEP:	46.4 GWh	47.98 GWh	+3.40%
CoE:	74.93 €/MWh	73.04 €/MWh:	-2.52%

positioning of the spar caps within the blade (see Fig. 4.13) or to the lower deflections associated to the use of carbon. A full account of such application is given by Polgati in his MSc Thesis [119].

5.3 Additional coupling through the shear webs

In the last part of this Chapter, we discuss an additional layer of structural tailoring, obtained through the combination of the O-BTC and a rotation of the fibers of the shear webs. The idea is to transform part of the edgewise deflection induced by the O-BTC into additional torsion, through the same principle which governs the F-BTC mechanism. Clearly, since the relative distance between the webs is small, we globally expect a small effect, however, it is interesting in our opinion to see the potential of this concept within a well-structured design evaluation. A qualitative sketch of the working principle is given in Fig. 5.27. Since the load-alleviation effect is obtained through a fiber rotation and the principal coupling is the one relating the edgewise deflection and the torsion, we call this mechanism F-ETC.

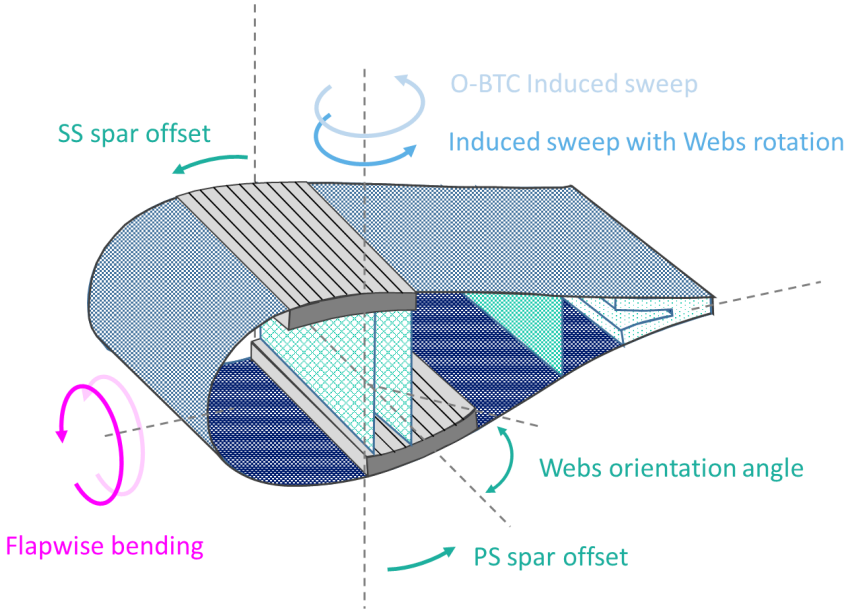

Figure 5.27: *Qualitative description of the F-ETC mechanism.*

As usual, we started this investigation with a stiffness analysis in which we studied the effect of an increasing fiber rotation in both shear webs. All solutions were applied to a basic configuration with 20cm spar offset, since the techniques are conceived to work together. The stiffness analysis led to interesting results, and showed that the rotation of the webs modifies several extra-diagonal terms of the stiffness matrix, including the Flap/Torsion coupling (although the magnitude is much lower than that introduced by a classic F-BTC), the Shear/Edge coupling and the Shear/Flap ones. The most important term, however, is the one relating the edgewise bending and the torsion. This term, which is the largest in magnitude, is shown for all the solutions in Fig. 5.28 (left).

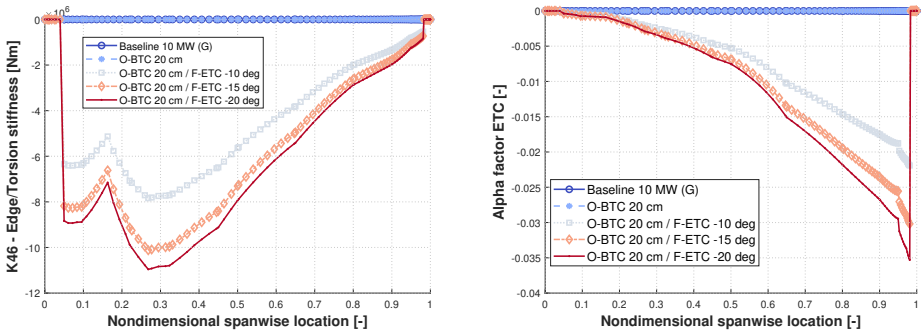

Figure 5.28: *Edge/Torsion stiffness (left) and α_{ETC} factor (right) for a 20cm spar offset and varying fiber orientations in the webs.*

As usual, a non-dimensional coupling factor could be defined as follows:

$$\alpha_{ETC} = \frac{K_{46}}{\sqrt{K_{44}K_{66}}} \tag{5.3}$$

in which K_{46} is the Edge/Torsion extra-diagonal term of the stiffness matrix, while K_{66} and K_{44} are, respectively, the diagonal terms related to the edgewise deformation and the torsion. The spanwise distribution of the factor is given in Fig. 5.28 (right). It is very interesting, then, to see that a coupling effect is indeed present after the rotation of the webs' fibers. However, the magnitude of the coupling is quite small when compared to that of the F-BTC or the O-BTC. This probably implies that the effects on the dynamic response of the rotor will be limited. However, we followed the usual road-map and performed the simplified test cases to check if the influence of the F-ETC is detectable in the behaviour of the blade. In all cases the peculiar behaviour was actually spotted, whereas here we give the sole results of test case 2,: Fig. 5.29 shows the in-plane deformation of the blade. All the three configuration with F-ETC (*plus* the O-BTC) are compared against the glass baseline, but also against the solution equipped with the sole O-BTC. This was done to highlight possible differences. In fact, due to the F-ETC mechanism, part of the edgewise deformation is indeed transformed into torsion. This is clearly visible in the torsional deformations given by Fig. 5.30. Although, as expected, the overall impact is modest there is a clear evidence of a trend with a larger torsion achieved for higher couplings.
To check the implications of the F-ETC at design level, we conducted a structural redesign of a rotor equipped with a 20cm spar caps offset *plus* a rotation of the web fibers of -20 degrees, since the latter configuration was found to give the most important load alleviation

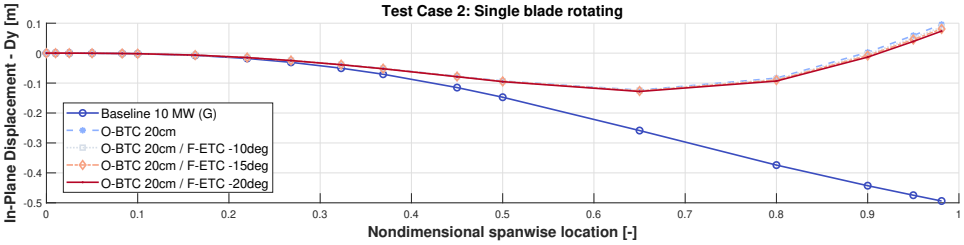

Figure 5.29: *Test case 2 with F-ETC: in-plane displacement.*

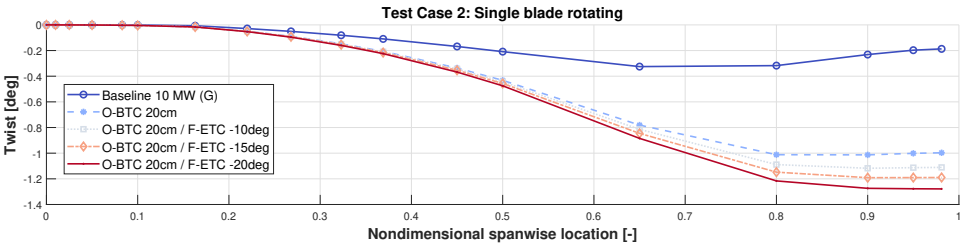

Figure 5.30: *Test case 2 with F-ETC: torsional deformation.*

from the simplified analysis. Figure 5.31 gives a comparison of the fatigue DELs developed by the resulted solution (acquamarine line) compared against those of the Baseline 10 MW (G) (grey line). To simplify the comparison, also the fatigue loads of a design with the sole O-BTC are provided (blue line). The results show that the introduction of the F-ETC provides a little improvement of the load mitigation, in particular in the side-side components of the tower base, in the fore-aft component at tower top and in the nodding component at the hub. In addition, although the blade edgewise component broadly depends on the blade mass, the F-ETC succeeds in reducing the equivalent load of a small amount.

Figure 5.32 provides the percent variations of the KPIs of both solutions (O-BTC and combined O-BTC/F-ETC) against the reference provided by the glass baseline. It is quite clear that, regardless to the additional load alleviation given by the F-ETC, the overall performance have worsened. In particular, although the blade mass is still lower than the original, it is slightly increased when compared to the genuine O-BTC case. This is probably a consequence of the fact that by introducing the F-ETC the shear webs lose some of their stiffness in the preferred directions, so that a higher thickness is required to absorb the fatigue loads. This is confirmed by looking at the thickness of the biaxial within the lamination of the webs, which is given in Fig. 5.33.

In the light of these results, we conclude that the load alleviating mechanism introduced by the F-ETC, although clearly present in the response of the blade, is not strong enough to provide significant design advantages. This can be due to the properties of the biaxial, which is typically employed in the manufacturing of the webs. However, a second redesign with a triaxial laminate in the webs did not result in better quantitative results. It is possible that different sectional topologies would encourage a better contribution from the F-ETC coupling: by increasing the distance among the webs, for example, the overall effect could be magnified. Similarly, different sectional arrangements with three webs (one to absorb fatigue and the others to ignite the coupling) could lead to a better exploitation of the concept. These ideas will be studied as part of the future developments of this work.

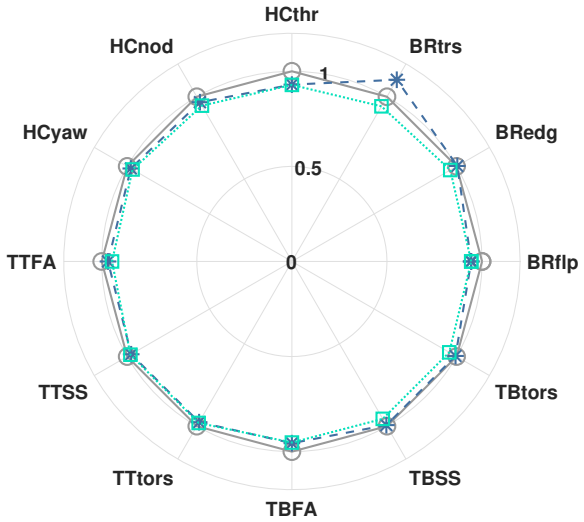

Figure 5.31: *Comparison between the fatigue loads of the Baseline 10 MW (G) (solid grey line), the O-BTC 20cm (blue) and the redesigned rotor with F-ETC (acquamarine).*

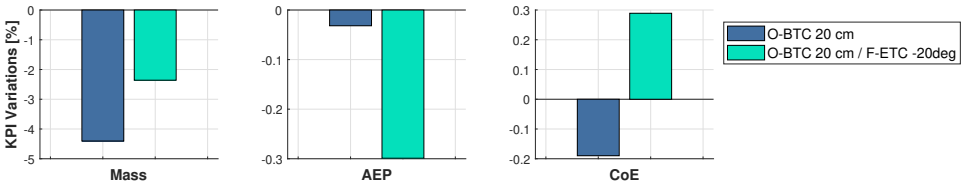

Figure 5.32: *F-ETC redesign: percent variation of the KPIs against the Baseline 10 MW (G) rotor.*

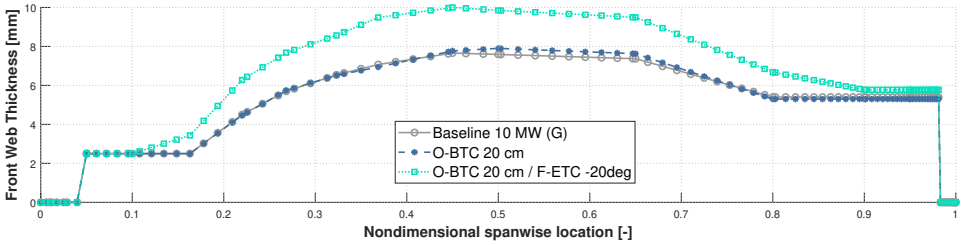

Figure 5.33: *F-ETC redesign: thickness of the shear webs.*

5.4 Conclusions

In this Chapter, we dealt with the problem of introducing several layers of structural tailoring in the design of large rotors. We investigated how it is possible to leverage on the materials, on the fiber orientation of the laminae and on the section topology to trigger different couplings in the elastic response of the rotor. The ultimate effect of all techniques is to transform part of the deformation of the blade into induced torsion, so that for an

increasing load the section can automatically reduce the angle of attack. In this view, we showed how the use of F-BTC, based on a direct rotation of the fibers, allows to achieve a significant reduction of ultimate and fatigue loads in modern rotors. When the structure is redesigned for a certain F-BTC, though, a typical drawback is a loss in the energy capture, due to larger deformations. However, if a suitable design procedure is tuned, it is possible to act on the rotor size (for a classic design) or on the control tuning (for low-induction rotors) to recover part of the AEP drop. We showed how this method allows to design lighter rotors for the same wind turbine. A second technique, the O-BTC based on the modification of the section topology, allows to introduce a coupling between the flapwise and the edgewise deformations of the blade, finally resulting in an additional contribution of induced torsion. The effectiveness of this strategy, however, depends on the blade at hand, in particular because the edgewise flexibility must be sufficient to exploit the mechanism. When this happens, however, the technique can reduce the loads. It is also possible to combine the F- and the O-BTC to exploit the characteristics of both techniques and achieve a better load reduction and, globally, a better improvement of the KPIs of the turbine. Finally, a novel layer of coupling which depends on the rotation of the fibers in the webs has been presented and discussed. We demonstrated the mechanism through simplified analysis, although a complete redesign highlighted no advantages over the other solutions under investigation.

CHAPTER 6

Lightweight redesign of a 20MW RWT

In this last Chapter, we present a redesign staged process in which the aim is to produce a lightweight rotor for the Baseline 20 MW developed in § 4.4. The idea is to conduct a series of design steps by resorting to the various modules of `Cp-Max`, in order to significantly reduce the rotor mass and the loads in the turbine components. This is a necessary step in the process of defining a 20 MW reference wind turbine, in particular because the Baseline 20 MW has been obtained after a structural optimization based on up-scaled parameters. While this allowed to achieve a feasible solution, and then a suitable starting point for our studies, there is no evidence that the characteristics of the rotor are indeed ideal with respect to same important KPIs. In this view, we conducted a series of parametric design studies in order to investigate the impact of several macro design features on the main ultimate and fatigue loads, as well as on our common set of performance indicators, which account for the blade mass, the AEP and the COE. This corresponds to operate the MDL of `Cp-Max` in manual mode: a certain parameter is manually modified in the definition of the macro design problem, then one or more design submodules are invoked to optimize certain features of the turbine. Although this strategy has several limitations when compared against a fully-automated macro design, it carries also some advantages: *in primis*, a larger number of DLC can be used, because imposing discrete values of the macro design variables typically reduces the number of iterations required by the algorithm to converge. After a certain parametric analysis, in fact, it is typically possible to identify the optimal, or close to, value of the varying parameter. This is particularly true when the initial configuration of the macro design loop is far from the optimum. Additionally, through a parametric approach it is possible to monitor a larger set of global KPIs rather than the sole COE and it is possible, at the end of each stage, to decide which way to go based on the analysis of the KPIs. Since we deal with a completely new class of turbines, in our opinion it is vital to monitor the evolution of several performance indicators before recurring to the automated

macro design, which will be postponed to a future, dedicated investigation.

6.1 Multi-staged design procedure

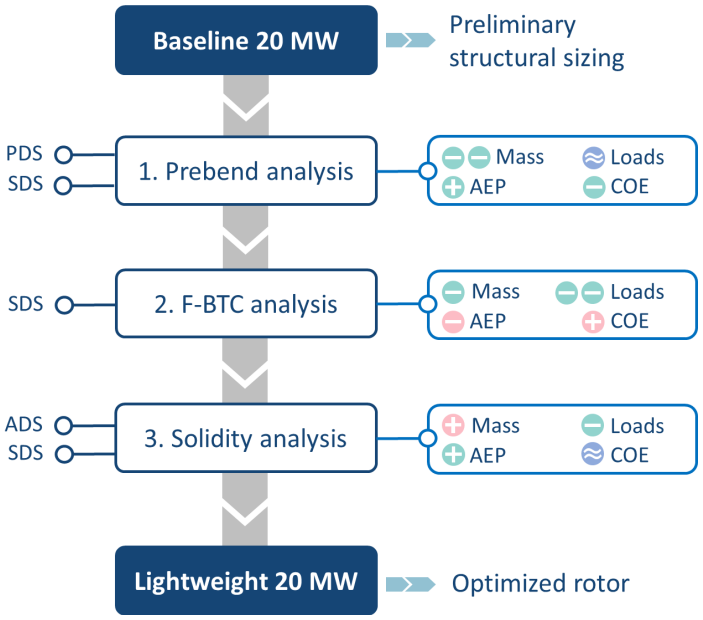

Figure 6.1: *Staged design process and step-by-step qualitative results.*

The design procedure is based on several steps, whose sequence is sketched in Fig. 6.1: here blue-shaded blocks represent the starting and ending points of the process, white blocks are instead parametric analysis, or design steps. For each analysis, the bullets to the left indicate which `Cp-Max` submodules have been employed during that analysis. In particular, the SDS is always called in order to re-design the structure of each solution under investigation. The blocks on the right give a qualitative overview of the results obtained at each design step: a green-shaded indicator means that the outcome is beneficial, while a red-shaded symbol represents detrimental effects. A *plus* sign implies that the corresponding quantity has increased during the current design step, while a *minus* sign indicates that the quantity has decreased. In both cases, a doubled sign implies that the variation is stronger, while an *equal* sign implies only minor variations. The starting point is our Baseline 20 MW, which has been developed as part of the activities described in this work. From here, we conducted the following parametric analysis:

1. **Prebend analysis**: since for simplicity the baseline has been designed with a straight-axis, we parametrically changed the prebend at tip and let the PDS module optimize the prebend shape according to procedure illustrated in § 3.2.4. The specified value of tip prebend enters as a constraint of the optimization problem, so that the PDS is forced to design the prebend distribution to match that value at tip. It is interesting to notice that in the current implementation of `Cp-Max` this analysis would be impossible in a fully-automated mode. In fact, the prebend at tip is not a global design variable, that is, the MDL has not a direct feedback on its value. According to the

first block of Fig. 6.1, the main achievement at this step is a significant reduction of the rotor mass. This is mainly due to the fact that the introduction of prebend leads to a relaxation of the tip deflection constraint.

2. **F-BTC analysis**: we exploit part of the concepts discussed in Chapter 5 to achieve significant load alleviation along the turbine. This is a fundamental step since the combination of a very long blade and a design based on fiberglass attains very high loads on both the rotor and the infrastructure. At this step, then, we equip the structure of the blade with a passive control technique by introducing a varying rotation of the spar caps fibers. As discussed in the previous Chapter, a known by-product of the F-BTC is a certain loss of the energy production, which leads to a small increase of the COE.

3. **Solidity analysis**: since the Baseline 20 MW has a very wide maximum chord, here we gradually reduce the target rotor solidity and redesigned the chord and twist distributions of the blade in order to achieve the maximum energy yielding. This is done by the ADS following the procedure detailed in § 3.2.2. At the end of the analysis it was possible to reduce the maximum chord of the optimal rotor and to alleviate the associated transportation issues. Additionally, the procedure led to a further load alleviation, mainly due to the reduced planform of the blade which limits the ultimate loads form storm conditions.

At the end of each step, the best configuration was taken as the starting point of the following one, so that the advantages obtained at each level could be combined together in the final redesign. To further simplify the complexity of the problem, the design is limited to the rotor whereas tower, nacelle, hub and foundations are considered as frozen. Similarly, the airfoils and the corresponding aerodynamic data are not changing during the design, that is, the rotor was optimized for a given set of airfoils. The full set of DLC described in § 4.1 has been used during the recursive structural redesign, whereas the evaluation of the COE is based on the updated scaling model from INNWIND, to enusre the consistency of the results with the other activities presented in this work.

6.2 Results

6.2.1 Prebend analysis

In the first parametric analysis we investigate the impact of a varying distribution of prebend along the blade. The Baseline 20 MW rotor was compared against two solutions characterized by a tip prebend of 2 m and 4 m respectively. While the tip prebend was imposed as part of the parametric study, the optimal shape of the prebend was designed by the dedicated prebend design submodule of `Cp-Max`. The resulting distributions are illustrated for the three cases under consideration in Figure 6.2. It must be noticed that the negative prebend occurring at the region close to the blade root is a typical result of how the prebend design problem is cast (see Fig. 3.5). This value can be limited as part of the formulation of the nonlinear constraints of the PDS, however, no bounding values have been defined in this work, to avoid an unnecessary limitation of the design space.
Figure 6.3 shows the variation of fundamental fatigue DEL experienced by the optimal solutions against those of the Baseline 20 MW: the results are normalized so that figures referring to the Baseline 20 MW are equal to one. As usual, BR identifies the blade root,

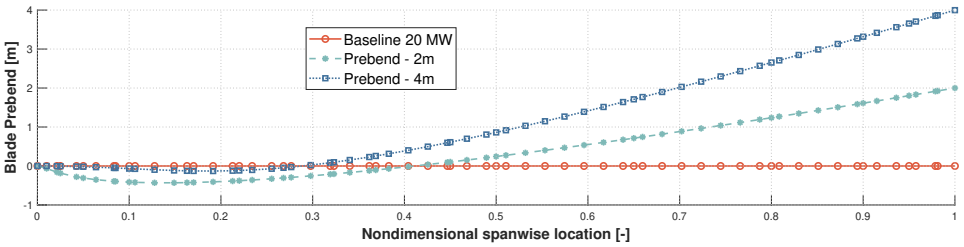

Figure 6.2: *Prebend analyisis: spanwise optimal prebend distribution.*

HC the hub center, TT and TB the top and the base of the tower. The *flp* and *edg* components represent the flapwise and edgewise bending loads, whereas *nod* and *yaw* are the nodding and yawing components at the hub. *FA* and *SS* identifies the fore-aft and side-side components of the tower bending. Similarly, Figure 6.4 shows the normalized variations of the KPIs considered in this study. The results show that the main advantage associated to the introduction of prebend is a mass saving up to 5%: this is due to the larger clearance between blade and tower, which contributes to relax the constraint on the maximum tip displacement, which is an active constraint on the structural design of the Baseline 20 MW.

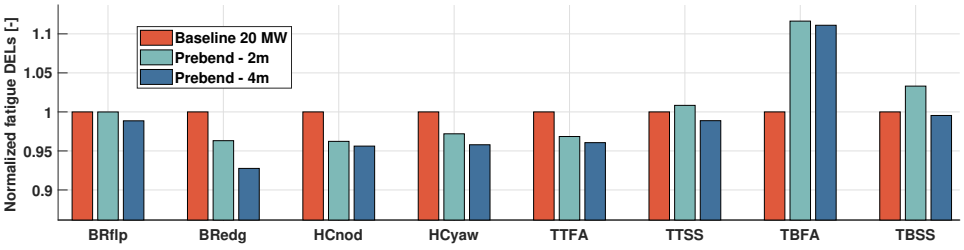

Figure 6.3: *Prebend analyisis: normalized variation of the fatigue DEL. BR is blade root, HC is hub center, TT is tower top and TR is tower root.*

The effect on the fundamental fatigue DEL is generally beneficial, with reductions in the order of 3 to 5% at the blade root, hub center and tower top. In particular, the reduction of the blade edgewise DEL can be directly associated to the reduction in the total blade mass. However, the fore-aft DEL at the tower root is increased of about 10%. In our experience, however, the tower design is heavily constrained by buckling in the vicinity of the root, so that this increase is considered acceptable at this step. It is important to notice that the formulation of the prebend optimization seeks to maximize the rotor swept area under rated loads, and the typical main effect is a slight increase of the AEP which, together with the reduction of the blade mass, allows to achieve a reduction of the COE in both optimal solutions. However, since the Prebend - 4m configuration combines the higher cost reduction and the largest load alleviation, this solution is considered the most promising at this step and used to initiate the next design step.

6.2.2 F-BTC analysis

In the second parametric analysis of the design process, we focused on the reduction of the fatigue loads by introducing a varying amount of built-in structural tailoring to the layup

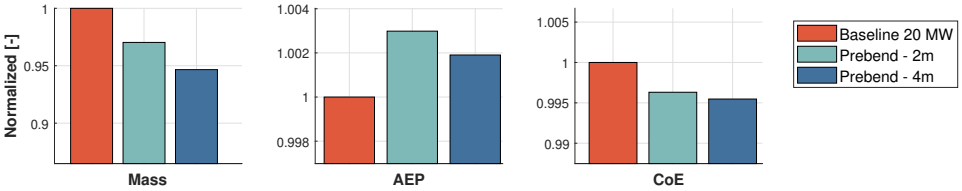

Figure 6.4: *Prebend analyisis: normalized variation of the KPIs.*

of the blade. This was mainly achieved through a fiber-induced Bend-Twist Coupling (F-BTC) according to the methodology described in Chapter 5. Three solutions have been tested, all of them characterized by a uniform rotation of the spar cap fibers. We tested three solutions with 4, 6 and 8 degrees of fiber orientation and again, for each solution, we performed a complete structural optimization loop to ensure the minimization of the total ICC. The comparison between the normalized fatigue DEL of the three solutions against the Prebend - 4m, which is the staring point of this second analysis, is given in Figure 6.5.

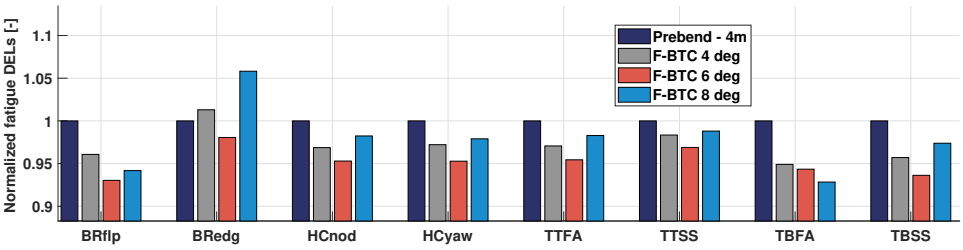

Figure 6.5: *F-BTC Analysis: normalized variation of the fatigue DEL.*

It is possible to observe how the F-BTC ensures a significant alleviation of the fatigue DEL. In particular, the flapwise DEL at blade root is reduced by 7% while the main DEL at the hub center are about 5% lower than the initial configuration. These results are consistent to those discussed in the dedicated Chapter. Finally, the fore-aft and side-side DEL at tower root are reduced by more than 5%, which in part contributes to compensate the increased loads experienced at the previous step. The normalized variation of the main KPI is given in Figure 6.5. As expected, the solutions with F-BTC lead to a small decrease in the AEP: this is a consequence of the additional torsion induced by the structural tailoring, which drives the individual airfoils along the blade away from their point of maximum efficiency. It is interesting to notice how the blade mass decreases for increasing fiber rotation. However, an excessive rotation of the fibers can significantly reduce the flapwise stiffness of the blade, leading to a higher thickness of the spar caps, which ultimately increases the mass. The overall impact on the COE is negligible for the three solutions, however, considering that the F-BTC 6 degrees provides the best load alleviation effect, this is identified as the optimal solution at this step and supplied to the next one.

6.2.3 Solidity analysis

In the last step of the design, we investigated the impact of a parametric variation of the rotor solidity. For each solution, we run the aerodynamic design submodule of `Cp-Max` to optimize the chord and twist distribution along the blade. The resulting shapes are

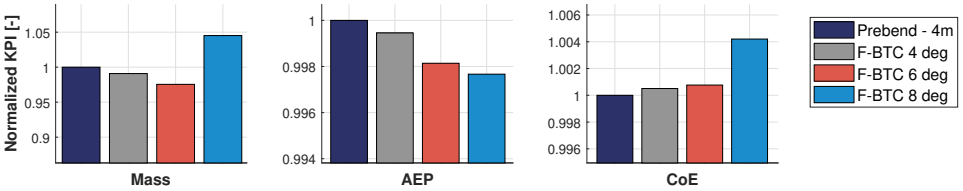

Figure 6.6: *F-BTC Analysis: normalized variation of the KPIs.*

compared in Figure 6.7, which shows quite clearly how the ADS optimizes the shape for a certain target value of solidity. At the end of each aerodynamic redesign, we run a full structural redesign to minimize the ICC of the turbine.

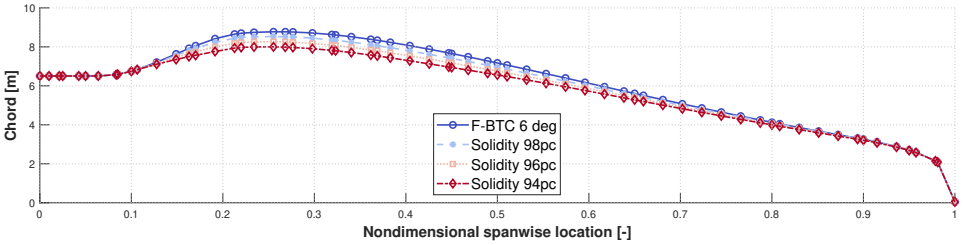

Figure 6.7: *Solidity analysis: optimal chord distributions.*

The main achievements in terms of fatigue loads are reported in Figure 6.8, while the variation of the main KPI is given in Figure 6.9. The main effect of the reduced solidity is a general alleviation of the fatigue loads, in particular at the tower base: this is mainly related to the lower planform of the blade. However, by reducing the solidity it is necessary to increase the thickness of the structural components, in particular of the spar caps, to compensate for the loss of sectional stiffness. The result is, unsurprisingly, an increasing blade mass for a decreasing solidity. This justifies the increase in the edgewsie DEL at root. At this step, the variations of the AEP and COE are very small, however, we concluded that the Solidity 96pc gives the best advantages in terms of costs and load alleviation, so that we selected this configuration as the optimal point of the redesign process. This solution is hereafter referred as Lightweight 20 MW.

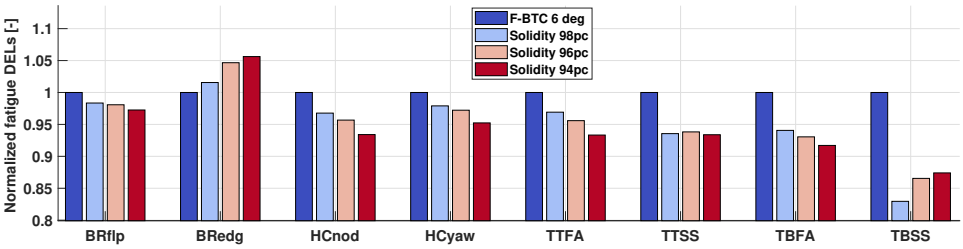

Figure 6.8: *Solidity analysis: normalized variation of the fatigue loads.*

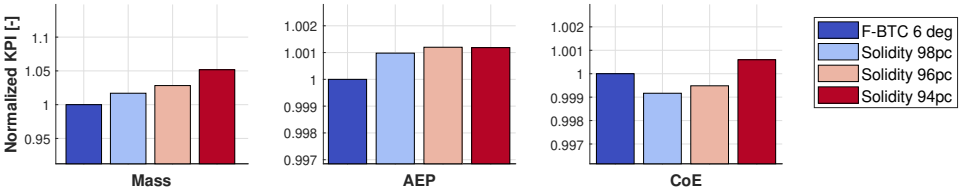

Figure 6.9: *Solidity analysis: normalized variation of the KPIs.*

6.2.4 Summary of the redesign process

At the end of the process, we compared the Lightweight 20 MW against the Baseline 20 MW. An overview of the results is given in Table 6.1 in terms of regulation parameters, geometry and KPIs. The optimal rotor has a solidity 4% lower than the initial, while the chord is 6% shorter. An optimal prebend at tip of 4 meters was introduced in the final redesign. The lightweight rotor is also characterized by a rotation of 6 degrees applied to the laminae of the spar caps. The comparison shows improvements in all the monitored indicators: in particular, a 5% reduction in the total blade mass was achieved through the design process. This saving is mostly related to the thickness of the spar caps and is a trade-off between the prebend, the F-BTC and the additional ply thickness needed by the lower optimal solidity. The turbulent AEP, which is computed by averaging the power production in DLC 1.2, is 0.12% higher than the Baseline, and the two advantages ultimately result in a 0.4% reduction of the COE.

Table 6.1: *Performance comparison between the Baseline 20 MW and the Lightweight 20 MW rotors.*

	Units	Baseline 20 MW	Lightweight 20 MW	Variation
Rotor speed	[RPM]	6.77	6.82	+0.74%
TSR	[-]	7.73	7.86	+1.68%
Rated wind speed	[m/s]	11.6	11.4	-0.95%
Max chord	[m]	8.77	8.27	-5.70%
Prebend at tip	[m]	0.0	4.0	
Spar caps fiber angle	[deg]	0.0	6.0	
Total blade mass	[ton]	113.5	107.8	-5.05%
AEP	[GWh]	91.6	91.7	+0.12%
COE	[€/MWh]	84.9	84.6	-0.42%

Figure 6.10 shows a direct comparison between the main fatigue loads at different components along the turbine. Figure 6.11 provides a similar comparison for the ultimate loads. All the fatigue load metrics are significantly reduced, in particular those at the hub and at the tower top, which are consistently reduced of more than 10%. The side-side loads at tower base have been reduced by 20%, which is important because the side-side corresponds to an underdamped mode of the turbine and its prone to vibrations. Such reduction, in fact, can easily be the proof of a more vibration-free design. Such reduction of the main

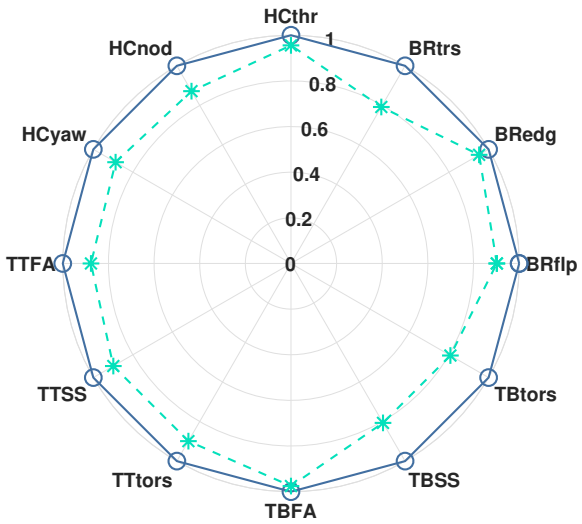

Figure 6.10: *Comparison between the fatigue loads of the Baseline 20 MW (solid blue) and Lightweight 20 MW (dashed green) wind turbines.*

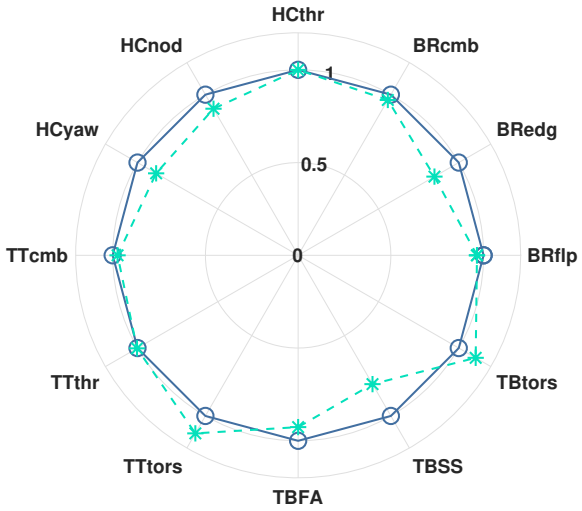

Figure 6.11: *Comparison between the ultimate loads of the Baseline 20 MW (solid blue) and Lightweight 20 MW (dashed green) wind turbines.*

loads is in part due to the lower rotor mass, whereas the main load alleviation mechanism depends on the F-BTC effect introduced through the ply orientation. The comparison of the ultimate loads shows some improvement of the Lightweight 20 MW against the baseline (in particular at the hub), whereas the torsion in the tower is slightly higher. This fact, however, has only minor implications on the design of the tower. On the contrary, considering the important load reduction, a dedicated redesign of the hub and the tower could provide additional cost savings.

6.3 Conclusions

In this Chapter, we performed a multi-staged optimization of our 20 MW baseline, with the goal of delivering a lightweight configuration for the same diameter, power and class. The design focused mainly on the rotor, which has been redesigned by exploiting the different modules of `Cp-Max` . At the end of redesign, we were able to achieve a global improvements of selected KPIs of the turbine. In particular, the total blade mass and the fatigue loads have been significantly decreased when compared against the initial configuration, making room for lighter and cheaper support structures. The main limitation of this work lies in the use of a parametric procedure instead of a fully automated one. However, this choice made possible to perform a great deal of analysis within a reasonable computational effort. On the other hand, in our opinion the satisfactory margins of improvement of the results fully justifies this course of action. These preliminary results will be compared against an automated macro design in a dedicated follow-up of this activity. Incoming activities will also focus on the detailed structural verification through 3D FEM, and on the application of additional load mitigating techniques.

CHAPTER 7

Conclusions

7.1 A final discussion

In this work, we have investigated the design of next-generation wind turbines through a system-engineering approach. The fundamental consideration which drives our efforts is that, as the standard size of wind turbines grows larger, traditional design procedures meet their limits and are no longer able to safely provide optimal solutions. A growing body of literature supports the idea that very large wind turbines should be designed with dedicated algorithms, which must forcibly implement a system-engineering vision. The development of such an approach is far from being trivial since increased complexities require, firstly, a higher fidelity of the physical models employed for the simulation of the wind turbine. The dynamic behaviour of large turbines, in fact, is dominated by the interactions of several factors like the aerodynamic inflow, the elastic response of the flexible elements, the wave and platform motion, the system stability. To conduct a safe and economically-beneficial design, these cross-correlations should be fully resolved at simulation level. Another native complexity of a system-engineering approach is the fact that, since several turbine components are included in the optimization problem, these algorithms must be able to manage a variety of highly-heterogeneous design variables, which pertain to different aspects of the design. Finally, it is necessary to adopt a holistic merit function as the objective of a well-posed optimization problem: typical examples from the literature include combinations of different discipline-specific merit functions (like the AEP and the rotor loads) and, recently, cost models for the computation of the COE. These requirements have forced the researchers to adopt compromises by prioritizing some aspects rather than the others, and this resulted in the development of different SDO philosophies. At present, different optimization architectures are available, some of them based on a monolithic, or sequential approach, while others implement a nested, or multi-level construction. Whilst successful

design applications have been conducted for each of the available solutions, there is not a recognized evidence that a certain method is globally better than others. A great effort is currently being paid within IEA Wind Task 37 [101] to draw unified conclusions on this topic and to possibly identify best practices for developing SDO algorithms. In this work, we approached the system design of large wind turbines from two directions, whose characteristics are summarized in Table 7.1.

Table 7.1: *Summary of the developed tools.*

	Free-Form	`Cp-Max`
Capabilities	MDO + rotor sizing	SDO
Architecture	Monolithic	Multi-level
Number of variables	High (100+)	Low at macro level Custom at sub-levels
Objective	COE	COE (macro) AEP (aerodynamic) Rotor Area (prebend) ICC (structural)
Modelling	Rigid BEM + 1D flexible beam + 2D sectional FEM	Multi-body nonlinear model + 2D/3D FEM
Load cases	Steady storm + operating	Arbitrary set of DLC
Constraints	Basic integrity constraints	IEC-61400 compliant
Typical runtime	~1 day	1~2 weeks

A first methodology implements a fully-monolithic *free-form* optimization in which many variables are designed at same level. The main feature of this algorithm is the possibility to optimize the airfoil shapes together with a set of classic aero-structural variables. In Chapter 2, we presented several design applications in which the program is used as an MDO for rotor design. Results show that, although the relative simplicity of the set-up, the algorithm manages complex design tasks quite successfully. For example, the algorithm was able to automatically trade some aerodynamic performance in favour of the structure (see § 2.4.1) and to generate specific configurations like flatback airfoils when required by the design (see for instance Fig. 2.9). Another important novelty is the possibility to optimize the rotor size, the airfoils *and* the blades at the same level, that is, to use the *free-form* as a basic SDO tool. We showed in § 2.4.3 that in this context a partial low-induction solution was automatically designed, a result which is unique to date. As shown by the bottom line of Table 7.1, the fundamental asset of the *free-form* lies in its computational speed, which is in the order of hours/days.

A second design methodology was developed in Chapter 3 and implements a genuine SDO perspective, as it supports the optimization of the wind turbine features and of the individ-

ual subcomponents. A fundamental feature of this method is that relies on a multi-body modelling of the wind turbine and on a set of fully-resolved DLC for the computation of the loads on the turbine. The multi-level architecture of `Cp-Max` discussed in § 3.2 poses some limits on the number of design variables especially because it requires a much longer runtime when compared against the *free-form* approach. In Chapter 4 we exploited the SDO tool to optimize our 10 MW and 20 MW baseline rotors. Then, we investigated possible directions to achieve lightweight rotors. In Chapter 5 we showed how structural tailoring can significantly relieve the loading on the turbine components and ultimately allow an increase of the diameter. In § 5.1 we studied the concept of material BTC showing its potential for load alleviation, then we investigated additional structural tailoring induced by the modification of the sectional layout. A key result is that, when applied to our 10 MW glass baseline, the combination of the two mechanisms works better than the individual ones, leading to a net reduction of the COE. In § 5.3, we introduced a novel way to achieve structural coupling, based on the combination of the O-BTC and an edge/torsion deformation due to the shear webs. Although we demonstrated the working principle of the mechanism, no particular effects were achieved at design-level. Interestingly enough, however, this strategy allows a reduction of the blade edgewise fatigue loads, which usually are largely determined by the blade mass. In Chapter 6, we conducted a semi-automated optimization of the 20 MW baseline to significantly reduce the system loads (see Figs. 6.10 and 6.11) and design a novel lightweight configuration.

7.2 Outlook

The research in the field of SDO design of modern wind turbines is quite recent, and several aspects and possibilities should be explored in the years to come. Concerning our activities, here follows a list of suggestions which highlight possible research directions.

Both the *free-form* methodology and `Cp-Max` showed a broad potential and produce important and innovative results. It is clear, however, that the latter approach is the most powerful, while the first served mainly as a *proof-of-concept* of the integration of the airfoil design. It would be interesting, then, to merge both procedures into a unified program. At present, probably the best way to to this would be to introduce the airfoil design within `Cp-Max`, either keeping the same parametrization employed in the *free-form* or through a different one. It would be extremely interesting to see whether some of the results produced by the *free-form* are confirmed in a more complete design framework.

At present, the range of applications of `Cp-Max` is limited by the fact that the design of the drive-train and generator is not supported. As discussed for example by Bortolotti et al. [89], this could lead the optimization towards a too optimistic diameter-sizing. Some researchers have recently presented models for driving the design of such components, for example Guo et al. [120, 121] and it would be interesting to study the effects of such models within `Cp-Max`.

A similar limitation concerns how `Cp-Max` deals with offshore systems and, specifically, with the supporting structures. At present, the tool supports the analysis (but not the design) of mono-piles, which are represented in the multi-body formulation through a combination of a flexible beam and a lifting line, both associated to a certain wave motion. This description suffices for coastal turbines in shallow waters, however, the focus of the offshore wind market is rapidly shifting towards floating wind farms. It has been esti-

mated that supporting structures and foundations can account up to 14% of the COE of an offshore turbine [122] and this suggests that it would be valuable to modify `Cp-Max` in order to manage the simulation and design of such components. This would require to couple `Cp-Lambda` to a dedicated module for the computation of hydrodynamic loads (like for example `HydroDyn` [123]) or to embed a dedicated hydrodynamic model in the solver.

Most research projects are now concerned with the development of analysis and design tools at wind-farm level. While the current release of `Cp-Max` is limited to the design of a sole wind turbine, it would be interesting to further expand the program in order to study the design of a turbine within a certain plant, or potentially to optimize the wind farm layout in the context of a dedicated cost model (see for example [124]).

Bibliography

[1] IRENA. *Renewable Power Generation Costs in 2017*. Tech. rep. International Renewable Energy Agency (IRENA), 2018.

[2] M. Stettner, M. J. Reijerkerk, A. Lünenschloß, V. Riziotis, A. Croce, L. Sartori, R. Riva, and J. M. Peeringa. "Stall-Induced Vibrations of the AVATAR Rotor Blade". In: *Journal of Physics: Conference Series* 753.4 (2016), p. 042019.

[3] M. H. Hansen. "Aeroelastic stability analysis of wind turbines using an eigenvalue approach". In: *Wind Energy* 7.2 (2004), pp. 133–143. DOI: 10.1002/we.116. eprint: https://onlinelibrary.wiley.com/doi/pdf/10.1002/we.116.

[4] J. C. Berg, M. F. Barone, and N. C. Yoder. *SMART Wind Turbine Rotor: Data Analysis and Conclusions*. Tech. rep. SAND2014-0712. Albuquerque, New Mexico: Sandia National Laboratories, 2014.

[5] J. F. Manwell, J. G. McGowan, and A. L. Rogers. *Wind Energy Explained: Theory, Design and Application*. 2nd Edition. John Wiley & Sons, Dec. 2009.

[6] J. A. Buck and S. D. Garvey. "Redefining the design objectives of large offshore wind turbine rotors". In: *Wind Energy* 18.5 (), pp. 835–850. DOI: 10.1002/we.1733. eprint: https://onlinelibrary.wiley.com/doi/pdf/10.1002/we.1733.

[7] A. S. Ning, R. Damiani, and P. J. Moriarty. "Objectives and Constraints for Wind Turbine Optimization". In: *Journal of Solar Energy Engineering* (2014).

[8] P. Bortolotti, L. Sartori, A. Croce, and C. L. Bottasso. "Multi-MW wind turbine CoE reduction via a multi-disciplinary design process". In: *Proceedings of the EWEA 2015*. 2015.

[9] P. K. Chaviaropoulos, H. J. M. Beurskens, and S. G. Voutsinas. "Moving Towards Large(r) Rotors Is that a good idea?" In: *Proceedings of EWEA 2013*. Vienna, Austria, 2013.

[10] G. Kenway and J. R. R. A. Martins. "Aerostructural Shape Optimization of Wind Turbine Blades Considering Site-Specific Winds". In: *12th AIAA/ISSMO Multidisciplinary Analysis and Optimization Conference*. Victoria, British Columbia, Canada, Sept. 2008.

[11] W. Xudong, W. Z. Shen, W. J. Zhu, J. N. Sørensen, and C. Jin. "Shape optimization of wind turbine blades". In: *Wind Energy* 12.8 (2009), pp. 781–803. DOI: 10.1002/we.335. eprint: https://onlinelibrary.wiley.com/doi/pdf/10.1002/we.335.

[12] A. Pourrajabian, P. A. Nazmi Afshar, M. Ahmadizadeh, and D. Wood. "Aero-structural design and optimization of a small wind turbine blade". In: *Renewable Energy* 87 (2016). Optimization Methods in Renewable Energy Systems Design, pp. 837–848. ISSN: 0960-1481. DOI: https://doi.org/10.1016/j.renene.2015.09.002.

[13] C. L. Bottasso, F. Campagnolo, and A. Croce. "Multi-disciplinary constrained optimization of wind turbines". In: *Multibody System Dynamics* 27.1 (Jan. 2012), pp. 21–53. ISSN: 1573-272X. DOI: 10.1007/s11044-011-9271-x.

[14] M. Sessarego and W. Z. Shen. "Aero-structural optimization of wind turbine blades using a reduced set of design load cases including turbulence". In: *Journal of Physics: Conference Series* 1037.4 (2018), p. 042018.

[15] C. Pavese, C. Tibaldi, T. J. Larsen, T. Kim, and K. Thomsen. "Reduced Design Load Basis for Ultimate Blade Loads Estimation in Multidisciplinary Design Optimization Frameworks". In: *Journal of Physics: Conference Series* 753.6 (2016), p. 062005.

[16] J. Zhu, X. Cai, and R. Gu. "Aerodynamic and Structural Integrated Optimization Design of Horizontal-Axis Wind Turbine Blades". In: *Energies* 9.2 (2016). ISSN: 1996-1073. DOI: 10.3390/en9020066.

[17] A. Dal Monte, S. De Betta, M. Raciti Castelli, and E. Benini. "Proposal for a coupled aerodynamic–structural wind turbine blade optimization". In: *Composite Structures* 159 (2017), pp. 144–156. ISSN: 0263-8223. DOI: https://doi.org/10.1016/j.compstruct.2016.09.042.

[18] H. Yang, J. Chen, X. Pang, and G. Chen. "A new aero-structural optimization method for wind turbine blades used in low wind speed areas". In: *Composite Structures* 207 (2019), pp. 446–459. ISSN: 0263-8223. DOI: https://doi.org/10.1016/j.compstruct.2018.09.050.

[19] P. W. Richards, D. T. Griffith, and D. H. Hodges. "Aeroelastic design of large wind turbine blades considering damage tolerance". In: *Wind Energy* 20.1 (2016), pp. 159–170. DOI: 10.1002/we.1997. eprint: https://onlinelibrary.wiley.com/doi/pdf/10.1002/we.1997.

[20] C. Pavese, C. Tibaldi, F. Zahle, and T. Kim. "Aeroelastic multidisciplinary design optimization of a swept wind turbine blade". In: *Wind Energy* 20.12 (2017), pp. 1941–1953. DOI: 10.1002/we.2131.

[21] P. Fuglsang, C. Bak, J. G. Schepers, B. Bulder, T. T. Cockerill, P. Claiden, A. Olesen, and R. van Rossen. "Site-specific Design Optimization of Wind Turbines". In: *Wind Energy* 5.4 (2002), pp. 261–279. DOI: 10.1002/we.61. eprint: https://onlinelibrary.wiley.com/doi/pdf/10.1002/we.61.

[22] K. Maki, R. Sbragio, and N. Vlahopoulos. "System design of a wind turbine using a multi-level optimization approach". In: *Renewable Energy* 43 (2012), pp. 101–110. ISSN: 0960-1481. DOI: https://doi.org/10.1016/j.renene.2011.11.027.

[23] T. Ashuri, M. B. Zaaijer, J. R. R. A. Martins, G. J. W. van Bussel, and G. A. M. van Kuik. "Multidisciplinary design optimization of offshore wind turbines for minimum levelized cost of energy". In: *Renewable Energy* 68.Supplement C (2014), pp. 893–905. ISSN: 0960-1481. DOI: https://doi.org/10.1016/j.renene.2014.02.045.

[24] T. Ashuri, M. B. Zaaijer, J. R. R. A. Martins, and J. Zhang. "Multidisciplinary design optimization of large wind turbines—Technical, economic, and design challenges". In: *Energy Conversion and Management* 123 (2016), pp. 56–70. ISSN: 0196-8904. DOI: https://doi.org/10.1016/j.enconman.2016.06.004.

[25] K. Dykes, A. Ning, R. King, P. Graf, G. Scott, and P. Veers. "Sensitivity Analysis of Wind Plant Performance to Key Turbine Design Parameters: A Systems Engineering Approach". In: *AIAA SciTech 2014*. National Harbor, Maryland, Jan. 2014.

[26] J. Gray, K. T. Moore, and B. A. Naylor. "OpenMDAO: An Open Source Framework for Multidisciplinary Analysis and Optimization". In: *13th AIAA/ISSMO Multidisciplinary Analysis Optimization Conference*. 2010.

[27] F. Zahle, C. Tibaldi, D. R. Verelst, C. Bak, R. Bitsche, and J. P. A. A. Blasques. "Aero-Elastic Optimization of a 10 MW Wind Turbine". In: *Proceedings - 33rd Wind Energy Symposium*. Vol. 1. American Institute of Aeronautics & Astronautics, 2015, pp. 201–223.

[28] L. Sartori, F. Grasso, C. L. Bottasso, and A. Croce. "Integration of Airfoil Design during the design of new blades". In: *Proceedings of the ICOWES 2013 conference*. Lyngby, Denmark, 2013.

[29] C. L. Bottasso, P. Bortolotti, A. Croce, and F. Gualdoni. "Integrated aero-structural optimization of wind turbines". In: *Multibody System Dynamics* 38.4 (Dec. 2016), pp. 317–344. ISSN: 1573-272X. DOI: 10.1007/s11044-015-9488-1.

[30] G. Sieros, P. Chaviaropoulos, J. D. Sørensen, B. H. Bulder, and P. Jamieson. "Upscaling wind turbines: theoretical and practical aspects and their impact on the cost of energy". In: *Wind Energy* 15.1 (2012), pp. 3–17. DOI: DOI:10.1002/we.527.

[31] M. O. L. Hansen. *Aerodynamics of wind turbines*. Earthscan, 2015.

[32] J. F. Manwell, J. G. McGowan, and A. L. Rogers. *Wind energy explained: theory, design and applications, 2nd edition*. Wiley, 2009.

[33] T. Wang. "A brief review on wind turbine aerodynamics". In: *Theoretical and Applied Mechanics Letters* 2.6 (2012), p. 062001. ISSN: 2095-0349. DOI: https://doi.org/10.1063/2.1206201.

[34] P. Fuglsang, C. Bak, M. Gaunaa, and I. Antoniou. "Design and Verification of the Risø-B1 Airfoil Family for Wind Turbines". In: *Journal of Solar Energy Engineering* 126.4 (2004), pp. 1002–1010.

[35] C. Bak, N. Gaudern, F. Zahle, and T. Vronsky. "Airfoil design: Finding the balance between design lift and structural stiffness". In: *Journal of Physics: Conference Series* 524.1 (2014), p. 012017.

[36] B. Méndez, X. Munduate, and U. San Miguel. "Airfoil family design for large offshore wind turbine blades". In: *Journal of Physics: Conference Series* 524.1 (2014), p. 012022.

[37] F. Grasso. "Design of a family of new advanced airfoils for low wind class turbines". In: *Journal of Physics: Conference Series* 555.1 (2014), p. 012044.

[38] C. L. Bottasso, F. Campagnolo, A. Croce, S. Dilli, F. Gualdoni, and M. B. Nielsen. "Structural optimization of wind turbine rotor blades by multilevel sectional/multibody/3D-FEM analysis". In: *Multibody System Dynamics* 32.1 (June 2014), pp. 87–116. ISSN: 1573-272X. DOI: 10.1007/s11044-013-9394-3.

[39] C. L. Bottasso, A. Croce, and L. Sartori. "Free-form Design of Low Induction Rotors". In: *33rd Wind Energy Symposium, AIAA SciTech Forum*. Kissimmee, Florida, 2015. DOI: https://doi.org/10.2514/6.2015-0488.

[40] W. J. Zhu, W. Z. Shen, and J. N. Sørensen. "Integrated airfoil and blade design method for large wind turbines". In: *Renewable Energy* 70 (2014). Special issue on aerodynamics of offshore wind energy systems and wakes, pp. 172–183. ISSN: 0960-1481. DOI: https://doi.org/10.1016/j.renene.2014.02.057.

[41] R. Barrett and A. Ning. "Integrated free-form method for aerostructural optimization of wind turbine blades". In: *Wind Energy* 21.8 (2018), pp. 663–675. DOI: 10.1002/we.2186. eprint: https://onlinelibrary.wiley.com/doi/pdf/10.1002/we.2186.

[42] J. L. Zhou, A. Tits, and C. T. Lawrence. *User's guide for FFSQP version 3.7: A FORTRAN Code for Solving Constrained Nonlinear (Minimax) Optimization Problems, Generating Iterates Satisfying All Inequality and Linear Constraints*. University of Maryland. 1997.

[43] N. P. Salunke, J. R. Ahamad, and S. A. Channiwala. "Airfoil Parameterization Techniques: A Review". In: *American Journal of Mechanical Engineering* 2.4 (2014), pp. 99–102.

[44] A. Shahrokhi and A. Jahangirian. "Airfoil shape parameterization for optimum Navier–Stokes design with genetic algorithm". In: *Aerospace Science and Technology* 11.6 (2007), pp. 443–450. ISSN: 1270-9638. DOI: https://doi.org/10.1016/j.ast.2007.04.004.

[45] H. Sobieczky. "Geometry Generator for CFD and Applied Aerodynamics". In: *New Design Concepts for High Speed Air Transport*. Ed. by H. Sobieczky. Vienna: Springer Vienna, 1997, pp. 137–157. ISBN: 978-3-7091-2658-5. DOI: 10.1007/978-3-7091-2658-5_9.

[46] H. Sobieczky. "Parametric Airfoils and Wings". In: *Recent Development of Aerodynamic Design Methodologies: Inverse Design and Optimization*. Ed. by Kozo Fujii and George S. Dulikravich. Wiesbaden: Vieweg+Teubner Verlag, 1999, pp. 71–87. ISBN: 978-3-322-89952-1. DOI: 10.1007/978-3-322-89952-1_4.

[47] T. Zhang, W. Huang, Z. Wang, and L. Yan. "A study of airfoil parameterization, modeling, and optimization based on the computational fluid dynamics method". In: *Journal of Zhejiang University-SCIENCE A* 17.8 (Aug. 2016), pp. 632–645. ISSN: 1862-1775. DOI: 10.1631/jzus.A1500308.

[48] M. Ceze, M. Hayashi, and E. Volpe. "A Study of the CST Parameterization Characteristics". In: *27th AIAA Applied Aerodynamics Conference*. 22 - 25 June 2009.

[49] D. Rajnarayan, A. Ning, and J. Mehr. "Universal Airfoil Parametrization Using B-Splines". In: *2018 Applied Aerodynamics Conference, AIAA AVIATION Forum*. 2018.

[50] A. Shikhar Jaiswal. "Shape Parameterization of Airfoil Shapes Using Bezier Curves". In: *Innovative Design and Development Practices in Aerospace and Automotive Engineering*. Ed. by Ram P. Bajpai and U. Chandrasekhar. Singapore: Springer Singapore, 2017, pp. 79–85. ISBN: 978-981-10-1771-1.

[51] H. Prautzsch, W. Boehm, and M. Paluszny. *Bézier and B-Spline Techniques*. Springer-Verlag Berlin Heidelberg, 2002. ISBN: 978-3-540-43761-1.

[52] G. Farin. *Curves and Surfaces for CAGD A Practical Guide*. Ed. by Elsevier Science & Technology. 5th Edition. Elsevier Science & Technology, 2001. ISBN: 978-1-55860-737-8.

[53] F. Grasso. "Usage of Numerical Optimization in Wind Turbine Airfoil Design". In: *Journal of Aircraft* 48.1 (2011), pp. 248–255. DOI: DOI:10.2514/1.C031089.

[54] F. Grasso, D. Coiro, N. Bizzarrini, and G. Calise. "Design of advanced airfoil for stall-regulated wind turbines". In: *Wind Energy Science* 2.2 (2017), pp. 403–413. DOI: 10.5194/wes-2-403-2017.

[55] M. Drela. "XFOIL: An Analysis and Design System for Low Reynolds Number Airfoils". In: *Low Reynolds Number Aerodynamics*. Ed. by Thomas J. Mueller. Berlin, Heidelberg: Springer Berlin Heidelberg, 1989, pp. 1–12. ISBN: 978-3-642-84010-4.

[56] M. Drela. *XFOIL 6.94 User Guide*. MIT Aero & Astro. Dec. 2001.

[57] J. van Ingen. "The eN Method for Transition Prediction. Historical Review of Work at TU Delft". In: *38th Fluid Dynamics Conference and Exhibit, Fluid Dynamics and Co-located Conferences*. 2008.

[58] L. A. Viterna and R. D. Corrigan. *Fixed pitch rotor performance of large horizontal axis wind turbines*. Tech. rep. 19830010962. Cleveland, Ohio: NASA Lewis Research Center, Jan. 1982.

[59] P. J. Moriarty and A. C. Hansen. *AeroDyn Theory Manual*. Tech. rep. NREL/TP-500-36881. National Renewable Energy Laboratory, 2005.

[60] C. L. Bottasso, A. Croce, Y. Nam, and C. E. D. Riboldi. "Power curve tracking in the presence of a tip speed constraint". In: *Renewable Energy* 40.1 (2012), pp. 1–12. ISSN: 0960-1481. DOI: https://doi.org/10.1016/j.renene.2011.07.045.

[61] International Electrotechnical Commission. *IEC 61400-1 Wind Turbines - Part 1: Design Requirements, 3rd Edition*. Tech. rep. 2006.

[62] *Guideline for the Certification of Wind Turbines*. Hamburg: Germanischer Lloyd Industrial Services GmbH. 2010.

[63] C. L. Bottasso and A. Croce. *Cp-Lambda a Code for Performance, Loads, Aeroelasticity by Multi-Body Dynamics Analyis*. Tech. rep. Politecnico di Milano, 2010-2017.

[64] J. P. Blasques. *A cross section analysis tool for anisotropic and inhomogeneous beam sections of arbitrary geometry*. Risø DTU - National Laboratory for Sustainable Energy Technical University of Denmark. Frederiksborgvej 399, P.O. Box 49, Building 114, DK-4000 Roskilde, Denmark, Feb. 2012.

[65] V. Giavotto, M. Borri, P. Mantegazza, G. Ghiringhelli, V. Carmaschi, G. C. Maffioli, and F. Mussi. "Anisotropic beam theory and applications". In: *Computers & Structures* 16.1 (1983), pp. 403–413. ISSN: 0045-7949. DOI: https://doi.org/10.1016/0045-7949(83)90179-7.

[66] L. Fingersh, M. Hand, and A. Laxson. *Wind Turbine Design Cost and Scaling Model*. Tech. rep. NREL/TP-500-40566. National Renewable Energy Laboratory, Dec. 2006.

[67] S. Tegen, M. Hand, B. Maples, E. Lantz, P. Schwabe, and A. Smith. *2010 Cost of Wind Energy Review*. Tech. rep. NREL/TP-5000-52920. National Renewable Energy Laboratory, Apr. 2012.

[68] S. Tegen, E. Lantz, M. Hand, B. Maples, A. Smith, and P. Schwabe. *2011 Cost of Wind Energy Review*. Tech. rep. NREL/TP-5000-56266. National Renewable Energy Laboratory, Mar. 2013.

[69] C. Moné, A. Smith, B. Maples, and M. Hand. *2013 Cost of Wind Energy Review*. Tech. rep. NREL/TP-5000-63267. National Renewable Energy Laboratory, Feb. 2015.

[70] D. J. Malcolm and A. C. Hansen. *WindPACT Turbine Rotor Design Study June 2000 — June 2002*. Tech. rep. NREL/SR-500-32495. National Renewable Energy Laboratory, 2006.

[71] D. A. Griffin. *WindPACT Turbine Design Scaling Studies Technical Area 1 - Composite Blades for 80- to 120-Meter Rotor*. Tech. rep. NREL/SR-500-29492. National Renewable Energy Laboratory, Apr. 2001.

[72] K. Smith. *WindPACT Turbine Design Scaling Studies Technical Area 2: Turbine, Rotor, and Blade Logistics*. Tech. rep. NREL/SR-500-29439. National Renewable Energy Laboratory, June 2001.

[73] D. T. Griffith and W. Johanns. *Large blade manufacturing cost studies using the Sandia blade manufacturing cost tool and Sandia 100-meter blades*. Tech. rep. SANDIA Report SAND2013-2374. Albuquerque, New Mexico: SANDIA Natonial Laboratories, 2013.

[74] W. A. Timmer and R. P. J. O. M. van Rooij. "Summary of the Delft University Wind Turbine Dedicated Airfoils". In: *Journal of Solar Engineering* 125.4 (2003), pp. 488–496.

[75] C. Bak, F. Zahle, R. Bitsche, T. Kim, A. Yde, L. C. Henriksen, M. H. Hansen, J. Blasques, M. Gaunaa, and A. Natarajan. *The DTU 10-MW Reference Wind Turbine*. Tech. rep. DTU Wind Energy, 2013.

[76] A. Björck. *Coordinates and calculations for the FFA-Wl-xxx, FFA-W2-xxx AND FFA-W3-xxx series of airfoils for horizontal axis wind turbines*. Tech. rep. FFA TN 1990-15. The Aeronautical Research Institute of Sweden, 1990.

[77] R. Quinn, G. Schepers, and B. Bulder. "A parametric investigation into the effect of low induction rotor (LIR) wind turbines on the levelised cost of electricity for a 1 GW offshore wind farm in a North Sea wind climate". In: *13th Deep Sea Offshore Wind R&D Conference, EERA DeepWind 2016*. Trondheim, Norway, Jan. 2016.

[78] L. Wang, X. Liu, and A. Kolios. "State of the art in the aeroelasticity of wind turbine blades: Aeroelastic modelling". In: *Renewable and Sustainable Energy Reviews* 64 (2016), pp. 195–210. ISSN: 1364-0321. DOI: https://doi.org/10.1016/j.rser.2016.06.007.

[79] V. A. Riziotis and H. A. Madsen. "Aeroelasticity and structural dynamics of wind turbines". In: *Wind Energy Systems*. Ed. by John D. Sørensen and Jens N. Sørensen. Woodhead Publishing Series in Energy. Woodhead Publishing, 2011, pp. 46–111. ISBN: 978-1-84569-580-4. DOI: https://doi.org/10.1533/9780857090638.1.46.

[80] F. Gualdoni. "Design optimization of wind turbines". PhD thesis. Politecnico di Milano, 2014.

[81] O. A. Bauchau, C. L. Bottasso, and Y. G. Nikishkov. "Modeling rotorcraft dynamics with finite element multibody procedures". In: *Mathematical and Computer Modelling* 33.10 (2001), pp. 1113–1137. ISSN: 0895-7177. DOI: https://doi.org/10.1016/S0895-7177(00)00303-4.

[82] C. L. Bottasso, A. Croce, B. Savini, W. Sirchi, and L. Trainelli. "Aero-servo-elastic modeling and control of wind turbines using finite-element multibody procedures". In: *Multibody System Dynamics* 16.3 (Oct. 2006), pp. 291–308. ISSN: 1573-272X. DOI: 10.1007/s11044-006-9027-1.

[83] L. Piegl and W. Tiller. *The NURBS book*. Ed. by Springer-Verlag Berlin. 2nd edition. Springer-Verlag Berlin, 1997.

[84] O. A. Bauchau. *Flexible Multibody Dynamics (Solid Mechanics and Its Applications)*. Springer, 2010. ISBN: 9400703341.

[85] M. O. L. Hansen. *Aerodynamics of Wind Turbines: second edition*. 2nd ed. Earthscan, 2008. ISBN: 978-1-84407-438-9.

[86] D. M. Pitt. "Theoretical prediction of dynamic inflow derivatives". In: *Vertica* 5 (1981), pp. 21–34.

[87] B. J. Jonkman. *TurbSim User's Guide: Version 1.50*. Tech. rep. NREL/TP-500-46198. National Renewable Energy Laboratory, Aug. 2009.

[88] C. E. D. Riboldi. "Advanced control laws for variable-speed wind turbines and supporting enabling technologies". PhD thesis. Politecnico di Milano, 2012.

[89] P. Bortolotti, C. L. Bottasso, and A. Croce. "Combined preliminary–detailed design of wind turbines". In: *Wind Energy Science* 1.1 (2016), pp. 71–88. DOI: 10.5194/wes-1-71-2016.

[90] L. Sartori, P. Bortolotti, A. Croce, and C. L. Bottasso. "Integration of prebend optimization in a holistic wind turbine design tool". In: *Journal of Physics: Conference Series* 753.6 (2016), p. 062006.

[91] A. Croce, L. Sartori, P. Bortolotti, and C. L. Bottasso. "Lightweight design of the INNWIND.EU and AVATAR rotors through multidisciplinary optimization algorithms". In: *15th Deep Sea Offshore Wind R&D conference*. Trondheim, Norway, Jan. 2018.

[92] P. K. Chaviaropoulos, I. Karga, C. Harkness, and B. Hendricks. *INNWIND Deliverable 1.2.3 PI-based assessment of innovative concepts (methodology),* tech. rep. INNWIND.EU, 2014.

[93] C. R. Sucameli, P. Bortolotti, A. Croce, and C. L. Bottasso. "Comparison of some wind turbine noise emission models coupled to BEM aerodynamics". In: *Journal of Physics: Conference Series* 1037.2 (2018), p. 022038.

[94] M. H. Hansen and L. C. Henriksen. *Basic DTU Wind Energy controller*. Tech. rep. DTU Wind Energy, Technical University of Denmark, 2013.

[95] P. Bortolotti, G. Adolphs, and C. L. Bottasso. "A methodology to guide the selection of composite materials in a wind turbine rotor blade design process". In: *Journal of Physics: Conference Series* 753.6 (2016), p. 062001.

[96] H. J. Sutherland. *On the Fatigue Analysis of Wind Turbines*. Tech. rep. SAND99-0089. Albuquerque, New Maxico: SANDIA National Laboratories, June 1999.

[97] E. P. Hong, B. J. You, C. H. Kim, and G. J. Park. "Optimization of flexible components of multibody systems via equivalent static loads". In: *Structural and Multidisciplinary Optimization* 40.1 (Jan. 2010), pp. 549–562. ISSN: 1615-1488. DOI: 10.1007/s00158-009-0384-2.

[98] T. P. Philippidis and A. P. Vassilopoulos. "Complex stress state effect on fatigue life of GRP laminates. Part II, Theoretical formulation". In: *International Journal of Fatigue* 24.8 (2002), pp. 825–830. ISSN: 0142-1123. DOI: https://doi.org/10.1016/S0142-1123(02)00004-X.

[99] The European Union. *EN 1993-1-9 Eurocode 3: Design of steel structures - Part 1-9: Fatigue*.

[100] C. Lindenburg and G. D. de Winkel. *Buckling load prediction tools for rotor blades*. Tech. rep. ECN-C-05-103. ENergy Research Centre of the Netherlands, 2005.

[101] K. Dykes, F. Zahle, K. Merz, M. McWilliam, and P. Bortolotti. "IEA Wind Task 37: Systems Modeling Framework and Ontology for Wind Turbines and Plants". In: *Wind Energy Science Conference 2017*. 2017.

[102] D. J. Lekou, D. Chortis, P. Chaviaropoulos, X. Munduate, A. Irisarri, H. Aa. Madsen, K. Yde, K. Thomsen, M. Stettner, M. Reijerkerk, F. Grasso, R. Savenije, G. Schepers, and C. F. Andersen. *AVATAR Deliverable D1.2 Reference Blade Design*. Tech. rep. AVATAR, 2015.

[103] P. Chaviaropoulos, F. Rasmussen, A. B. Abrahamsen, D. Conti, A. Natarajan, G. Roukis, A. Makris, L. Sartori, F. Bellini, A. Croce, H. Polinder, D. Kaufer, J. A. Armendariz, Jumar, D. Powell, P. Todd, and R. CLark. *INNWIND Deliverable 1.25: PI-based assessment (application) on the results of WP2-WP4 for 20 MW wind turbines*. Tech. rep. INNWIND.EU, Sept. 2017.

[104] A. Croce, L. Sartori, R. Riva, M. Spinelli, F. Zahle, A. Barlas, A. Milidis, D. Manolas, R. M. S. Roman, C. A. Pueyo, and M. Schwarz. *Aerodynamics of Large Rotors WP4 Deliverable 4.12 Effect of blade flexibility and structural tailoring on loads*. Tech. rep. AVATAR, 2017.

[105] D. W. Lobitz and P. S. Veers. "Aeroelastic behavior of twist-coupled HAWT blades". In: *1998 ASME Wind Energy Symposium*. 1998. DOI: doi:10.2514/6.1998-29.

[106] D. W. Lobitz and P. S. Veers. "Load Mitigation with Bending/Twist-coupled Blades on Rotors using Modern Control Strategies". In: *Wind Energy* 6.2 (2003), pp. 105–117. ISSN: 1099-1824. DOI: 10.1002/we.74.

[107] K. Cox and A. Echtermeyer. "Geometric Scaling Effects of Bend-twist Coupling in Rotor Blades". In: *Energy Procedia* 35.Supplement C (2013). DeepWind'2013 – Selected papers from 10th Deep Sea Offshore Wind R&D Conference, Trondheim, Norway, 24 – 25 January 2013, pp. 2–11. ISSN: 1876-6102. DOI: https://doi.org/10.1016/j.egypro.2013.07.153.

[108] C. L. Bottasso, F. Campagnolo, A. Croce, and C. Tibaldi. "Optimization-based study of bend–twist coupled rotor blades for passive and integrated passive/active load alleviation". In: *Wind Energy* 16.8 (2013), pp. 1149–1166. ISSN: 1099-1824. DOI: 10.1002/we.1543.

[109] R. W. Vesel and J. J. McNamara. "Performance enhancement and load reduction of a 5 MW wind turbine blade". In: *Renewable Energy* 66.Supplement C (2014), pp. 391–401. ISSN: 0960-1481. DOI: https://doi.org/10.1016/j.renene.2013.12.019.

[110] M. K. McWilliam, F. Zahle, A. Dicholkar, D. Verelst, and T. Kim. "Optimal Aero-Elastic Design of a Rotor with Bend-Twist Coupling". In: *Journal of Physics: Conference Series* 1037.4 (2018), p. 042009.

[111] A. Pirrera, M. Capuzzi, N. Buckney, and P. M. Weaver. "Optimization of Wind Turbine Blade Spars". In: *53rd AIAA/ASME/ASCE/AHS/ASC Structures, Structural Dynamics and Materials Conference*. Honolulu, Haway, Apr. 2012.

[112] N. Buckney, S. Green, A. Pirrera, and P. M. Weaver. "On the structural topology of wind turbine blades". In: *Wind Energy* 16.4 (2013), pp. 545–560.

[113] N. Buckney, A. Pirrera, S. D. Green, and P. M. Weaver. "Structural efficiency of a wind turbine blade". In: *Thin-Walled Structures* 67 (2013), pp. 144–154.

[114] P. Chaviaropoulos, G. Sieros, D. Lekou, B. Bacharoudis, C. Tibaldi, T. Barlas, F. Zahle, H. A. Madsen, F. Rasmussen, A. B. Abrahamsen, T. P. Philippidis, G. Roukis, A. Croce, D. Kaufer, and J. A. Armendariz. *INNWIND Deliverable 1.24 PI-based assessment on the Results of WP2-WP4*. Tech. rep. INNWIND.EU, 2015.

[115] A. Croce, L. Sartori, M. S. Lunghini, L. Clozza, P. Bortolotti, and C. L. Bottasso. "Lightweight rotor design by optimal spar cap offset". In: *Journal of Physics: Conference Series* 753.6 (2016), p. 062003.

[116] M. Capuzzi, A. Pirrera, and P. M. Weaver. "A novel adaptive blade concept for large-scale wind turbines. Part I: Aeroelastic behaviour". In: *Energy* 73 (2014), pp. 15–24. ISSN: 0360-5442. DOI: https://doi.org/10.1016/j.energy.2014.06.044.

[117] M. Capuzzi, A. Pirrera, and P. M. Weaver. "A novel adaptive blade concept for large-scale wind turbines. Part II: Structural design and power performance". In: *Energy* 73 (2014), pp. 25–32. ISSN: 0360-5442. DOI: https://doi.org/10.1016/j.energy.2014.04.073.

[118] N. Buckney, A. Pirrera, and P. M. Weaver. "Structural Efficiency Measures for Sections Under Asymmetric Bending". In: *Journal of Mechanical Design* 137.1 (2015), p. 011405. DOI: 10.1115/1.4028590.

[119] L. A. Polgati. "Optimization of a low induction 10 MW rotor with passive load reduction system". MA thesis. Politecnico di Milano, 2017.

[120] Y. Guo, T. Parsons, R. King, K. Dykes, and P. Veers. *An Analytical Formulation for Sizing and Estimating the Dimensions and Weight of Wind Turbine Hub and Drivetrain Components*. Tech. rep. NREL/TP-5000-63008. National Renewable Energy Laboratory, June 2015.

[121] Y. Guo, T. Parsons, K. Dykes, and R. N. King. "A systems engineering analysis of three-point and four-point wind turbine drivetrain configurations". In: *Wind Energy* 20.3 (2017), pp. 537–550. DOI: 10.1002/we.2022. eprint: https://onlinelibrary.wiley.com/doi/pdf/10.1002/we.2022.

[122] R. Damiani, K. Dykes, and G. Scott. “A comparison study of offshore wind support structures with monopiles and jackets for U.S. waters”. In: *Journal of Physics: Conference Series* 753.9 (2016), p. 092003.

[123] J. M. Jonkman, A. N. Robertson, and G. J. Hayman. *HydroDyn User’s Guide and Theory Manual*. National Renewable Energy Laboratory. 2015.

[124] G. Katsouris and A. Marina. *Cost modelling of floating wind farm*. Tech. rep. ECN-E–15- 078. ECN, 2016.